Mechanism of Contact Electrification and Improved Performance of Triboelectric Nanogenerators via Surface Modification with Functional Materials

A Dissertation
Presented to
The Academic Faculty

by

Aurelia Chi Wang

In Partial Fulfillment
of the Requirements for the Degree
Doctor of Philosophy in the
School of Materials Science and Engineering

Georgia Institute of Technology
August, 2020

Approved by:

Dr. Zhiqun Lin, Advisor
School of Materials Science and Engineering
Georgia Institute of Technology

Dr. Vladimir Tsukruk
School of Materials Science and Engineering
Georgia Institute of Technology

Dr. Preet Singh
School of Materials Science and Engineering
Georgia Institute of Technology

Dr. Yulin Deng
School of Chemical and Biomolecular Engineering
Georgia Institute of Technology

Dr. Meilin Liu
School of Materials Science and Engineering
Georgia Institute of Technology

Date Approved: July 20, 2020

ACKNOWLEDGEMENTS

I would like to express my sincere appreciation and gratitude to my academic advisors, Dr. Zhiqun Lin and Dr. Zhong Lin Wang, without whom none of this could have been possible. They provided incredible support, insightful guidance, and thoughtful encouragement throughout my Ph.D. career, and I truly owe them everything from the bottom of my heart. I would like to thank my thesis committee, Dr. Preet Singh, Dr. Vladimir Tsukruk, Dr. Meilin Liu, and Dr. Yulin Deng for their willingness to support my career as well as their continuous inspiration and guidance. Also, I would like to thank Dr. Cheng Xu and Binbin Zhang for their amazing support and assistance in our research endeavors.

I would also like to thank every group member, past and present, for their kind support and camaraderie, as well as for providing much appreciated assistance whenever I needed them. In particular, I would like to mention Jiwoo Yu for her wonderful companionship and eager support in characterizing materials, Dr. Meng Zhang for leading me through the field of perovskites, Dingfeng Shen for guiding me and supplying his expertise, Dr. Jiabin Qi and Dr. Shuang Pan for involving me in their research and discussions, Dr. Changsheng Wu for his assistance with my review paper, Dr. Yeu Wei Harn for her assistance with polymer synthesis, and Dr. Haiyang Zou for his continued support in cleanroom fabrication. I would express my deepest gratitude to Dr. James Iocozzia, Dr. Yihuang Chen, Dr. Shuguang Zhang, Dr. Chuntao Lan, Dr. Yanjie He, Dr. Meidan Ye, Dr. Xun Cui, Dr. Cheng-Hsin Lu, Dr. Likun Gao, Dr. Zili Li, Dr. Wendan Xue, Dr. Shumeng Hao, Dr. Shiqiang Zhao, Dr. Ming He, Dr. Zewei Wang, Matt Rager, Gill

Biesold-McGee, Chris Sewell, Shuang Liang, Songru Jia, Mingyue Zhang, Woosung Choi, Baoying Dai, Jiawei Zhang, and Fan-Wei Liu for being an incomparably amazing lab family. I would also like to thank Dr. Longfei Wang, Dr. Steven Zhang, Dr. Wenbo Ding, Dr. Dong Kai, Dr. Yuliang Chen, Dr. Minyi Xu, Dr. Yi Xi, Dr. Hengyu Guo, Dr. Yong Ding, and all the members of the Wang lab for their insightful conversations, assistance, and inspiration throughout the years.

Lastly, I would like to thank my family and friends from the bottom of my heart for their whole-hearted support throughout my Ph.D. studies.

TABLE OF CONTENTS

LIST OF TABLES

LIST OF FIGURES

SUMMARY

Efforts to establish a universal explanation of contact electrification (CE) have spanned many centuries, and yet our understanding of this commonplace phenomenon remains to be explored. With the landscape of triboelectrification research changing so dramatically in the past few years due to the invention of triboelectric nanogenerators (TENGs) and their wide gamut of applications and innovations, it is imperative that we make efforts to understand CE moving forward. Through our research, we have unraveled the underlying mechanisms of CE using high temperature resistant TENGs. We have correlated the exponential decay trends of surface charges on the contact separation Ti-SiO_2 and Ti-Al_2O_3 TENGs at high temperatures to the model of thermionic emission of electrons. With this knowledge in hand, we have developed a surface states model for CE in metal-semiconductor pairs with clear energy levels and an electron cloud potential-well model for CE in metal-dielectric or dielectric-dielectric pairs, which could be extended to universal solid-solid CE. Investigating sliding mode Ti-SiO_2 TENGs at high temperature with a similar material scheme resulted in an extension of those models. We also determined that the sliding mode TENGs were even able to generate charges at high temperature without any pre-charging of the SiO_2 substrates, which was essential for maintaining any surface charges in the contact-separation mode. We determined that the model for the sliding mode TENG should be area-dependent, and when the displaced area is greater than the area in contact, thermionic emission has the potential to overtake the charge generation capabilities of the TENG. Following our studies on thermionic emission and charge degradation on surfaces in high temperature, we developed a high temperature-

resistant rotating TENG that was capable of generating and maintaining an appreciable level of charge even at 673 K through pre-annealing at similarly high temperatures to achieve extremely tight contact.

Functional materials that are robust and capable of being tuned for optimal triboelectric charge generation are of great interest to the development of hybrid and sensing TENG applications. We investigated the effects of precursor modulation on the surface morphology of CsFAMAPb(I_xBr_{1-x})$_3$ thin films fabricated through a facile, one-step spin coating process. We found that lowering the CsI molar ratio in the precursor solution to 0.02 produced the highest improvement in TENG output, resulting in a 26.5% increase in V_{OC}, 24.4% increase in I_{SC}, and 17.5% increase in Q_{SC} over the lowest performing sample with a CsI molar ratio of 0.14. Also, a unique TENG triboelectric material design with CsFAMAPb(I_xBr_{1-x})$_3$ paired with interfacial layers of SnO_2 and P3HT exhibited improved electrical output performance, particularly in V_{OC}, under solar simulator illumination compared to without any carrier charge transport layers. Finally, effective electrical output improvements were made on a PAzoMA microsphere-based TENG by using 450 nm blue LPL to irradiate said microspheres and produce elongations of up to an aspect ratio of 1.82 in the direction of light polarization. It was found that irradiation at 300 mW cm^{-2} for 3 hours produced the greatest TENG output improvement over microspheres without light treatment, with a 16% increase in V_{OC}, 20.8% increase in I_{SC}, and 10.7% increase in Q_{SC}. The understanding of functional materials and the factors that impact their performance in TENGs for sensors and energy harvesting is of great importance to their eventual commercial usage.

CHAPTER1. INTRODUCTION

In society's ever-growing drive for technological, cultural, and civil advancement, reliable sources of energy are of utmost importance. The availability of electric power to any household is often a key factor in determining the quality of life, and is vital to developing any infrastructure without severe limitations. With the world advancing towards globalization and the expansion of developed societies, the availability of energy globally presents a pressing issue. The collective human consumption of power in 2005 was calculated to be 13 terawatts (TW) with 85% coming from pollution-producing fossil fuels, and projected to be 30 TW by 2050.[1] In developing new ways to produce energy, not only should the methods be adequate to support a growing population and demand, but also renewable and sustainable for the earth.

In order to support the demands of a developing world along the path to an electronics and Internet of Things (IoT)-based future, a safe, cost-effective, efficient, sustainable, and renewable source of energy is required. Mechanical energy harvesting has the potential to fulfill all of these roles with the most ease, availability, and adaptability. The sources of otherwise largely wasted mechanical energy and ambient vibrational energy are innumerable and easily identified, including human motion, wind, and water currents. Wind turbines and hydroelectric generators are commonly used, although these are based on standard electric generators that require a regular and high frequency input, lowering their efficiency. Nanogenerators are relatively simple in design and capable of high-efficiency energy harvesting, miniaturization or large scale operation, and do not require a

high frequency mechanical input to be viable. The construction of nanogenerators can range from a simple dielectric/polymer in contact with another dielectric or conducting surface (triboelectric effect) to micro-scale arrays of nanowires that produce electricity when deformed (piezoelectric effect). The versatility and excellent voltage output of nanogenerators have made them a research topic of interest in the past decade, and further improvements and applications continue to surface.

1.1 Triboelectric Nanogenerators

The triboelectric nanogenerator (TENG) was first invented in 2012 and operates on the contact electrification between materials and electrostatic induction through a circuit.[2] The material selection for TENGs is vast due to the nature of most materials to accept or relinquish electrons to another material. Not only are TENGs capable of harvesting low frequency, irregular motion in self-powering applications, but they also may be used as highly sensitive motion and pressure sensors.[3] Many efforts have been conducted to modify the surfaces of the contacting materials in order to increase charge density, and improvements in design and adaptability are continually being made.

1.1.1 Mechanisms of Energy Harvesting

The fundamental operation of a double electrode TENG is depicted in **Figure 1a**, in which two dielectrics, e.g. polymers and metals, are connected to electrodes.[4] As the two dielectrics contact, immobile electrostatic charges transfer to both surfaces due to the triboelectric effect, shown in **Figure 1a(ii)**. As the number of times the dielectrics contact increases, surface charge density σ_C is built up until it reaches a saturation, shown in **Figure 1a(iii)**. The electrons are driven to flow through the external load, causing a buildup of

electrons in the electrode $\sigma_l(z,t)$, which is a function of the gap distance $z(t)$ between the two dielectrics. Thus, mechanical motion that causes the two dielectrics to contact has been converted to electricity, which may be readily stored and used. In Maxwell's equations, Ampère's law states that:

$$\nabla x \boldsymbol{H} = \boldsymbol{J_f} + \frac{\partial \boldsymbol{D}}{\partial t} \tag{1}$$

where H is the magnetizing field, J_f is the free electric current density, and D is the displacement field. The term $\frac{\partial D}{\partial t}$ is Maxwell's displacement current J_D, which is defined as:

$$J_D = \frac{\partial \boldsymbol{D}}{\partial t} = \epsilon_0 \frac{\partial \boldsymbol{E}}{\partial t} + \frac{\partial \boldsymbol{P}}{\partial t} \tag{2}$$

where ε_0 is the permittivity in vacuum, E is the electric field, and P is the polarization field.[26] The displacement current is therefore a time-varying electric field, plus a contribution from the movement of charges bound in atoms, or dielectric polarization. The $\epsilon_0 \frac{\partial E}{\partial t}$ component accounts for electromagnetic waves, while $\frac{\partial P}{\partial t}$ contributes to the surface polarization mechanism behind nanogenerators. While the displacement current has been mainly tied to the generation of electromagnetic waves, the dielectric polarization component will prove indispensable for future self-powering developments such as nanogenerators.

The equivalent circuit of a TENG in **Figure 1b** depicts two circuit elements – a capacitance term C_{TENG}, which originates from the capacitance between the two electrodes, and an open-circuit voltage term V_{OC}, which originates from the separation of polarized tribo-charges.

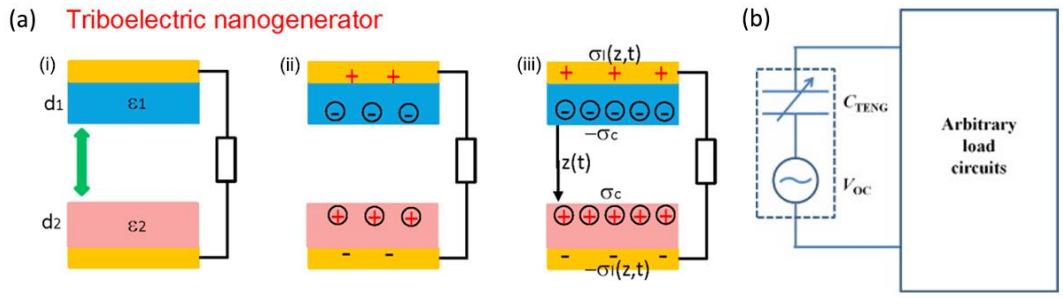

Figure 1. Schematics of a TENG. (a) Working mechanism of TENG with the increase of contact cycles. (b) Equivalent electrical circuit of TENG. Reproduced with permission.[4] Creative Commons license.

As the inherent capacitance of a TENG is increased, the impedance to the AC voltage source V_{OC} will increase, lowering the impedance match between the load and C_{TENG}. C_{TENG} and V_{OC} are functions of moving distance (x) and structural parameters, being independent from velocity and acceleration. Therefore, the energy conversion mechanism of TENGs can harvest mechanical motion of a wider range of frequencies and consistencies compared to most EMIGs.

1.1.2 Modes of Triboelectric Nanogenerators

A variety of modes of operation have been developed for TENGs in order to define energy conversion methods and designs, as depicted in **Figure 2**. In **Figure 2a**, the dielectric-to-dielectric mode involves two dielectric plates with metal layer electrodes deposited on the outer faces, separated by distance x, coming into contact through an external mechanical force. When this occurs, the inner faces have opposite static charges of equal density σ due to contact electrification. When the plates separate the charged

surfaces, an electric potential difference V is induced between the two electrodes, driving the electrons back and forth across the electrodes, in which Q is the amount of transferred charge. These vertical contact-separation TENGs can harvest energy from forces similar to the pressure from shoe soles while walking and waves in water. **Figure 2b** depicts the dielectric-to-dielectric (top) and metal-to-dielectric (bottom) sliding modes of TENGs, in which the bottom material is fixed while the top slides along the longitudinal direction. In this case, as the top layer is sliding and creating a lateral separation distance of x, opposite charges exist in the non-overlapping regions. The metal-to-dielectric mode has the metal surface acting as both a triboelectric layer and an electrode. These lateral sliding TENGs can harvest wind forces and sliding of fingers on a mobile phone. **Figure 2c** shows the single electrode mode of TENGs, where a single dielectric moves along the vertical direction towards a fixed primary and reference electrode. These single-electrode TENGs may be used to harvest motion from pressing on touchscreens, cars on city roads, and more. **Figure 2d** depicts a dielectric sliding-mode freestanding TENG, where two metal electrodes are placed in the same plane with an air gap in between, while a freestanding dielectric plate of the same size of one electrode is suspended above the electrodes and slides laterally across both. These freestanding triboelectric-layer TENGs can harvest energy from automobiles and trains, for instance. In order to compare the performances of all of these TENG modes, a system of standards in quantitative measurement must be put in place.

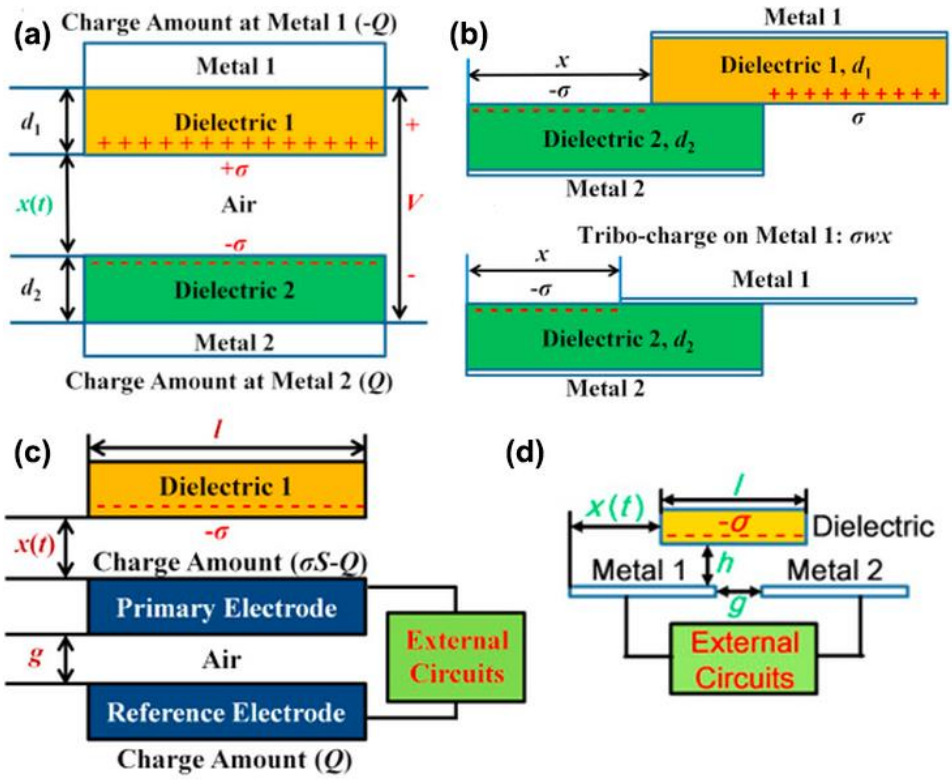

Figure 2. Theoretical models of different modes of TENG. (a) Vertical contact-separation TENG. (b) Lateral sliding TENG. (c) Single electrode TENG. (d) Freestanding triboelectric layer TENG. Reproduced with permission.[5-8] Copyright, Refs. 5, 6, 8. John Wiley & Sons, 2014. Ref. 7: Copyright, Elsevier 2015.

According to a study on the figure of merits for the differing operational modes of TENGs, the maximum potential output, from highest to lowest, for each of the featured modes was: contact freestanding triboelectric layer > contact-separation > sliding freestanding triboelectric layer > lateral sliding > contact single electrode.[9] It was previously determined that contact-separation TENGs have better performance at ambient temperatures than sliding mode TENGs, due to their lower maximum displacement to achieve the same level open circuit voltage values.[10] However, after new energy evaluation standards had been established, the sliding freestanding triboelectric layer model was found to have the highest output energy density among all the modes.[11] This maximal energy

density before dielectric breakdown was found to be >1000 J m^{-3} for a PDMS-based TENG in simulations. Increasing performance through design and material properties is key to commercial fabrication processes of TENGs, and is a highly attractive field of study in order to realize many of the potential applications of nanogenerators.

1.1.3 Recent Benchmarks and Applications

TENGs are capable of converting irregular, low frequency sources of mechanical energy to electric power, including biomechanical motion, vibrations, wind, water, and more, with great implications on mobile and sustainable sources of energy for the IoT.[12-22] When combined with functional materials, TENGs can create a wide variety of self-powered active sensors, with potential usage in robotics, soft/flexible electronics, and artificial intelligence.[23-29] In order to ensure the high performance of TENGs in such applications, constant improvements and theoretical studies are ongoing. Charge generation in air is limited by air breakdown of surface electrostatic charges, and it has been shown that TENG operation in a vacuum was able to raise the charge density from 120 μC m^{-2} to 1003 μC m^{-2}, which elevated the maximum output power density of the TENG from 0.75 to a whopping 50 W m^{-2} using a low frequency source of motion at 2 Hz.[30] Even more fascinating is the ability to achieve these levels of charge density in ambient conditions, which was realized by Xu *et al.* through the development of a charge pump designed TENG, which was able to achieve a charge density of 1020 μC m^{-2}, which is unprecedented and highly noteworthy for commercial integration of TENGs (**Figure 3**).[31] With such leaps and bounds made by TENG energy harvesting capabilities in recent years, it appears that the field is in a strong growth phase. Therefore, it is imperative that we more fully understand the theory behind contact electrification and its nuances.

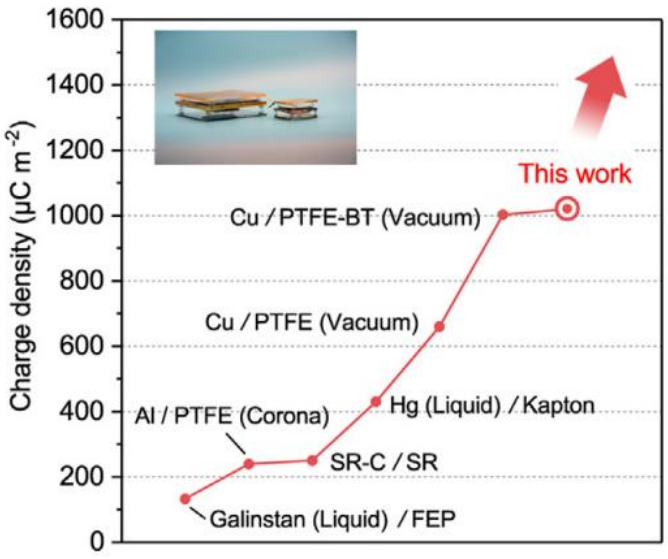

Figure 3. Ultrahigh charge density achieved in ambient conditions using a charge pump design TENG.

Another championing achievement made possible by TENGs is the creation of a comprehensive triboelectric series using a mercury liquid-solid TENG system with maximized intimate contact of the materials tested in highly controlled conditions.[32] There has been a lack of such rigorous quantitative characterization databases for materials in the past, perhaps due to the lack of applications involving triboelectricity previously. The number of commercially/environmentally appealing and scientifically significant developments made possible by TENGs continues to increase rapidly in recent years, and fields that have been born from nanogenerators, including tribotronics[17, 33] and piezophototronics[34-37], have been growing quickly as well.

CHAPTER 2. MOTIVATION, OBJECTIVES, AND OVERVIEW

2.1 Motivation

Efforts to establish a universal explanation of contact electrification (CE) have spanned many centuries, and yet our understanding of this commonplace phenomenon remains to be explored. Existing theories involving CE are highly material-dependent, and there lacks an agreement on an all-inclusive, dominant mechanism of CE. TENGs have proven to be valuable tools in studying the underlying mechanisms and effects of CE, so great progress on this front is possible. CE can occur for solid, liquid, and gas phases of matter, so any universal model should be carefully presented and investigated. With the landscape of triboelectrification research changing so dramatically in the past few years due to the invention of nanogenerators and their wide gamut of applications and innovations, it is imperative that we make efforts to understand CE moving forward. The research presented in this thesis puts forth multiple models that suggest the dominance of electron transfer in solid-solid CE, corroborated by data as well.

TENGs that operate well in extreme conditions are of significant interest due to the possible applications of TENGs in harvesting electricity in space or in automobiles, which have environments that are hostile to the stability and performance of many devices. Careful investigation of how TENGs perform, the factors that impact their efficiency, and innovating methods to counteract these factors are all important questions to answer through our research. From our studies into the theories behind CE that stemmed from our high temperature TENG analysis that tied thermionic emission to the degradation of charges on solid-solid TENGs at high temperature, we can develop a device that combats such phenomena. In this way, we may establish a roadmap in designing TENGs that are able to withstand other extremities in environmental properties.

Functional materials that are robust and capable of being tuned for optimal triboelectric charge generation are of great interest to the development of hybrid and sensing TENG applications. Due to the wide spectrum of materials that are possible for fabricating TENGs, there is a great deal of interest in examining the performances of novel materials that have not yet been used. For instance, new phenomena and beneficial factors could arise from the study of functional materials in charge generation from mechanical energy. It is important to combine disciplines so both fields can grow, so materials that are well known for ferroelectric, photoelectric, magnetic, etc. characteristics should be investigated in TENG applications. Even if these materials may not be as commercially appealing as widely available polymers and dielectrics, we may still learn a great deal about their electrical properties and effects of chemical/physical alteration on their charge generation capabilities. Additionally, in the pursuit of innovating hybrid energy harvesting devices, these functional materials are key to such goals.

Surface modification of TENG triboelectric materials is key to increasing their surface charge density and surface contact area, and facile, scalable methods to accomplish that are of great value. Therefore, self-assembly of micro/nanostructures to increase surface roughness would be optimal for its easy tunability, reliability, and convenience. Such techniques could be further combined with chemical surface functionalization or further geometrical modulation of features to increase the benefits for charge generation even more. We can combine this effort with a novel functional photoresponsive material to develop our knowledge of both TENG design and the material's unique properties even further.

2.2 Objectives

(1) Inquiry into the degradation of performance of high temperature-resistant material TENGs at high temperatures.

(2) Modeling our novel findings on CE through correlating our data with the thermionic emission model for electrons.
(3) Investigating the performance of sliding mode TENGs at high temperature and comparing it with our contact-separation TENG study.
(4) Designing a TENG that is capable of performing efficiently at high temperatures despite thermionic emission of charges.
(5) Investigating the effects of precursor tuning on triple cation mixed-halide perovskite surface morphology and its performance in a TENG.
(6) Surface modification using reverse breath figure method to fabricate azobenzene polymer microspheres and irradiating with linearly polarized light to change microstructure geometries, and studying their effects on charge generation in a TENG.

2.3 Map of Dissertation

This thesis reports on multiple novel models and theoretical claims on CE using TENGs at high temperature, as well as several material modification techniques in an effort to increase surface charge density and contact area of a TENG triboelectric material. Chapter 1 is an introductory overview of TENGs and recent developments of importance. Chapter 2 lists motivations of the presented work and organizes the research objectives that have been pursued through these studies. Chapter 3.1 details the initial high temperature TENG study to investigate the fundamentals of CE. Chapter 3.2 continues on this inquiry of sliding mode TENGs, which differ from contact-separation mode TENGs in significant ways and possible applications. Chapter 3.3 chronicles the endeavour made to quench the thermionic emission of electrons using a sliding, rotating TENG design to efficiently generate charges at high temperatures. Chapter 4 begins the functional material portion of

the thesis, including an analysis of chemical composition tuning to impact perovskite grain sizes and surface morphology for a TENG triboelectric surface. Chapter 5 continues on the functional material route, bringing to attention a novel azobenzene-based polymer as well as a self-assembly method to develop a novel surface modification technique. Finally, Chapter 6 summarizes the findings of significance from all chapters and includes future outlooks and developments in these areas since the publications of these studies. Chapter 7 lists publications that the author has had the honor of being involved in and references as well. This thesis interpolates material from three papers by the thesis author.[38-40] Chapter 3 uses material from References [38], [39], and [40], out of which [38] and [40] are co-first authored with Dr. Cheng Xu. Chapter 4 and 5 are based on unpublished data.

CHAPTER 3. CONTACT ELECTRIFICATION AND THERMIONIC EMISSION

3.1 Unraveling the Mechanism of Contact Electrification between Dielectrics and Conductors Using Triboelectric Nanogenerators at High Temperature

3.1.1 Introduction

Although contact-electrification (CE) (or triboelectrification) has been a documented phenomenon since the ancient Greek era from 2600 years ago, there still exist many debates regarding to the origins of this effect, the most important issue being whether the charge transfer occurs through electrons or ions and why the charges retain on the surface without a quick dissipation. The concept of electron transfer was well accepted in explaining metal-metal and metal-semiconductor electrification, as determined by the work function or contact potential difference,[41, 42] which could be extended to explain the metal-insulator electrification to some extent using the existence of surface states.[43-46] Ion transfer was also proposed to explain electrification, particularly which occurred involving polymers.[47, 48] Ions containing functional groups were believed to contribute to CE.[49-51] These discrepancies have continued to raise doubts about whether electron or ion transfer is the dominant underlying mechanism in CE.

It is worth noting that nearly all of these studies were based on quantitative analysis of generated charge amount, including the correlation of charge amount with band gaps, work function and ion densities[52, 53] and electrochemical reactions.[54, 55] It is also interesting to note that there are few time-dependent and/or temperature-dependent studies on the variation of surface electrostatic charges.[56] Here, we believe that the key to solving the debate may lie in developing a new method that can quantitatively obtain the surface charge

density/amount in real time, particularly under different temperatures. Accordingly, time-dependent studies on charge transfer may be accomplished through a newly developed TENG as an application of Maxwell's displacement current,[3, 4, 57, 58] due to the fact that the TENG's outputs are dictated by the surface charge density.[9] Recently, TENGs have been utilized to investigate CE at relatively low temperatures.[14, 59, 60] However, an in-depth study on the mechanism of CE is required to be performed at high temperatures, at which electron emission is possible. In such temperature ranges, the discharge of electrons or ions may follow distinct laws and they can be easily modeled and separated.

In this study, by designing a TENG that worked under high temperatures, real-time quantitative measurements of the surface charge density/amount were realized, facilitating a possible discovery of the charge identity and mechanism in CE. The TENG was designed to reflect the discharge performance of the surface electrostatic charges at high temperature; and the results were found to be consistent with the thermionic emission equation of electrons for both types of TENGs designed in the study. Moreover, it was found that different materials had different potential barrier heights at the surfaces, which would prevent the charges generated by CE from flowing back or dissipating. Furthermore, an electron cloud-potential well model was proposed based on the electron emission dominated charge transfer mechanism, which could be applied to understand all types of CE in general materials. This chapter section interpolates material from a paper co-authored by the thesis author with Professor Cheng Xu.[38]

3.1.2 Results and Discussion

3.1.2.1 Performance of the Ti-SiO_2 TENG

The conventional metal-polymer or polymer-polymer structure of TENGs was not adopted in this study, mainly because polymers could not withstand at high temperatures.

Here, two kinds of high-temperature-resistant contact-separation (CS) mode TENGs, a Ti-SiO_2 TENG and a Ti-Al_2O_3 TENG, were designed and fabricated, which were able to withstand a maximum temperature of 673 K and operate stably for a long period of time. Each TENG was placed in a heating cabinet, which could provide the desired temperature with an accuracy of ±5 K. The charges increasingly accumulate with the CS operation of the TENG and then tend to balance at 293 K (**Figure 4.**), with the operation principles shown in **Figure 5.**

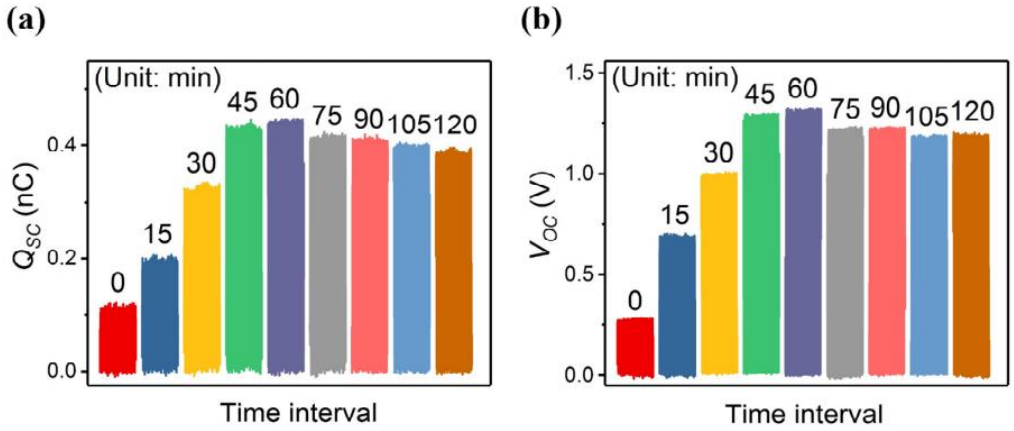

Figure 4. CE of the Ti-SiO_2 TENG at 293 K. Q_{SC} (a) and V_{OC} (b) changes of the TENG with the operation time increase.

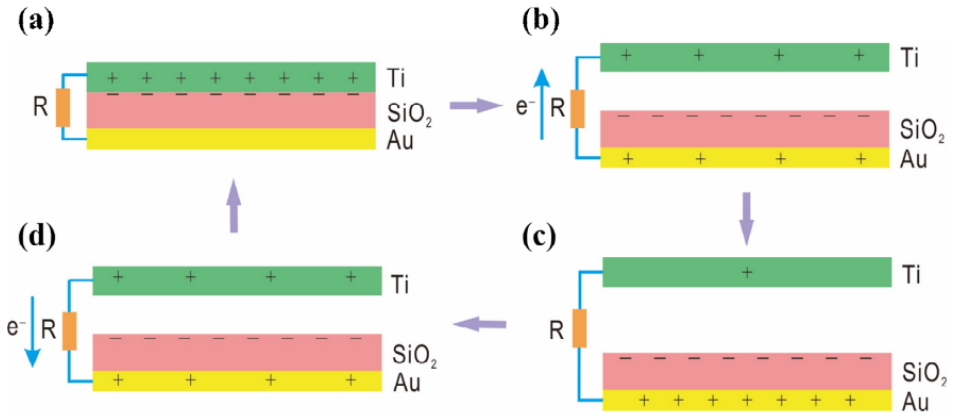

Figure 5. The operation principles of the Ti-SiO_2 TENG. When the Ti and SiO_2 get into contact, opposite triboelectric charges will be generated on the two surfaces with the same density: positive charges on the Ti and negative charges on SiO_2 (a). Upon releasing, the two oppositely charged surfaces start to get separated from each other, inducing a potential difference between the Ti and Au electrode. This potential difference will drive electrons flow from the Au electrode to Ti (b). When the separation between the two surfaces reaches the maximum, almost all the positive triboelectric charges on the Ti will be neutralized, so that positive charges on the Au electrode equals to the transferred charges on the Ti (c). Subsequently, when the Ti and SiO_2 are pressed to approach each other again, the reversed potential difference between the two electrodes will build, which leads to the back flow of all the transferred electrons from the Ti to Au electrode (d).

The structure of the Ti-SiO_2 TENG is shown in **Figure 6a**. It is worth noting that both the short-circuit transfer charge Q_{SC} (0.45 nC) and the open-circuit voltage V_{OC} (1.3 V) are rather low, which means that the CS Ti-SiO_2 TENG in the experiment can only generate limited charges during the CS operation. In addition, scanning electron microscope (SEM) images only show very slight structure change for both Ti foil and SiO_2 surfaces after CE for twenty thousand circles (**Figure 7**). Thus, to investigate the influence of temperature on the tribocharges on the surfaces, SiO_2 was first rubbed by polyurethane (PU) foam to introduce initial surface charges on SiO_2, as reflected by a Q_{SC} of around 45 nC. The cabinet was heated up to the desired temperature, and then held for 5 min to measure the variation of Q_{SC}. **Figure 6b** shows the change of Q_{SC} at temperatures of 353

K, 533 K and 583 K, demonstrating that the charge density decreased more rapidly at higher temperatures. When the temperature rose to 583 K, the charges quickly disappeared and the total Q_{SC} was less than 1 nC. Figure 1C shows the residual charges on the TENG after 5 min of measurement at different temperatures and the inset is the diagram of the working model of the CS Ti-SiO_2 TENG. The residual charges decreased more rapidly with the increase of the temperature, and it is interesting to note that they started to decrease more rapidly once the temperature is higher than 533 K.

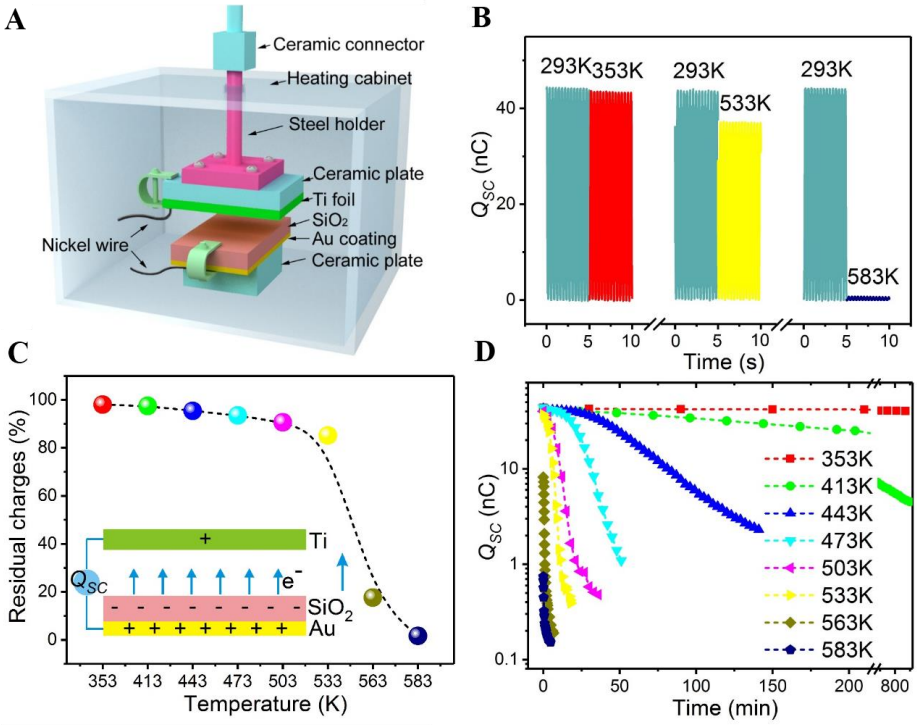

Figure 6. Performance of the Ti-SiO_2 TENG at different temperatures. (A) Setup of the measurement platform. (B) The total transferred changes Q_{SC} at room temperature and various high temperatures for three groups of experiments, respectively. (C) The percentage of residual charges of the TENG at different temperatures. The residual charges are the Q_{SC} of the TENG after 5 min heat preservation at different temperatures. Inset is the diagram of the working model of the TENG. (D) Q_{SC} evolution with time under high temperatures.

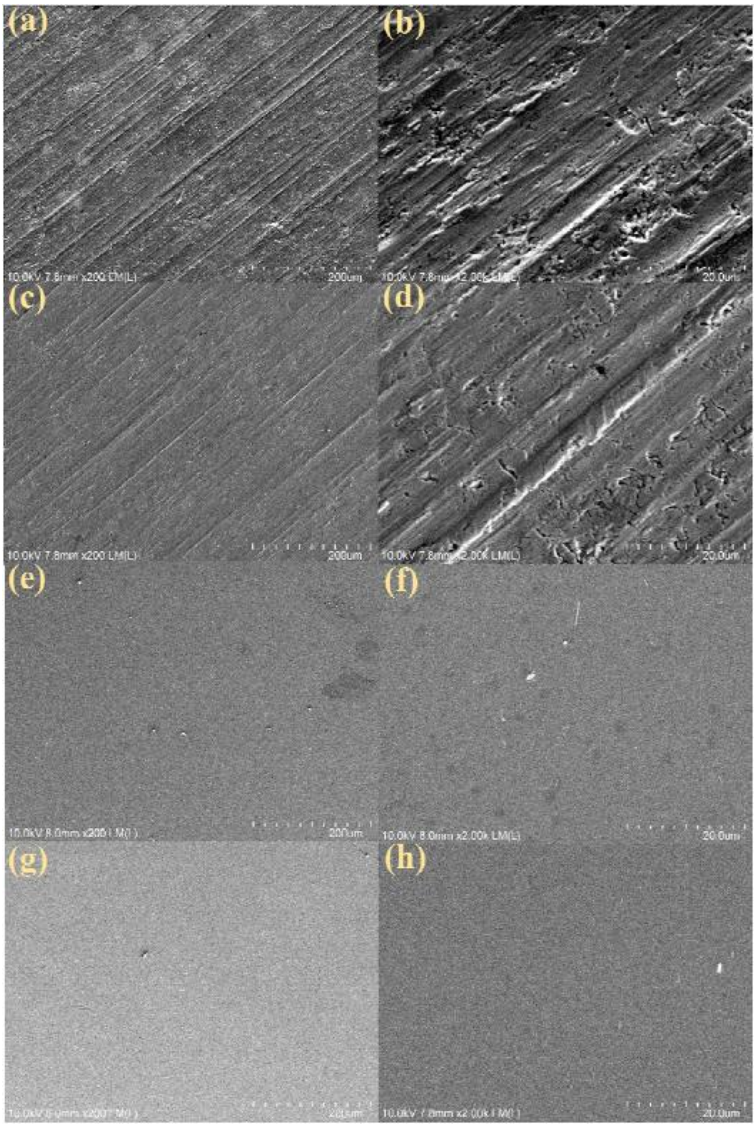

Figure 7. SEM images of the material surfaces before and after CE for twenty thousand circles. Ti foil magnified 200 times (a) and 2000 times (b) before CE, Ti foil magnified 200 times (c) and 2000 times (d) after CE, SiO2 magnified 200 times (e) and 2000 times (f) before CE, and SiO2 magnified 200 times (g) and 2000 times (h) after CE. The scale bars are 200 μm for (a), (c), (e) and (g), and 20 μm for (b), (d), (f) and (h).

It is worthwhile to note that the aforementioned experiments are the results after holding the TENG at different temperatures for 5 min. In order to further systematically explore the effect of temperature on Q_{SC}, long-term measurements were conducted on the TENG under various temperatures. **Figure 6d** shows long-term charge decay under high

temperatures, which indicates that the increase of temperature facilitates charge decay. It also reveals that the Q_{SC} response is analogous to exponential decay under high temperatures. In addition, taking the temperature of 503 K as an example, all of Q_{SC}, V_{OC} and short-circuit current I_{SC} share the same decay characteristics, which features a slow-fast-slow trend in decay speed (**Figure 8**).

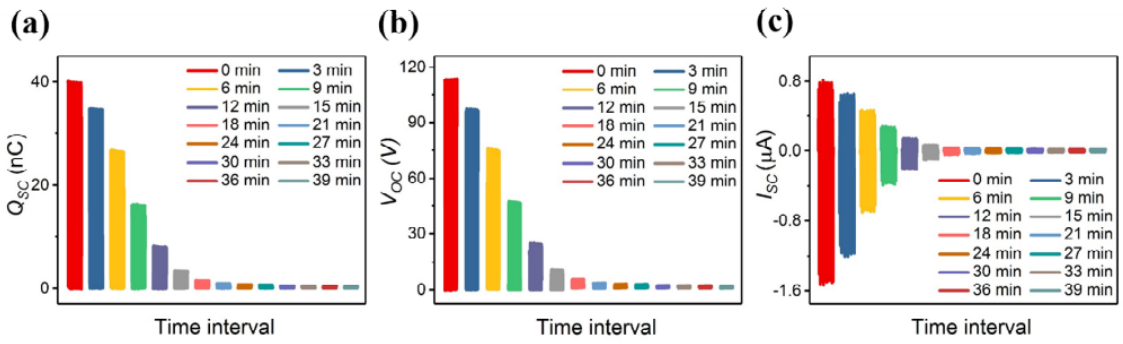

Figure 8. Performance of the Ti-SiO_2 TENG at 503 K. Q_{SC} (a), V_{OC} (b) and I_{SC} (c) evolution with time.

3.1.2.2 Theoretical Simulated Data for the Ti-SiO_2 TENG

To estimate whether charge decays are consistent with the electron thermionic emission model, the measured Q_{SC} values are fitted according to the thermionic emission equation:[61, 62]

$$J = \lambda A_0 T^2 e^{\frac{-W}{kT}} \left[e^{\frac{\Delta W}{kT}} - 1 \right] \quad (3)$$

where J is the current density, λ is the material-specific correction factor, A_0 is Richardson constant of a free electron, T is the temperature, W is the height of the potential barrier, k is Boltzmann constant and ΔW is the potential barrier height variation due to the surface

electric field *E*. Since $E \propto \frac{\sigma}{\varepsilon_0} \propto Q_{SC}$ (supporting online material text), we may assume that

$\Delta W=\lambda_1 Q_{SC}/\lambda$. ($\lambda_1$ is a constant). When $\Delta W << kT$, $e^{\frac{\Delta W}{kT}} - 1 \approx \frac{\Delta W}{kT}$, then

$$J = \frac{\lambda_1 A_0}{k} T e^{\frac{qV}{kT}} Q_{SC} \tag{4}$$

or equivalently:

$$\ln\left(\frac{J}{A_0 T}\right) = -\frac{qV}{kT} + \ln\left(\frac{\lambda_1}{k} Q_{SC}\right) \tag{5}$$

where q is the electronic charge. By assuming $J = \frac{1}{A}\frac{dQ_{SC}}{dt} = SQ_{SC}$, where A is the surface area and S is used to replace $\frac{\lambda_1 A_0}{k} T e^{\frac{qV}{kT}}$, then:

$$Q_{SC} = e^{-SAt} Q_{SC0} \tag{6}$$

where Q_{SC0} is the initial value of Q_{SC}. According to Eq. (6), Q_{SC} follows an exponential decay during thermionic emission. Simulated charge decay curves at the temperatures of 413 K, 473 K and 533 K are shown in **Figure 9a-c**, respectively. It is found that the simulated data are consistent with the measured data, except for the Q_{SC} values during the initial few minutes. This inconsistency may be due to the temperature destabilization during the short-period heat preservation, which may result in a lower average temperature compared to the measured value.

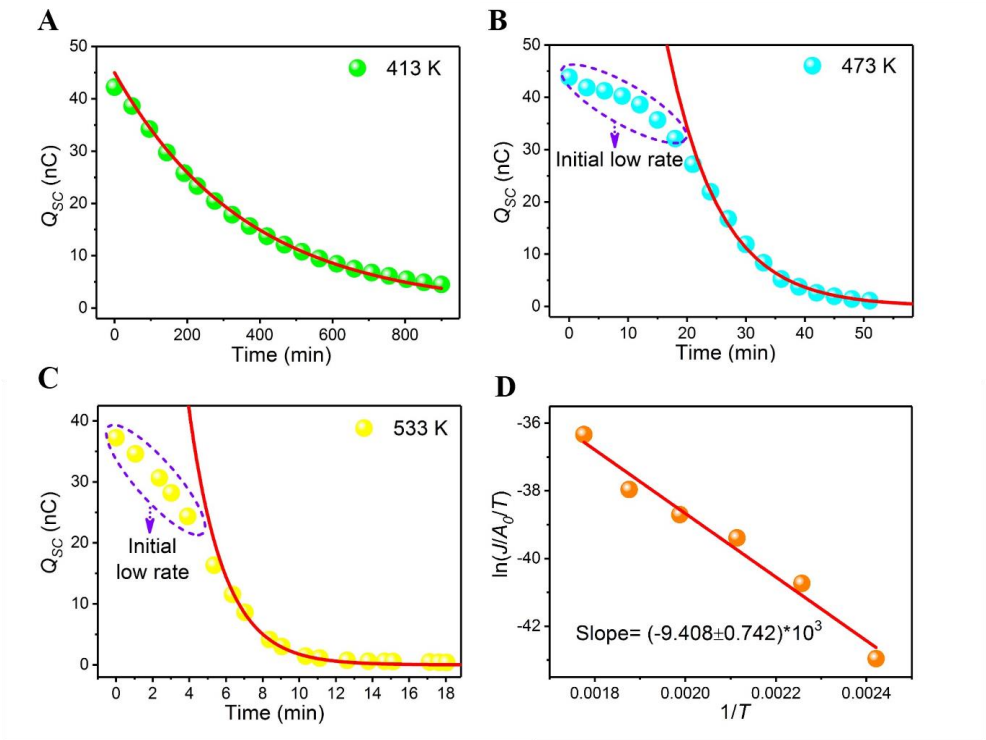

Figure 9. The measured (dots) and simulated (line) data of the Ti-SiO_2 TENG. Q_{SC} as a function of the time at various temperatures of (A) 413 K, (B) 473 K and (C) 533 K and (D) Plots of ln ($J/A_0/T$) against 1/T.

With the control experiments extending heat preservation from 5 min to 25 min under temperatures of 443 K and 473 K, both time-changing curves of Q_{SC} are much more consistent with exponential decay (**Figure 10**). In addition, according to Eq. (6), the plots of ln ($J/A_0/T$) against 1/T are shown in **Figure 9d**. These plots illustrate that the measured data fit the thermionic emission equation very well. The height of the barrier W is calculated to be 0.81±0.06 eV.

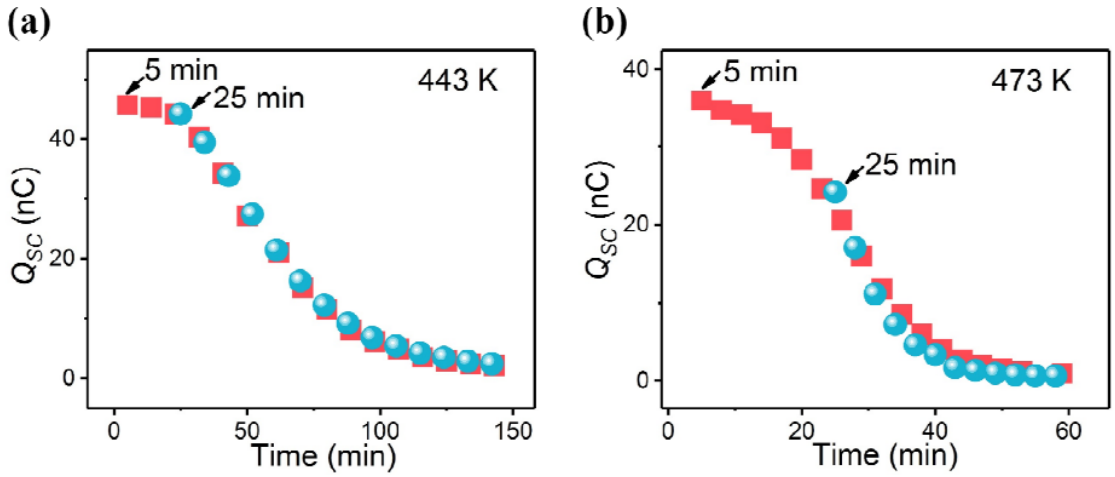

Figure 10. Effect of heat preservation time on Q_{SC} of the Ti-SiO_2 TENG under different temperatures. Q_{SC} evolution with time after 5 min or 25 min heat preservation under 443 K (a) and 473 K (b).

Moreover, if the thermionic emission mechanism is applicable here, the surface charge density/amount decay should be affected by the contact/separation status of the two surfaces, since CE may generate additional surface charges during the contact of the surfaces. Therefore, further experimentation was conducted to investigate how the status of the TENG affected the surface charge decay, as reflected by Q_{SC}. The effect of the contact/separation status of the two surfaces in four different cases before measuring Q_{SC} was studied (**Figure 11a**).

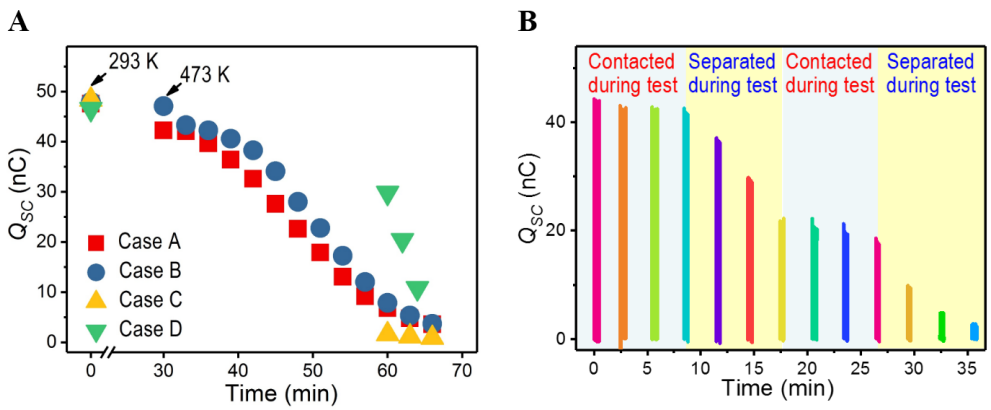

Figure 11. Contacting processes between Ti foil and SiO_2 on Q_{SC}. (A) The change of Q_{SC} with time in the four different cases outlined in Table 1. (B) Q_{SC} evolving with time when Ti foil either contacts or separates with SiO_2 during the interval of measurements.

Case A started with the two surfaces being separated at 293 K; and raised the temperature until 473 K, the temperature was maintained at 473 K for 5 min before testing. Case B started with the surfaces contacted at 293 K; and raised the temperature until 473 K, the temperature was maintained at 473 K for 5 min before testing. Case C and Case D were similar to Case A and Case B, respectively, but the maintenance time at 473 K increased to 35 min. These four cases are also described in **Table 1**.

Table 1. Status of Ti foil and SiO_2 in the four experimental cases.

Cases	Step 1: 293 K to 473 K	Step 2: 473 K	Step 3: 473 K
A	Separated for 25 min	Separated for 5 min	Did measurement
B	Contacted for 25 min	Contacted for 5 min	Did measurement
C	Separated for 25 min	Separated for 35 min	Did measurement
D	Contacted for 25 min	Contacted for 35 min	Did measurement

The measured Q_{SC} values in Case D are the largest for all of the cases; in other words, the contact status of the two surfaces slows down the discharge from SiO_2 surface. Conversely, the Q_{SC} values in Case C are the smallest, that is, the separation status of the two surfaces facilitates the discharge from SiO_2 surface. To further investigate this effect, we explored the decay of Q_{SC} at 473 K when the surfaces were kept either contacted or separated during the time periods for Q_{SC} measurements (**Figure 11b**). It is demonstrated directly that the Q_{SC} decay slowed down during contact, while the decay noticeably speeded up during separation.

Based on these results, we believe that the negative charges on SiO_2 surface are electrons rather than ions as follows. (i) In this study, the charges on SiO_2 surface were generated by PU-SiO_2 triboelectrification. It contradicts the conventional ion transfer model that dictates the material should contain at least mobile ions,[63, 64] since PU is a non-ionic polymer. McCarty and Whitesides correlated the ion transfer model to even non-ionic polymers, in which the hydronium and hydroxide ions were attributed to the water from the humid atmosphere: $2H_2O \rightleftharpoons H_3O^+ + OH^-$ (*29*). However, since the temperatures in our experiment are always higher than 373 K (the boiling point of water) and the local relative humidity is less than 1.5% in the furnace, the dominance of such an ion transfer model appears to be impossible; (ii) Assuming an unlikely situation that there are indeed some ions originated from PU itself during the CE, according to the ion transfer model demonstrated by Harper (**Figure 10**), these ions can transfer to the opposite Ti surface when the distance is less than 10 nm under a contacting status.[65, 66]

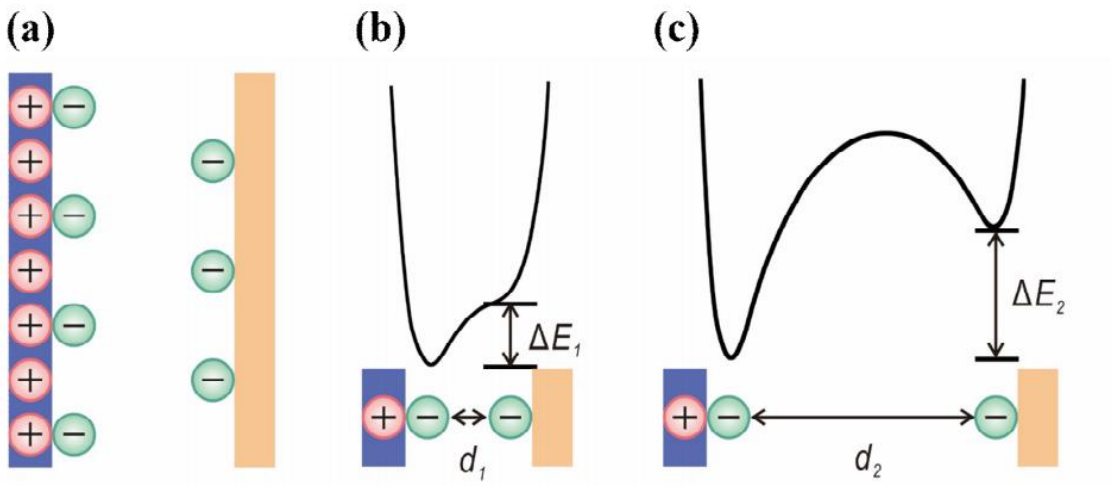

Figure 12. Schematic diagram of the barrier height based on ion transfer models. a) On the left surface there are covalently bound ions (positive) and mobile counterions (negative), and these counterions can move to the opposite right surface. b) When the two surfaces are close to each other ($d_2 > d_1$), the ion transfer becomes impossible due to the greatly increased barrier height ΔE_2.

Once the two surfaces are separated more, ion emission becomes a less plausible explanation due to the greatly increased barrier height, which will result in a slower Q_{SC} decrease under a separated status over that in a contacting status. Evidently, the above discussions contrast with our experimental results, so the ion transfer model cannot explain the phenomena we observed for inorganic solid-solid cases.

3.1.2.3 Experimental and Theoretical Simulated Results for the Ti-Al_2O_3 TENG

Another experiment was conducted to further verify the thermionic emission mechanism by replacing SiO_2 with Al_2O_3 to fabricate a Ti-Al_2O_3 TENG. It is noteworthy that with a better thermal conductivity and thinner thickness, a faster thermal equilibrium will be reached for Al_2O_3. The Q_{SC} (0.16 nC) and the V_{OC} (3.3 V) generated by the Ti-Al_2O_3 TENG at 293 K are also very low (**Figure 13**), which can be ignored during testing.

Similar to that of the Ti-SiO_2 TENG, an initial charge amount of around 12 nC was introduced by PU-Al_2O_3 triboelectrification before the TENG operation.

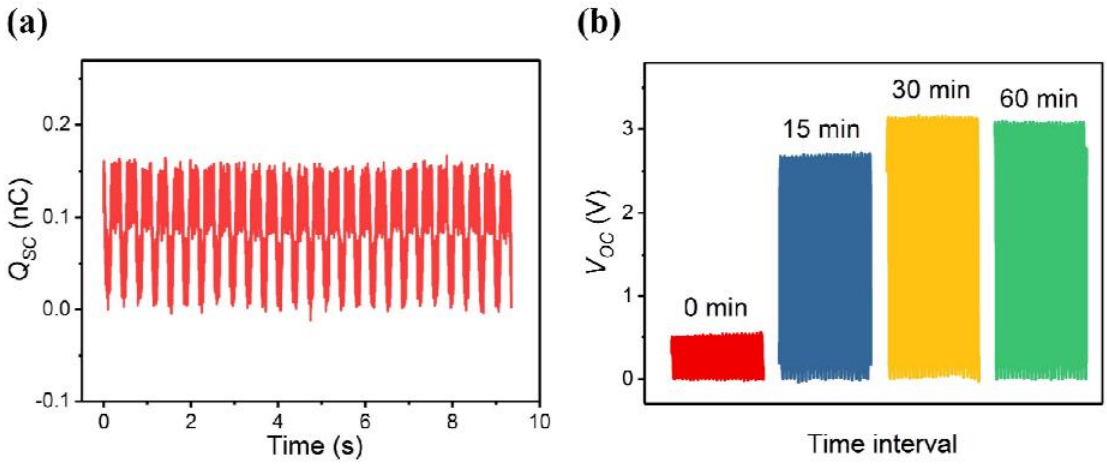

Figure 13. CE of the Ti-Al_2O_3 TENG at 293 K. Q_{SC} (a) and V_{OC} (b) changes with the operation time increase.

Following this, the temperature was increased and held for 5 min to measure the Q_{SC} variation. **Figure 14a** demonstrates that the residual charges decrease more rapidly at higher temperatures. The inset in **Figure 14a** shows the variations of Q_{SC} at 353 K, 443 K and 533 K, indicating that at 533 K, the charges decay rapidly to around 1 nC. **Figure 14b** shows the long-term charge decay of the Ti-Al_2O_3 TENG at different temperatures.

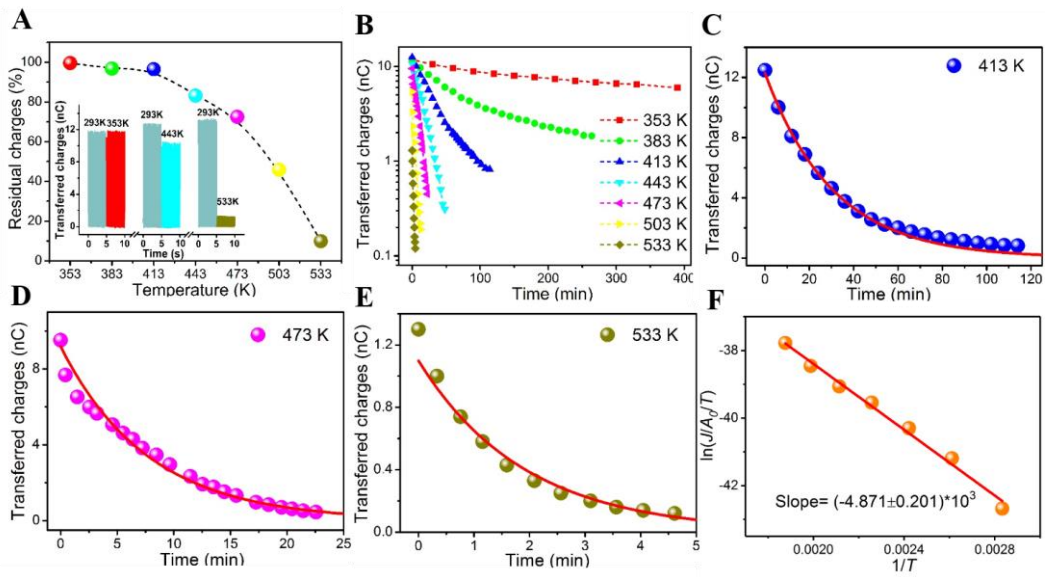

Figure 14. Experimental and simulated data of the Ti-Al_2O_3 TENG. (A) The percentage of residual charges of the TENG at different temperatures. The residual charges are the Q_{SC} of the TENG after 5 min heat preservation at different temperatures. Inset is the change of Q_{SC} at various temperatures. (B) Q_{SC} evolution with time at different temperatures. (C), (D) and (E) The measured (dots) and simulated (line) Q_{SC} as a function of the time at various temperatures of 413 K, 473 K and 533 K. (F) Plots of ln ($J/A_0/T$) against 1/T.

The experimental results are fitted to an exponential decay, which is similar to the data of the Ti-SiO_2 TENG, and the Q_{SC} decays faster at higher temperatures. A little difference is that, taking the temperature of 503 K as an example, all of Q_{SC}, V_{OC} and I_{SC} share the same fast-slow trend in decay speed (**Figure 15**). It further confirms that the slow-fast-slow trend in decay speed of the Ti-SiO_2 TENG performances is due to the temperature destabilization. **Figure 14c-e** show the measured and simulated Q_{SC} decays at temperatures of 413 K, 473 K and 533 K. The data from the Ti-Al_2O_3 TENG evidently fit to the theory even better than that of the Ti-SiO_2 TENG. **Figure 14f** shows the plots of ln ($J/A_0/T$) against 1/T, which demonstrates that the charges on Al_2O_3 are also consistent with the thermionic emission equation, with a lower potential barrier of 0.42±0.02 eV.

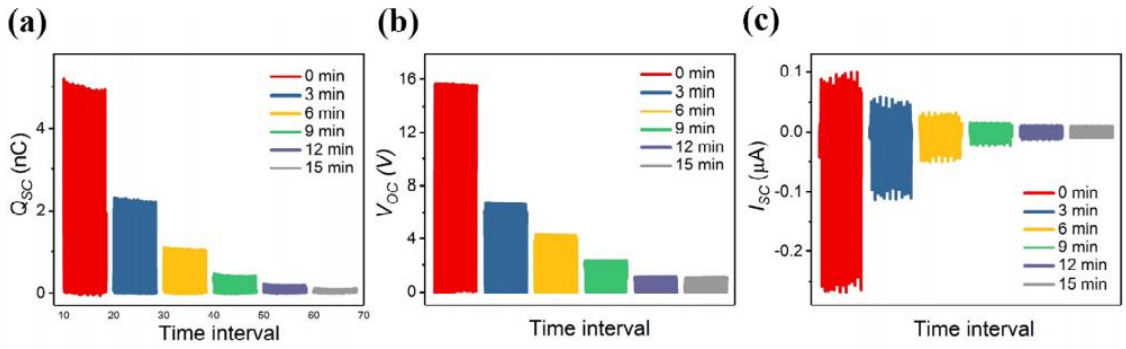

Figure 15. Performance of the Ti-Al_2O_3 TENG at 503 K. Q_{SC} (a), V_{OC} (b) and I_{SC} (c) evolution with time.

3.1.2.4 Ruling out the Ion Transfer Mechanism

Herein, we further discuss why the ion transfer mechanism fails to explain the CE data presented above for inorganic solid-solid cases. As shown in **Figure 11**, it verifies that the mechanism of the surface discharging follows the electron thermionic emission model, which rules out the possibility of ions as the charge carriers in CE. In addition, the ion transfer model satisfies the Boltzmann distribution,[63] which indicates that more triboelectric charges would be transferred at higher temperature. However, experimental results demonstrated that there were only less charges being transferred during triboelectrification at higher temperatures.[60] Furthermore, since the water plays a very important role in the ion transfer model,[67, 68] here we make more discussions. Nguyen *et al.* demonstrated that there were less charges being transferred at higher moisture level and the maximum charge transfer occurred at ~0% relative humidity.[69] Baytekin *et al*. further verified CE did not need the presence of water to occur by providing a water-free environment using paraffin oil.[70] Moreover, Wen *et al*. found that the CE of Al-PTFE could generate electricity at 500 K[71] and by using our high-temperature-resistant TENG, the CE of Ti-Al_2O_3 could happen even at 623 K (**Figure 16**). Recent studies by Wang *et al.*

indicated CE at a vacuum of 10^{-6} torr was five times higher than that at one atmosphere pressure.[72] All of these phenomena indicate that water is not necessary for CE and the ion transfer mechanism fails to explain the CE observed on larger surfaces.

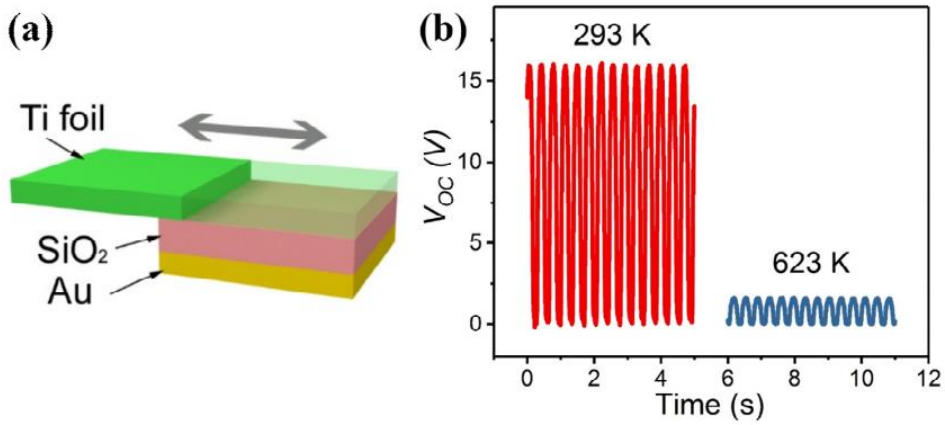

Figure 16. The structure of the sliding mode Ti-SiO_2 TENG (a) and the V_{OC} at 293 K and 623 K.

On the other hand, more recent studies support the electron transfer mechanism. As demonstrated by scanning Kelvin probe microscopy (SKPM), the sign of the transferred charges in CE could be reversed by applying an electric field.[73] Further studies found that the work required to separate the charged surfaces was comparable to the fracture energies of materials, which revealed that the electrification was associated to the interactions in electron clouds.[74] These studies indicate that the electrification is strongly related to the electron transfer during the overlap of the electron cloud and the formation or fracture of the bonds, which further rule out the ion transfer mechanism. Therefore, we believe that CE is dominated by electron transfer in the case of solid-solid pairs.

3.1.2.5 A Modified Surface States Model

The surface states model[75, 76] has been proposed to illustrate the fundamental charge transfer process in CE between a metal and a dielectric (semiconductor). **Figure 17** is a diagram showing the energy band before the mutual contact between a metal and a dielectric.

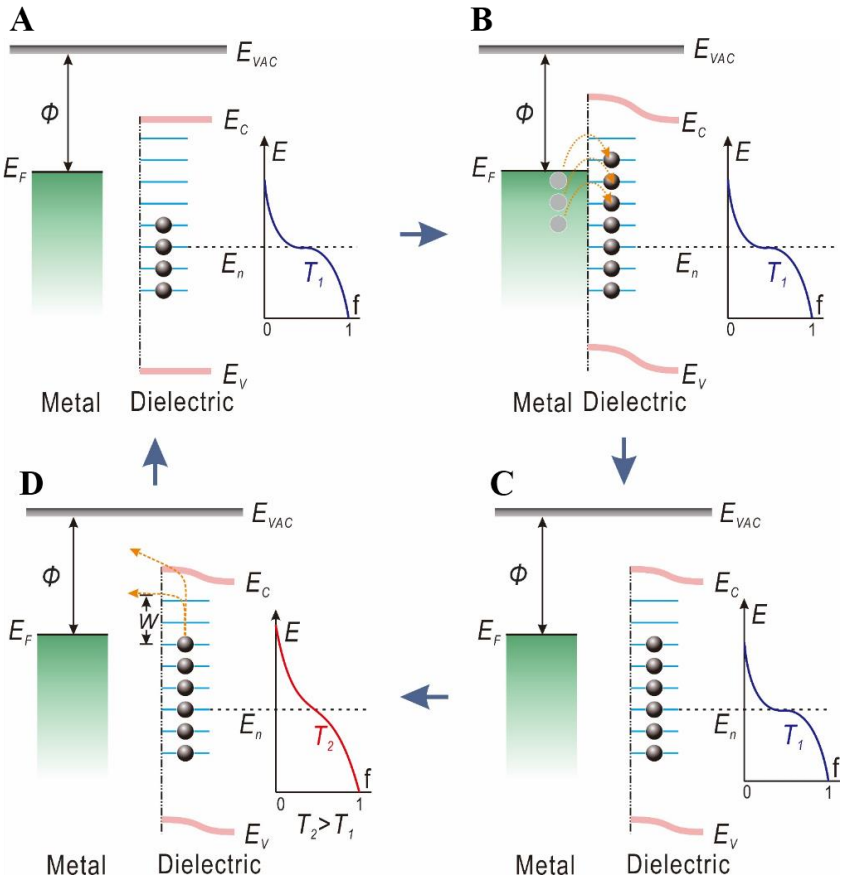

Figure 17. Modified surface states model for explaining the charge transfer during and after CE for the case of metal-dielectric pairs (semiconductor). The CE for a metal and a dielectric (A) before contact, (B) in contact and (C) after contact and (D) Charge release. Φ, metal work function; E_F, Fermi level; E_{VAC}, vacuum level; E_C, conduction band; E_V, valence band; E_n, neutral level of surface states; $f(E)$, Fermi-Dirac distribution probability; W, potential barrier; T_1 and T_2, temperature.

Despite the comparatively large equivalent band gap of the dielectric, its highest filled surface energy states are usually lower than the Fermi levels E_F of metals, considering

fewer electrons remain in the surface states. It should be noted that in this modified model, the electrons are conformed to the Fermi-Dirac distribution function:

$$f = \frac{1}{\exp^{(E-E_F)/kT}+1} \tag{7}$$

where f is the probability that an electron has energy E, E_F is the energy of the Fermi level, k is Boltzmann constant and T is the temperature. According to Eq. (8), at T_0 (T_0=0 K, absolute zero) the electrons will fill up all available energy states below the level of E_F. At a high temperature T_1 (T_1>T_0), some electrons are elevated to above the Fermi level. When the metal is in contact with the dielectric, those electrons with high energy in the metal hop up into the surface states of the dielectric. According to the Fermi-Dirac distribution, the filled surface energy states of electrons may be slightly higher than the E_F of the metal (**Figure 17b**). After being separated, the transferred charges create an electric field between the metal and the dielectric, which enables part of electrons that are at higher surface energy states flow back to the metal from the dielectric surface (**Figure 17c**). At a significantly higher temperature T_2 (T_2>T_1), the hopping of the electron becomes much easier to overcome the potential barrier W (**Figure 17d**). This explains why the charges accumulated at the surface cannot completely escape after the two surfaces are separated.

3.1.2.6 The Electron Cloud-Potential Well Model

It is noteworthy that, although the aforementioned surface states model can be used to explain the mechanism of CE of metal-semiconductor and metal-insulator, there are still some difficulties in explaining CE of metal-polymer and polymer-polymer pairings. The reason is that the surface states model originates from the band structure theory of

semiconductors, which is not the case for polymers and non-crystalline materials. To address this issue, an electron cloud/potential model based on fundamental electron cloud interactions is proposed to explain all types of CE phenomena for general materials (**Figure 18**).

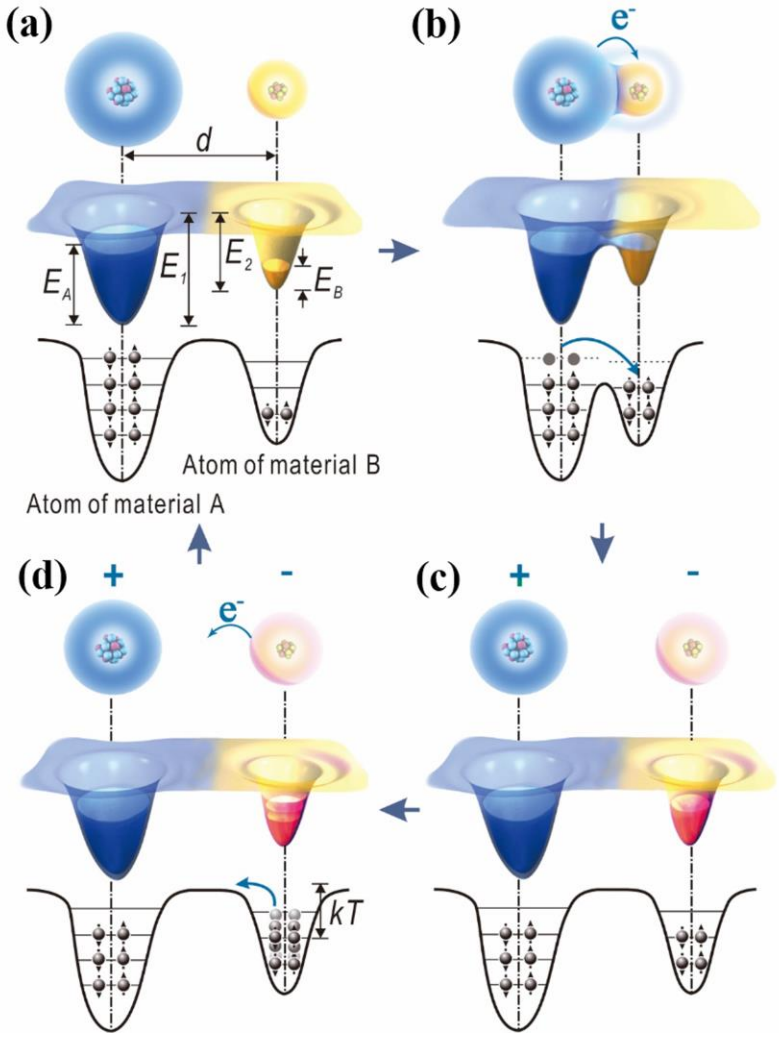

Figure 18. An electron cloud-potential well model proposed for explaining CE and charge release. The status of the electron cloud and potential energy of the two materials (A) before contact, (B) in contact and (C) after contact and (D) Charge release at an elevated temperature *T*. *d*, distance between electron clouds; E_A and E_B, occupied energy levels of electrons; E_1 and E_2, potential energies for electrons to escape; *k*, Boltzmann constant; *T*, temperature.

Here, the electron clouds are formed by electrons that are spatially localized within specific atoms or molecules, and occupying specific atomic or molecular orbitals. An atom can be represented by a potential well in which the out shell electrons are loosely bounded, forming an electron cloud of the atom or molecule. As shown in **Figure 18a**, *d* is the distance between electron clouds, and E_A and E_B are the occupied energy levels of electrons in materials A and B, and E_1 and E_2 are the required potential energies for electrons to escape from the surfaces of materials A and B, respectively. E_A and E_B are respectively smaller than E_1 and E_2. Before the contact of the two materials, the electrons cannot transfer due to the local trapping effect of the potential wells. When material A contacts with material B, the electron clouds overlap due to the "screening" between the two materials introduced in physical contact, and the initial single potential well becomes an asymmetrical double-well potential allowing the electrons to hop from material A to material B (**Figure 18b**). To some extent, this asymmetric double-well potential is similar to the potential curve for the initial formation of a hydrogen bond between OH and H[77] or for proton motion in the NHN^+ system.[78] After the separation of materials A and B, most of the electrons transferred to material B will be kept due to the energy barrier E_2 present in material B if the temperature is not too high (**Figure 18c**). Therefore, the CE occurs resulting in the positively charged material A and negatively charged material B. **Figure 18d** shows the charge releasing process at an elevated temperature *T*. As the temperature rises, the energy fluctuations of electrons become larger and larger as *kT* increases. Thus, it is easier for electrons to hop out of the potential well, and they either go back to the material where they came from or emit into air. This model further clarifies why the electrons generated from CE can be maintained due to the existence of potential barriers

that exist for all types of materials. In general material cases, we propose that, using our model, electron transfer dominates the CE process, and in parallel, ion transfer may also occur, but it is a minor process especially for non-ionic materials.

3.1.3 Conclusion

In conclusion, we introduced a new method to quantitatively investigate the real-time charge transfer using the outputs of a TENG, which revealed that electron transfer was the dominating mechanism for CE. We show that charge transfer follows an exponential decay at high temperatures for a variety of TENGs, which is consistent with the theory of electron thermionic emission. An electron cloud-potential well model is proposed based on the electron emission dominated charge transfer mechanism for understanding CE of all types of materials, which is more applicable to polymer materials and non-crystalline materials than existing models for CE. Our study may provide a new approach for understanding CE, which has been a well-known and debated phenomenon for thousands of years.

3.1.4 Experimental Section

3.1.4.1 Fabrication of the TENGs

Ti foil (99.7%) with a thickness of 0.0032 cm was purchased from Sigma Aldrich. SiO_2 (99%) with a thickness of 0.3175 cm was purchased from Technical Glass Products. Its thermal conductivity was 1.4 W mK^{-1} (293 K) and the dielectric constant was 3.75 (293 K, 1 MHz). Al_2O_3 (96%) with a thickness of 0.0635 cm was purchased from MTI Corporation. The thermal conductivity was 24 W mK^{-1} (293 K) and the dielectric constant

was 9.8 (293 K, 1 MHz). Polyurethane foam was purchased from McMaster-Carr. Polytetrafluoroethylene (PTFE) film and Kapton film were purchased from American Durafilm. The structure of the Ti-SiO_2 TENG was shown in **Figure 6a**. The Ti foil and SiO_2 were used as the electrification materials. Au coating with a thickness of 300 nm was deposited on the back of SiO_2 as the electrode by using a Denton Explorer E-beam Evaporator. The deposition rate of Au coating was 0.2 nm s^{-1}. After the Au deposition, SiO_2 was annealed at 673 K for 4 h in the air. This SiO_2 with Au coating was positioned on an insulating and high-temperature-resistant ceramic plate. In order to eliminate the interference of the metal to the testing process, an insulating ceramic plate was specially added between the Ti foil atop the SiO_2 and steel holder.

For the Ti-Al_2O_3 TENG, the SiO_2 with Au coating was replaced by Al_2O_3 with the same thickness Au coating. The structure of the Ti-Al_2O_3 TENG was similar to that of the Ti-SiO_2 TENG except SiO_2 was replaced by Al_2O_3. For the SiO_2-Al_2O_3 TENG, the structure was similar to that of the Ti-Al_2O_3 TENG except Ti foil was replaced by SiO_2 coated with Au. The structures of the Ti-PTFE TENG and Ti-Kapton TENG were similar to that of the Ti-SiO_2 TENG except SiO_2 was replaced by PTFE coated with Au and Kapton coated with Au, respectively.

3.1.4.2 Measurement of the TENGs

The TENG was placed in a heating cabinet (Barnstead/Thermolyne 6000 furnace), which provided the desired temperature with an accuracy of ±5 K. The heating rate of the cabinet was about 7.5 K min^{-1}. The top of the steel holder on the TENG extended out of the open hole on the heating cabinet and was connected to a computer programmed linear

motor. Between the steel holder and the linear motor, a ceramic connector was added for preventing the heat from damaging the linear motor. Nickel wires were attached to the surfaces of Au electrode and Ti foil and extended out of the heating cabinet. The environmental relative humidity was less than 30%. During the TENG performance measurement, the linear motor provided an accurate control of position and speed for the mechanical stimulation, and the heating cabinet controlled the temperature. The separation distance between the tribo-materials was 0.24 cm. The loading frequency was 2.7 Hz and the loading force was about 2.1 N. The effective areas of the Ti-SiO_2 TENG, Ti-Al_2O_3 TENG, SiO_2-Al_2O_3 TENG, Ti-PTFE TENG, and Ti-Kapton TENG were 21, 18, 15, 10, and 10 cm^2, respectively. The relative humidity was measured by a Shaw Superdew 3 hygrometer. The loading force was measured by a Vernier LabQuest Mini compression dynamometer. The short-circuit transfer charge Q_{SC}, open-circuit voltage V_{OC}, and short-circuit current I_{SC} of the TENGs were measured by a Keithley 6514 electrometer. The microscopy images of Ti foil and SiO_2 surfaces before and after contact-electrification were measured by a Hitachi SU8010 field-emission SEM.

3.2 Comparing Contact-Separation and Sliding Mode Triboelectric Nanogenerators at High Temperature Operation

3.2.1 Introduction

Efforts to establish a universal explanation of contact electrification (CE) have spanned many centuries, and yet our understanding of this commonplace phenomenon remains to be explored. Existing theories involving CE are highly material-dependent, and there lacks an agreement on an all-inclusive, dominant mechanism of CE. One primary example of this is the debate over whether the charges transferred between surfaces in metal-dielectric and dielectric-dielectric CE are electrons or ions, which has been ongoing since the early 20th century.[65, 79, 80] Well-established studies from the mid-20th century suggest that metal-metal CE is electron-dominated and dependent on the work function, the Volta potential difference, or the electrostatic potential difference between two metals in contact.[41, 42, 52] Due to charged surfaces being in a non-equilibrium state, the significant impact of contaminants, and the influence of varying length and time scales, a universal model for metal-dielectric and dielectric-dielectric CE is a challenge yet to be resolved.[43, 81] Dielectric surface states and barrier heights have been widely accepted as entities involved in metal-dielectric charge transfer and retention, and many endeavors to theoretically characterize these processes using density functional theory measurements and electrochemical reduction reactions have been made, yet discrepancies between proposed universal models still persist.[43, 45, 46, 75, 82-84] Recently, extensive progress has been made on this front, owing to the systematic measurement of metal-dielectric CE through real-time temperature-dependent TENG studies, which provides a new method for exploring CE.

Nanogenerators have been one of the fastest-growing fields in energy research since their inception in 2006, and have given rise to a great deal of energy harvesting and sensing applications rooted in the Maxwell displacement current.[2, 4, 25, 85-87] In addition to making water energy,[19, 58] wind energy,[14] and biomechanical/ambient energy harvesting[15, 24, 88] for self-powered electronics with ultra-high efficiency[16, 31, 72, 89, 90] and self-powered active sensors[3, 23, 25, 26, 57, 60, 91] possible, TENGs have been instrumental in theoretical studies on the origin and workings of CE.[4, 6] A variety of TENG studies that suggest that electrons are the dominant CE transferred charge identity have been performed, including those based on the photoelectron emission model[92] and Kelvin force probe microscopy.[93-95] Moreover, a quantum mechanical model for electron transfer for dissimilar and separated atoms has been proposed.[96] Of particular note are our recent studies that demonstrated the thermionic emission of electrons and subsequent exponential decay of surface charge from the surfaces of contact-separation mode Ti-SiO_2 and Ti-Al_2O_3 TENGs at high temperatures.[97] The generation of surface charge of TENG operation was maintained until temperatures rose above 413 K, above which exponential charge decay began to be observed. The decay patterns were correlated to the electron thermionic emission model, suggesting electrons as the dominant charge identity in CE, and a metal-semiconductor surface states model and dielectric/metal-dielectric electron cloud potential well model were proposed.[98] Thermionic emission is a key phenomenon in explaining the reasoning behind electron-dominated CE, and involves heating a material so that electrons gain enough thermal energy to overcome the work function and in turn, emit from the material. Few studies have been conducted on how to prevent or counteract this effect, and therefore further investigation on its involvement in high temperature TENGs is needed. An efficient TENG

that consistently generates power under high temperatures has recently been developed, and indeed, the sliding mode was determined to be the best operational mode, assisted by metal supports so as to increase tight contact between triboelectric materials and quench the effects of thermionic emission.[40] The reasoning behind why the sliding mode TENG operated more efficiently at high temperatures is a pressing question in the development of related applications, and one that is furthered through this study.

Figures of merits have revealed that discrepancies between different TENG operating modes (contact-separation, sliding, freestanding triboelectric layer, single electrode contact) include their charging behavior, maximum output energy per cycle, energy conversion efficiencies, and average output power.[9] Charging behavior has been found to be different between different modes of contact in CE, including sliding, rolling, and contact-separation,[99] warranting further investigation in order to develop a more universal model of CE. There have been few studies comparing contact-separation and sliding CE in depth, but more exist that compare sliding and rolling CE due to their importance in industrial granular processes. For instance, rolling particles have been found to have less fall off of charge transfer with contact time, due to the tendency of the entire surface of a particle to come into contact through a randomized fashion, including charged and uncharged areas.[100] Discharge has been suggested as the limiting factor of contact-separation or "bouncing" particle CE as compared to continuous sliding/rolling CE. Additionally, sliding motions of cylindrical grains were found to produce less charge transfer than rolling spheres, despite spherical grains having fewer triboelectric charges on their surface than cylindrical grains due to minimization of surface area.[101] This shows that despite the saturated charge being the same for sliding and rolling friction systems,[102] the

operational mode has a profound effect on overall efficiency of CE. As a vital mode of operation for TENGs in terms of versatility in energy harvesting and sensing applications, lower volume required, and uniquely efficient performance in harvesting motion, sliding mode CE is a phenomenon that begs more investigation.

Herein, we report our findings build upon our previously suggested CE mechanism by incorporating surface charge data from a sliding mode Ti-SiO_2 TENG at high temperatures. Comparisons are made against the patterns of electron emission from thermal energy of the previous contact-separation mode Ti-SiO_2 TENG, and the cause for any discrepancies and similarities is scrutinized. Finally, a modified electron cloud potential well model for universal metal-dielectric and dielectric-dielectric CE is presented to incorporate the data from the sliding mode TENG. This chapter section interpolates material from a paper authored by the thesis author.[39]

3.2.2 Results and Discussion

3.2.2.1 Design and Performance of the Sliding Mode Ti-SiO2 TENG.

In order to maintain a valid comparison of our data to that from the contact-separation mode high-temperature study, a high temperature-resistant sliding variant of the previously used Ti-SiO_2 TENG was developed for this study.[97] Even though polymers are ideal materials for TENGs due to their flexible physical and chemical characteristics in exchanging charge, reducing wear, and minimizing friction, the selection of thermally stable polymers is limited in regards to our experiment.[103] Also, polymer-polymer contacts can experience intermittent motion, seizure, or stick-slip due to adhesion when tested in dry conditions.[104-106] This should not limit future high temperature studies to be performed on thermally stable polymers such as thermosets, since triboelectrification was found to

not be directly related to friction.[102] However, friction, wear, and energy consumption of sliding materials can be affected by the presence of surface charges due to increased attractive forces between them.[107] Attracting impurities and causing wear can quickly degrade the performance of CE, and regularity of motion and minimal wear of the material should be maintained for best results.

Our testing setup was designed to support a controlled vertical sliding motion between the triboelectric pair surfaces (**Figure 19a**), which were secured on heat-resistant mica ceramic plates by clamps, with one side being a sputtered Au electrode and a SiO_2 sheet that was optionally charged using a polyurethane (PU) foam, and the other being Ti foil (**Figure 19b-c**). The usage of PU foam to pre-charge the SiO2 surface is not only to mirror the previous contact-separation study, but to also provide enough charges for any temperature effects on these surfaces to be apparent. The addition of foam to the contact-separation study was necessary, as the room temperature output was 0.45 nC for short-circuit charge transfer Q_{SC}, indicating that the surface charges generated by contact-separation were inadequate to visualize the effects of thermionic emission.[97]

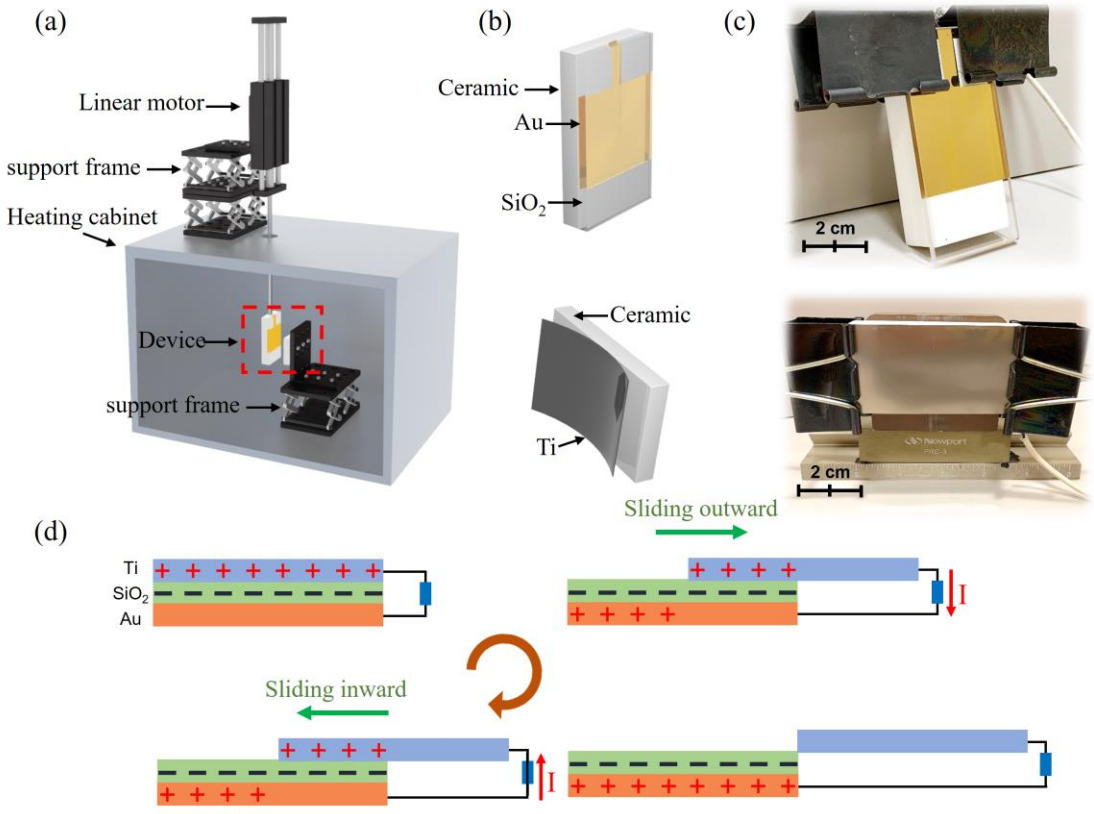

Figure 19. Setup of the high-temperature measurement platform for TENGs. (a) Schematic illustration of the sliding mode Ti-SiO_2 TENG anchored with the heating cabinet and motor. (b)-(c) Enlarged view and optical photograph of the sliding mode Ti-SiO_2 TENG within the red-dashed frame in (a). (d) The working principle of the sliding mode Ti-SiO_2 TENG.

The triboelectric pair of SiO_2 and Ti have low power output as TENG materials, but are heat resistant and robust, and thus fitting for this study. These surfaces were aligned and stabilized with a stainless-steel framework in a heating cabinet, and a linear motor was positioned to vertically displace the mobile SiO_2 platform from alignment with the Ti foil then return it to the starting position at an operation frequency of 0.4 Hz. The Ti-SiO_2 sliding mode TENG produced an average open-circuit voltage V_{OC} of 70 V and short-circuit current I_{SC} of 116 nA per operation cycle at room temperature (**Figure 20**).

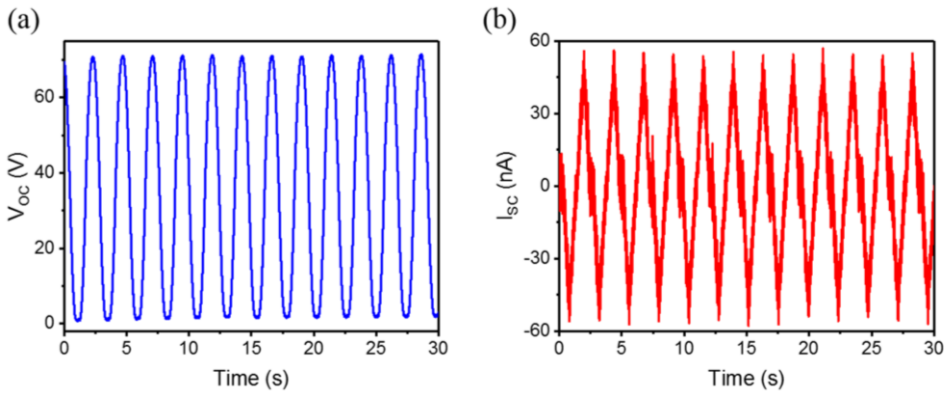

Figure 20. CE of the Ti-SiO_2 sliding mode TENG at 293 K. V_{OC} (a) and I_{SC} (b) of the TENG.

A Cu- polytetrafluoroethylene (PTFE) TENG of the same contact area and operation frequency was fabricated for comparison, and Q_{SC} and V_{OC} were 29 nC and 70 V for the Ti-SiO_2 TENG and 94 nC and 235 V for the Cu-PTFE TENG, respectively (**Figure 21**). Although the Ti-SiO_2 TENG's electrical output performance is less than one third that of the Cu-PTFE TENG, the materials were selected for their excellent durability, stability and comparative performance at different elevated temperatures in the preceding study.[97] Sliding CE varies between materials due to yield, deformation of surfaces, frictional heating, and material transfer, so our materials were chosen to minimize the effects of all of these.[108]

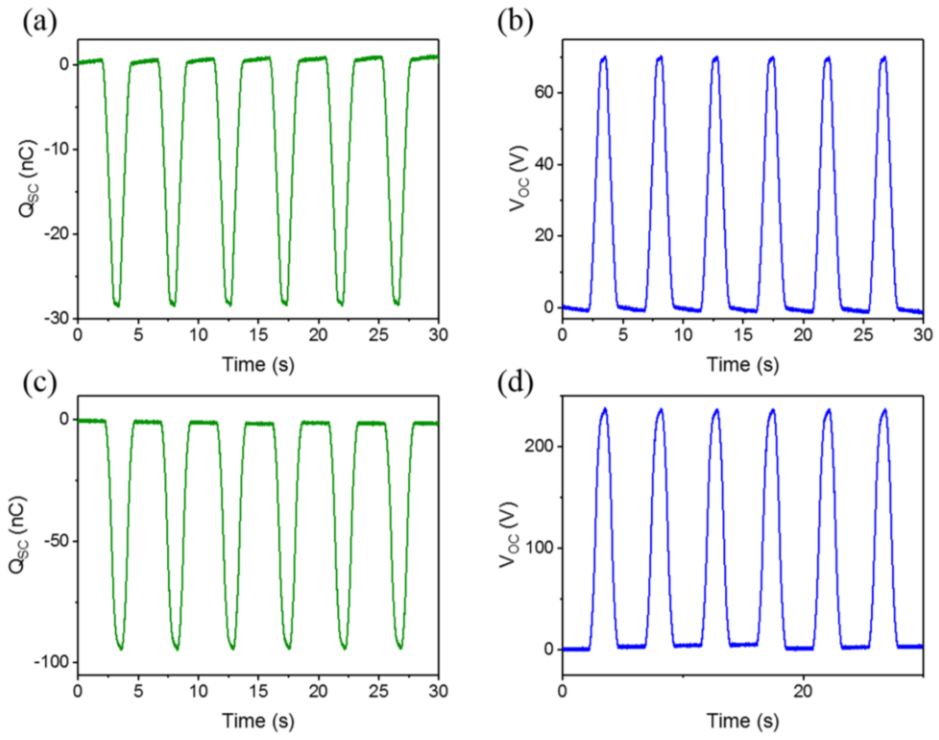

Figure 21. CE of the Ti-SiO_2 and Cu-PTFE sliding mode TENG. (a, b) Q_{SC} (a) and V_{OC} (b) of the Ti-SiO_2 TENG. (c, d) Q_{SC} (c) and V_{OC} (d) of the Cu-PTFE TENG.

The working principle of this sliding mode Ti-SiO_2 TENG is shown in **Figure 19d.** As the linear motor displaces the initially aligned Ti and SiO_2 surfaces, the spontaneously generated opposite charges on both surfaces are displaced as well, creating a potential difference between the Ti foil and Au electrode. This potential imbalance drives electrons to flow from the Au electrode to the Ti foil as the surfaces are continually displaced, neutralizing the charge of the exposed area of the Ti surface. At any given point of displacement, the amount of positive charges on the Au electrode is equal to the electrons transferred to the Ti foil. The portion of Ti still in contact with SiO_2 maintains its positive charge until both surfaces are completely separated by the motion of the motor. At this point, the displacement is reversed so the Ti comes into contact with SiO_2 again, generating

a spontaneous opposite charge on the area of Ti-SiO_2 contact and creating backflow of electrons to neutralize the Au electrode. The alternating current from this interchanging flow of electrons produces the electrical output of this sliding mode Ti-SiO_2 TENG.

3.2.2.2 Comparing the sliding mode and contact-separation mode Ti-SiO2 TENGs.

The short-circuit transferred charge Q_{SC} provides a real-time quantification of the electron flow between the Ti foil and Au electrode, and a sliding mode Ti-SiO_2 TENG with ~28 nC of initial surface charge on the SiO_2 surface shows a comparable amount of charges being transferred with each operation cycle at room temperature (**Figure 22a**). After instilling ~28 nC of surface charge on SiO_2, Q_{SC} was monitored over time while operating at a range of temperatures, and increasingly rapid decay was observed with increasing temperature (**Figure 22b**). This resulted in charge decay trends similar to those found at the same temperatures in our contact-separation mode Ti-SiO_2 TENG studies,[97] albeit on much longer time scales. Through comparing the individual Q_{SC} over time plots in **Figure 22c-h** from the sliding mode TENG measurements to those at the same temperatures from the contact-separation mode TENG study, we find that thermionic emission of electrons is less efficient at depleting Q_{SC} to below 1 nC and surface charges are retained for longer periods of time for sliding mode TENGs at temperatures below 503 K. However, it appears that for the sliding mode TENG at 413 K, 443 K, and 473 K, Q_{SC} decays rapidly during initial measurements, while the contact-separation mode TENG showed slower charge decay at the beginning followed by a sharper decline. Both operational modes of TENGs show a rapid initial decline of surface charge leading to exponential decay at 503 K and above.

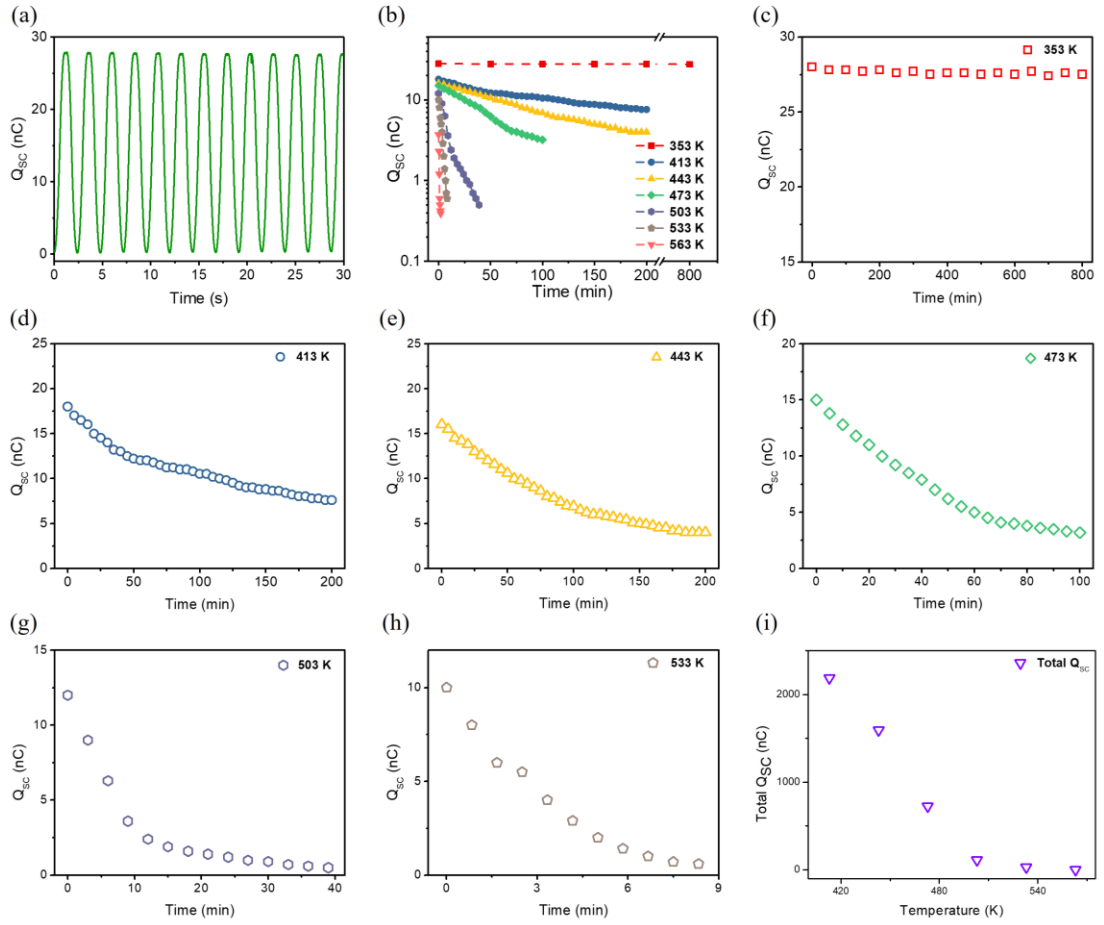

Figure 22. Performance of the Ti-SiO_2 sliding mode TENG at different temperatures with induced charge of -28 nC. (a) The total transferred changes at room temperature. (b-i) Q_{SC} evolution with time under different high temperatures: (c) 353 K, (d) 413 K, (e) 443 K, (f) 473 K, (g) 503 K, (h) 533 K. (i) Integration of the decay curves from Figure 23d-h, showing total Q_{SC} measured under different high temperatures ranging from 413 to 563 K.

By integrating over these curves to determine the total amount of surface charge collected over the measurement time, an apparent decline in this value is also observed in **Figure 22i** as temperature increases, which may be attributed to the thermionic emission of electrons from the surface due to thermal energy fluctuations overpowering the charge generation and transfer effect of the TENG. This plot excludes the integration over the measurement taken at 353 K, not only because the time scale is much larger than that of

the higher temperature measurements, but also because it is meant to show the evolution of the charge in states being directly affected by temperature effects. The relaxation time for charges also appears to shorten considerably as temperature increases, perhaps due to the greater mobility of charges from the surface until an equilibrium state is reached. The more immediate, sharper initial decay of Q_{SC} in pre-charged sliding mode TENGs below 503 K may result from less efficient generation of charges when pre-charged above a certain charge density due to saturation. Owing to the higher maximum displacement required for sliding to achieve the same maximum open-circuit voltage $V_{OC,max}$, the performance of a sliding TENG tends to be less efficient than that of a contact-separation TENG.[9] However, this does not explain the overall longer time scales for sliding mode charges to dissipate compared to contact-separation mode charges. To investigate this, measurement and analysis of charge retention without the influence of pre-charging is performed.

In order to evaluate the sliding mode Ti-SiO2 TENG's performance without initially induced charges on the surface, the charge on the triboelectric surfaces were eliminated using the process depicted in **Figure 23a**, in which ethanol and 2-propanol were applied and dried with Ar gas for three cycles per test. The measured Q_{SC} would then only be associated to the charges generated and transferred by the sliding mode TENG. In this case, even at the highest tested temperature of 563 K, the TENG was still able to increase the amount of transferred charges for a period of time through continual sliding interactions. The magnitude of transferred charges per TENG cycle decreases across the board as testing temperatures increase, as well as the period of time that charges can build up (**Figure 23b**). This collective plot differs greatly from the pre-charged measurements

from Figure 2b, due to the lack of pre-charged electrons on SiO_2 in order to demonstrate the sliding TENG's capability to charge surfaces even in very high temperatures. There is a shorter time scale required for the un-charged TENG measurements to reach a similar plateau Q_{SC} value as the pre-charged TENGs, aside from the 353 K measurement, since the TENG was able to retain all pre-charged electrons for that condition.

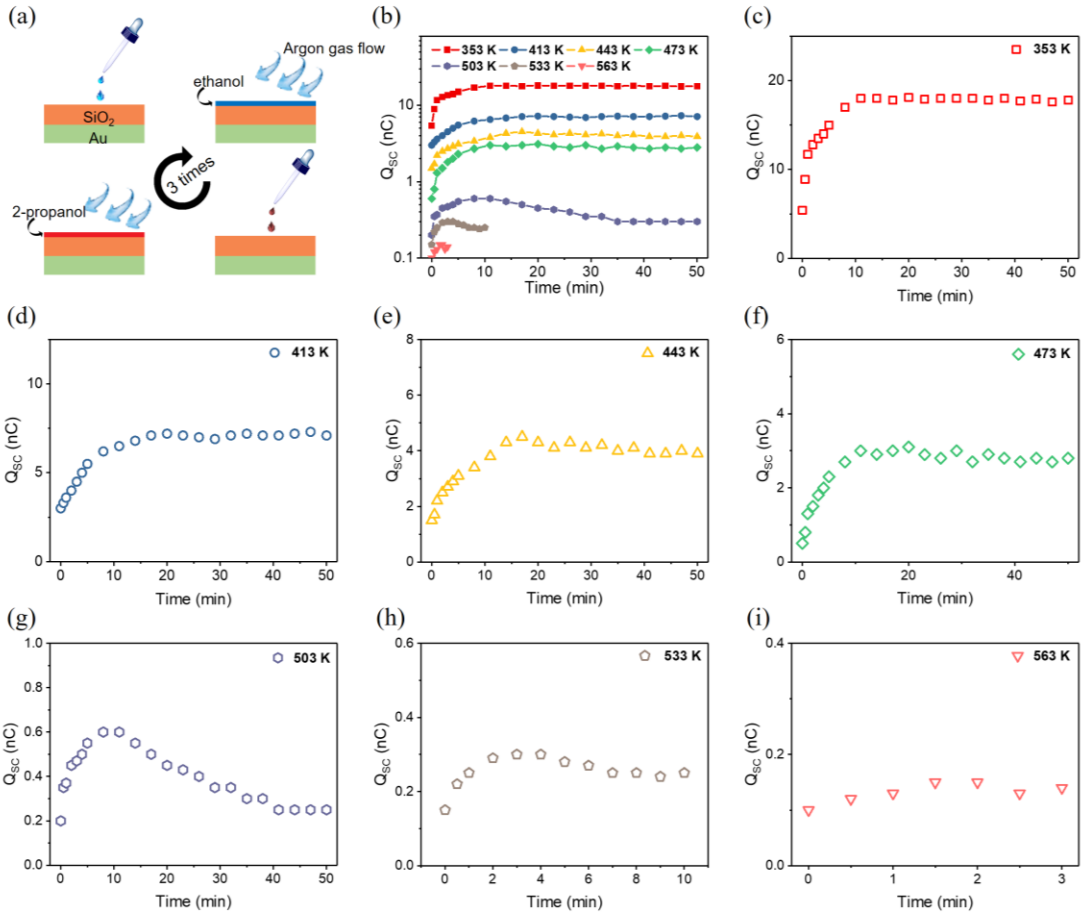

Figure 23. Performance of the Ti-SiO_2 sliding mode TENG at different temperatures without induced charges. (a) Process of eliminating the initial charges on the surface of SiO_2. (b-i) Q_{SC} evolution with time under different high temperatures: (c) 353 K, (d) 413 K, (e) 443 K, (f) 473 K, (g) 503 K, (h) 533 K. (i) 563 K.

The individual plots of Q_{SC} over time at increasingly higher temperatures (**Figure 23c-h**) show a decay pattern emerging at and above 503 K following an elevated period

from charge production by the TENG. The decrease is associated with thermionic emission overtaking the charge-generating mechanism of the TENG and causing a decrease in transferred Q_{SC}. The onset of this decay occurs earlier as temperature increases above 503 K, since electrons experience thermal energy fluctuations more rapidly at higher temperatures. The decay does not quite appear to be exponential or consistent in some of these cases aside from 503 K (Figure 3g), as the overall Q_{SC} measured at these temperatures is so close to 0 nC the change is less noticeable. At temperatures below 503 K, the repeated sliding displacement and reunion of triboelectric surfaces was sufficient to prevent dissipation of transferred charges from the exposed surfaces. The operation of the sliding mode TENG without initial charging was able to maintain TENG-produced charges more successfully at certain temperatures at which the pre-charged contact-separation mode TENG was unable to (e.g., 413 K, 443 K, 473 K).[97] Thereby, we suggest that the sliding mode is more efficient at generating and retaining charges at high temperatures when emission of electrons is at play, despite the lower figure of merits of sliding mode TENGs. These findings are supported by a recent systematic study on the maximal power of TENGs, which found that sliding-triggered TENGs are less limited by air breakdown and have higher energy density than contact-separation TENGs.[11] With the comparisons drawn from these results, TENGs for commercial applications have even more room to grow.

When contrasting the initially PU foam-charged samples with those that had charges eliminated from their surface, the Q_{SC} of initially discharged TENGs whose operation was able to overcome the influence of thermionic emission would plateau around the value that the initially-charged TENGs would reach after exponential decay occurred. Therefore, this value appears to be a saturation point tied to its corresponding temperature

and a Q_{SC} above or below it will eventually plateau at said value, although it takes longer for an over-saturated surface to lose charge and reach this point than an under-saturated surface to gain charge to this point. This is likely due to the efficient charge retention capability of the sliding mode Ti-SiO_2 TENG. Notably, the pre-charged sliding mode TENG had higher Q_{SC} output only at 353 K (**Figure 24**), but produced the same amount of Q_{SC} per operation cycle at higher temperatures and was not able to overcome thermionic emission like the uncharged sliding TENG.

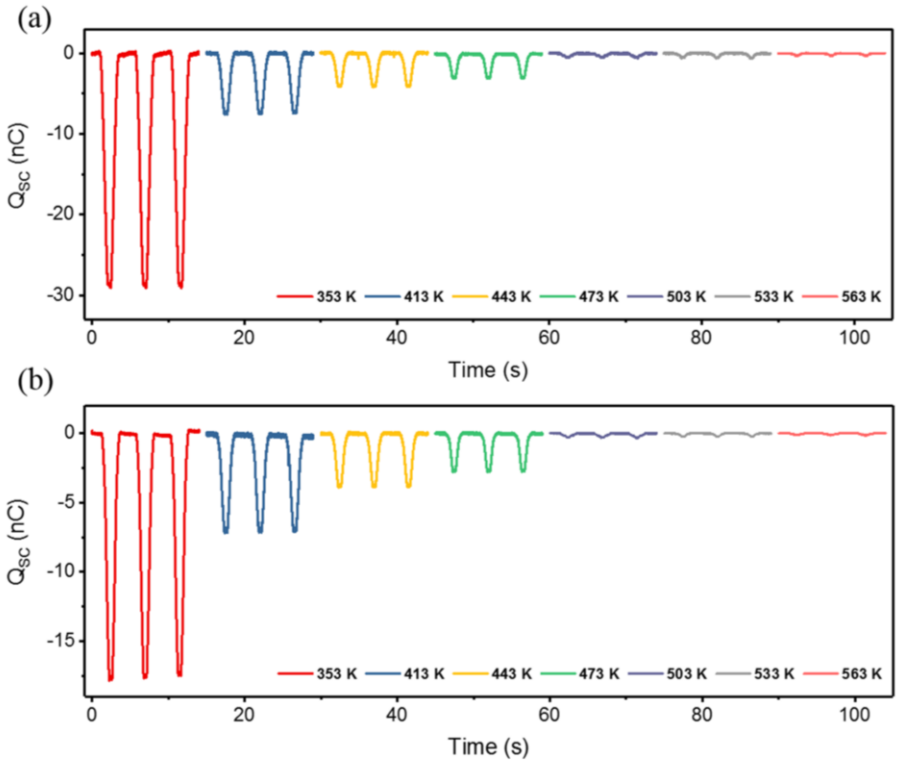

Figure 24. CE of the Ti-SiO_2 TENG (a) with induced charge of -28 nC and (b) without induced charge at different temperatures.

Additionally, the pre-charged and uncharged sliding mode measurements at 353 K do not reach the same plateau point as the other measurements do. This is due to the pre-charged SiO_2 measurement in **Figure 22c** retaining all of the pre-charged electrons since

thermionic emission has not occurred significantly at this temperature and the charges likely do not exceed the air breakdown limit. Therefore, they remain on the pre-charged SiO_2 surface throughout the TENG operation, which by itself can only generate what is measured in **Figure 23c**. If the pre-charged and uncharged sliding mode measurements were performed at temperatures lower than 353 K such as room temperature, the trends would likely match the data from the 353 K measurements. Whether pre-charged or uncharged initially, the closeness of surfaces sliding together more continuously has greater potential to prevent discharge or emission at high temperatures than when in an intermittently separated motion. Even so, discharge from dielectric surfaces is possible during the sliding process if voids or gaps of at least 1 μm are present,[109] so protection of surface charges from thermionic emission may not be maximized by changing operational mode alone.

3.2.2.3 Electron transfer corroborated by the sliding mode Ti-SiO2 TENG

In order to further implicate thermionic emission of surface charges and provide further evidence for electrons as the charge identity in charge transfer, the Q_{SC} data from the initially-charged Ti-SiO_2 TENG tests at temperatures above 443 K were set against the simulated exponential decay model identified previously for contact-separation TENGs.[97] Unlike the fairly good fit of 443 K (**Figure 25a**), the residual charges at 473 K (**Figure 25b**) and 533 K (**Figure 25d**) follow a less rapid fast-slow decay than that simulated, with a slower initial decline and a less severe transition into the slower decay portion. For 503 K (**Figure 25c**) and 563 K (**Figure 25e**), the initial decline is faster and the transition is more immediate into the slow decay period compared to the simulated curve. As these discrepancies were also observed in the previous study, perhaps increasing volume of tests

being averaged may match the data points to the exponential decay model more closely. Moreover, the plot of ln ($J/A_0/T$) against 1/T in **Figure 25f** fits their linear relationship quite well, showing a strong correlation of surface charge data with the thermionic emission equation.[97] The adequate fit of the sliding mode TENG data to simulated thermionic emission curves serves to provide further evidence of electron-dominated charge transfer in contact electrification.

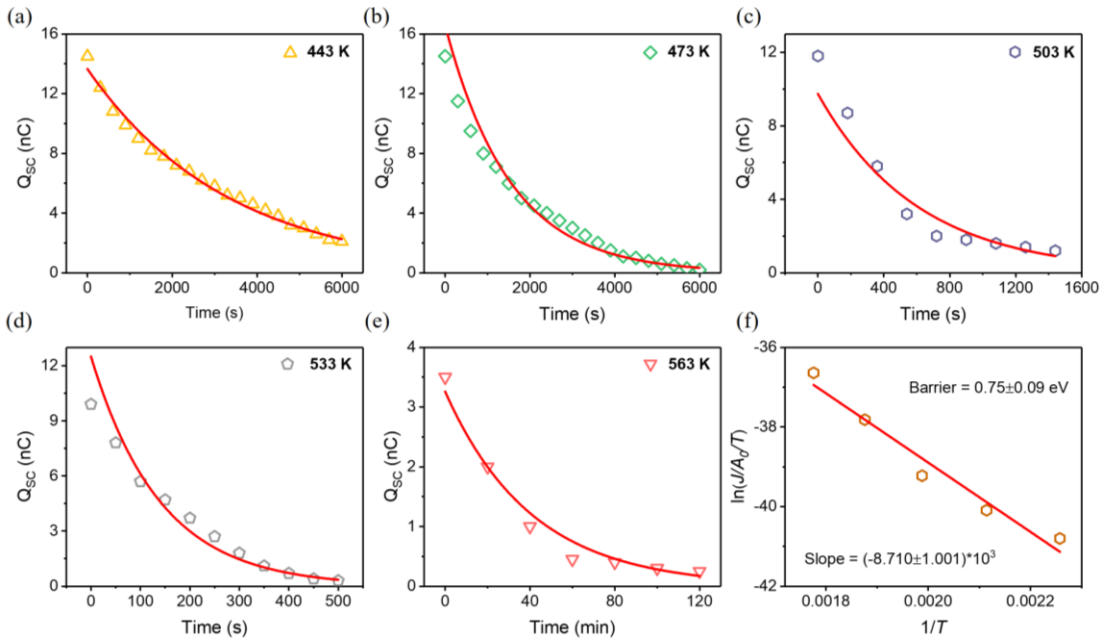

Figure 25. The measured (data points) and simulated curve based on electron thermionic emission model (solid) Q_{SC} as a function of the time at various temperatures. (a) 443 K, (b) 473 K, (c) 503 K, (d) 533 K. (e) 563 K. (f) Plots of ln ($J/A_0/T$) against 1/T.

When comparing our sliding mode data to previous contact-separation mode findings,[97] we can associate the increased time scale required for near-complete emission of surface electrons as well as the ability to retain and generate charges at higher temperatures due to the protective nature of the sliding mode TENG against discharge. As this operational mode allows for longer periods of overlapping triboelectric surfaces, the

effects of thermionic emission are dampened up until a certain temperature. Also, although the Q_{SC} rapidly decayed at higher test temperatures for the contact-separation mode Ti-SiO_2 TENGs, the sliding mode TENG was capable of generating even a small amount of transferred charge (0.05 nC) before decay took over at the highest tested temperature (563 K). In addition to Q_{SC}, surface charge density is also a satisfactory variable in investigating temperature effects on TENGs, and a recent study using and tapping mode AFM has found that triboelectric charge decay follows the thermionic emission model at nanoscale.[110] It would be of great interest to continue this line of research by using contact scanning mode AFM to mirror a sliding mode TENG.

3.2.2.4 Modified electron cloud model for sliding mode CE at high temperatures

Based on the mechanism of CE from the newfound data on high temperature sliding mode TENGs, a modified electron cloud potential well model is proposed for CE resulting from the sliding operational mode at elevated temperatures (**Figure 26**). This model may be applied to general triboelectric pair materials under these conditions in sliding contact, including metal-dielectric and dielectric-dielectric pairs. Since electrons in a general dielectrics do not have individual energy levels like in metals and semiconductors,[111, 112] the electron clouds and potential well model are presented as universal characteristics that all materials possess. Even in the presence of factors such as surface impurities and chemical/atomic structure of materials that complicate dielectric CE studies, this model should apply, although these additional factors will also have an impact, especially certain material characteristics at high temperatures. This model also offers an explanation for the prolonged charge retention and improved charge generation efficiency of sliding mode TENGs at high temperatures.

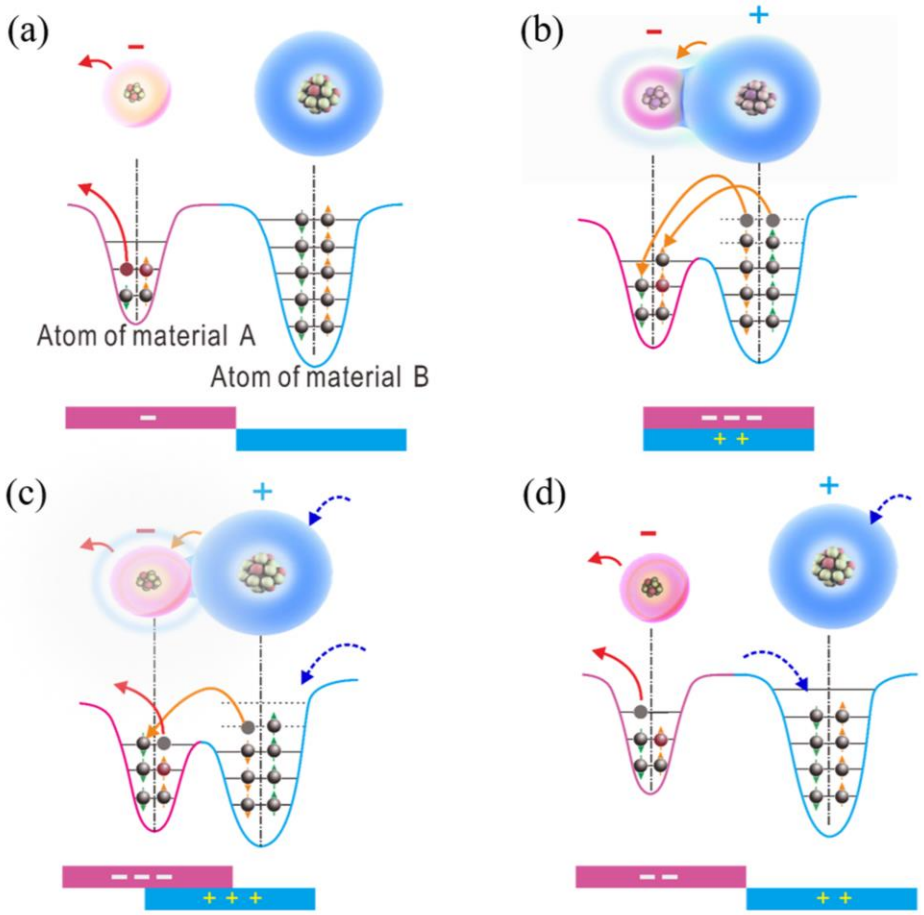

Figure 26. An electron cloud potential-well model proposed for explaining CE and charge transfer and release between two materials in the sliding-mode TENG. (a) Initial state. (b) Contact state. (c) Semi-separated state. (d) Separated state.

First off, the model shows two materials completely displaced from each other and their electron clouds filled with electrons that are localized to specific atomic or molecular orbitals (**Figure 26a**). In this state, material A is negatively charged from the initially-induced charges that were implemented in the first set of tests, and no electron transfer is occurring since it has not contacted material B yet. The difference in charge between the two materials is not as apparent without the pre-charging unless the materials are far apart on the triboelectric series. At high temperatures, the negatively pre-charged material A

exhibits thermionic emission of surface charges at this state of noncontact, represented by the red directional arrows. Material B is not indicated to have any significant thermionic emission since its electrons are at an equilibrium state, and it would take a much more extreme temperature to induce emission of electrons from material B. When the two materials are in contact when sliding against one another (**Figure 26b**), the electrons may be transferred from material B to material A due to CE and the development of equal and opposite charges on both surfaces when the materials are fully contacted. In this state, electron thermionic emission from the surface of SiO_2 is theoretically not present since the two surfaces are in such close contact. The electron clouds in Figure 5b demonstrate the overlap of clouds that occurs when two surfaces are closer than the interatomic distance at equilibrium, where long range attractive forces are equal to short range repulsive forces so charge transfer may occur.[12] These overlap areas or contact points occur from the presence of an externally applied force, and they occur on a very small fraction of the area between two surfaces in contact. However, they still play an instrumental role in facilitating CE, as has been validated by previous AFM studies.[12, 110, 113] The transfer of electrons, represented by the orange arrows, corresponds with the respective charge of each material surface in this state.

When the two materials begin to be displaced from the fully contacting state as they slide against each other along a single plane (**Figure 26c**), both the thermionic emission from the exposed areas of the negative material A and charge transfer from the areas in contact are affecting the measured total charges in sliding mode TENG. The emission of electrons from material A is represented by the red arrowheads, charge transfer by the orange arrowheads, and the flow of electrons through the circuit to balance the positive

material B by the blue arrowheads. When the two materials are completely displaced once more (**Figure 26d**), the residual charges on the surface of the negative material A dissipate more rapidly due to thermionic emission and the lack of shielding by material B. As the displaced area increases to be greater than the contact area, thermionic emission overtakes the charge generation effects of the sliding mode TENG. The emitted electrons are represented by the red arrowheads and the electrons traveling through the circuit due to the potential imbalance between the materials is demonstrated by the blue arrowheads. The behavior of nearly all metal-dielectric and dielectric-dielectric pairs in sliding mode operation at high temperature may be modeled using this electron cloud potential well model based on the rate of electron thermionic emission, the charge transfer rate of CE, the changing rate of the contacted area of between the two materials. Once the contacted area is dominant, the CE between the two materials is the major contributor. While the contact area is smaller than the displaced area, the thermionic emission of the exposed surfaces is the major contributor.

3.2.3 Conclusion

In summary, we compared the trends of thermionic emission of electrons between a sliding mode and previously tested contact-separation mode Ti-SiO_2 TENGs at elevated temperatures. The sliding mode TENG exhibited a sharper initial decline in charges below 503 K when pre-charged with PU to ~28 nC compared to the pre-charged contact-separation mode TENG. However, in an initially uncharged state, the sliding mode TENG was able to overcome the influence of thermionic emission even at the highest tested temperature to increase transferred charges for a period before succumbing to exponential decay, which was not observed in the contact-separation TENG tests. This and the

observation that the time scale for charge dissipation is much longer in sliding mode TENGs, both pre-charged and uncharged, are perhaps due to the prolonged shielding of discharge from the material surfaces in a continuous sliding motion as compared to an intermittent contact-separation motion. Lastly, the combined phenomena of CE charge transfer, and thermionic emission and the change in surface contacting areas are incorporated into a model of sliding mode CE between metal-dielectric and dielectric-dielectric pairs at high temperatures.

In general, high temperature operation of TENGs is not widely studied due to the degradation of many materials in such conditions under constant changing contact, as well as the low power output of materials at that state. Understanding the fundamentals behind charge behavior and optimized design are both important in furthering this front. Clearly, as CE may occur in a variety of different operational modes and is highly variable, controlled experiments with TENGs that have tailored designs and flexible material choices are valuable in studying the mechanisms of CE and developing its universal model. A rolling mode TENG study at high temperatures would be useful in analyzing the differences in charge generation and retention between the sliding and rolling modes, which have already had many comparative studies in terms of tribology. As sliding TENGs have been determined to be the best mode for both efficient high temperature operation and maximal power density, more investigations on other existing modes are necessary to form a solid knowledge foundation for the commercialization of TENGs.

3.2.4 Experimental Section

SiO_2 sheets (99%) of 0.3175 cm thickness were purchased from Technical Glass Products. Their thermal conductivity was 1.4 W mK^{-1} (293 K) and their dielectric constant

was 3.75 (299 K, 1 MHz). Ti foil (99.7%) with a thickness of 0.0032 cm was purchased from Sigma-Aldrich Co., LLC. Polyurethane (PU) foam was purchased from McMaster-Carr. Polytetrafluoroethylene film and Kapton film were purchased from American Durafilm.

3.2.4.1 Fabrication of the High Temperature Ti-SiO_2 TENG

The Ti foil and SiO_2 were used as triboelectric pair materials. An Au coating on the back of the SiO_2 with a thickness of 300 nm was deposited as an electrode by using a Denton Explorer E-beam Evaporator. The deposition rate of Au coating was 0.2 nm s^{-1}. After Au deposition, the SiO_2 was annealed at 673 K for 4 hours in air. The Au-coated SiO2 was clamped to an insulating and high-temperature-resistant ceramic plate attached to the steel bar connecting to the motor. The Ti foil was clamped against a second ceramic plate attached to a stationary heat-resistant steel platform. Ni wires were clipped behind the SiO_2 sheet positioned in contact with the Au electrodes and behind the Ti foil acting as its own electrode.

3.2.4.2 Characterization of the Ti-SiO_2 TENG Performance at Varying Temperature

A computer programmed linear motor was secured on top of a heating cabinet (Barnstead/Thermolyne 6000 furnace), which provides a desired temperature with an accuracy of ±5 K. The heating rate of the cabinet was about 7.5 K min^{-1}. In order to protect the motor from high temperatures, a long steel rod was implemented through the open hole in the heating cabinet to separate the active surfaces from the linear motor. A cooling fan was positioned adjacent to the setup to keep it from overheating. The environmental relative humidity was less than 30%, as measured by a Shaw Superdew 3 hygrometer.

During TENG performance measurement, the linear motor was effective in accurately controlling the position and speed of mechanical stimulation, and the heating cabinet maintained the desired temperature. The effective area of the Ti-SiO_2 TENG was 10 cm^2. The short-circuit transfer charge Q_{SC}, open-circuit voltage V_{OC}, and short-circuit current I_{SC} of the TENGs were measured by a Keithley 6514 electrometer and collected by LabView software. Pre-charged tests were performed after charging ~28 nC to the surface of SiO_2 using PU foam, and uncharged tests were performed after discharging the surface to nearly 0 nC by washing the triboelectric surfaces with ethanol and 2-propanol three times each and drying with Ar gas after each wash.

3.3 Developing an Efficient Triboelectric Nanogenerator for High Temperature Operation by Quenching Thermionic Emission of Electrons

3.3.1 Introduction

It is believed that CE occurs in most material systems around room temperature and nearly all conventional TENGs operate in this temperature range. However, the intriguing question stands: can CE pertain at high temperatures? Present studies of the temperature effect on CE or the TENG are still rare, and there are limited reports that address this question.[14, 27] Wen *et. al* studied the influence of temperature on the TENG and confirmed its successful operation at the high temperature of 500 K, despite a significant decrease in voltage.[71] Lu *et. al* reported that the decrease of the TENG output at high temperatures might be due to the thermal change of the chemical groups and the generation of structural defects on the tribo-material surface.[60] However, due to the limitation that TENGs are normally made of conventional polymers,[3, 9, 114] until now the potential occurrence and working mechanism of CE at higher than 500 K have not been elucidated. Our recent study developed a polymer-free TENG that withstood and operated at the temperatures as high as 673 K, providing the possibility to reveal the CE mechanism under high temperatures and develop a unique high-temperature resistant TENG.[38]

In this section, Ti/SiO_2 TENGs of different working modes were compared, and finally the rotating free-standing mode TENG was adopted for the study. Through optimizing the device structure, this rotating TENG with double supports produced the greatest output at 523 K. It was revealed that the dominant deterring factor of CE at high temperatures was electron thermionic emission. By further alternating materials and

applying pre-annealing, thermionic emission was prevented and the working temperature of the rotating TENG was risen up to 673 K. The surface states model and the electron cloud-potential well model were then proposed, respectively. These models accounted for the CE mechanism with temperature effects involving metals, dielectrics and polymers, and could be extended to all types of materials. This chapter section interpolates material from a paper co-authored by the thesis author with Professor Cheng Xu.[40]

3.3.2 Results and Discussion

To realize high temperature resistance, a SiO_2 plate was utilized as the tribo-material to replace the traditional polymer film and Ti foil rather than Cu foil or Al foil was used as the counter-electrode. **Figure 27** shows the prepared contact-separation mode TENG (C-TENG).The V_{OC} of the C-TENG is only around 1.3 V, similar to the rather small I_{SC} and Q_{SC}.

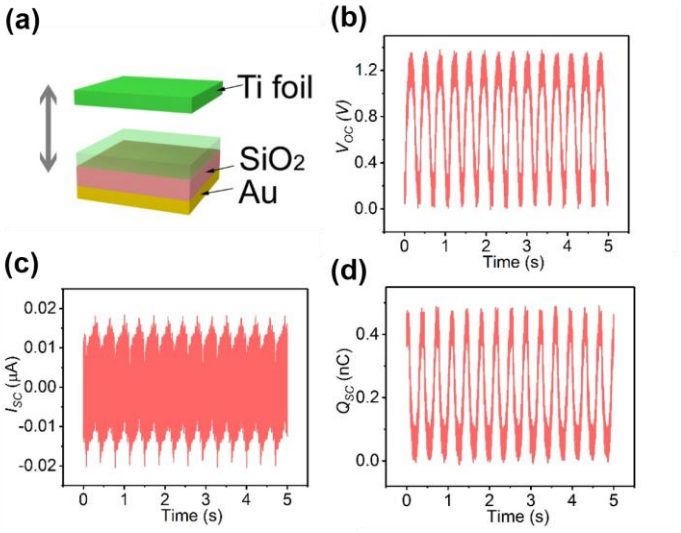

Figure 27. Performance of the C-TENG at room temperature. (a) Schematic illustration of the C-TENG. (b)-(d) V_{OC}, I_{SC} and Q_{SC} of the C-TENG at room temperature.

The working principle of the C-TENG is shown in **Figure 28**. The same size SiO_2 plate and Ti foil from the C-TENG are adopted in the sliding mode TENG (S-TENG) with an equal effective working area.

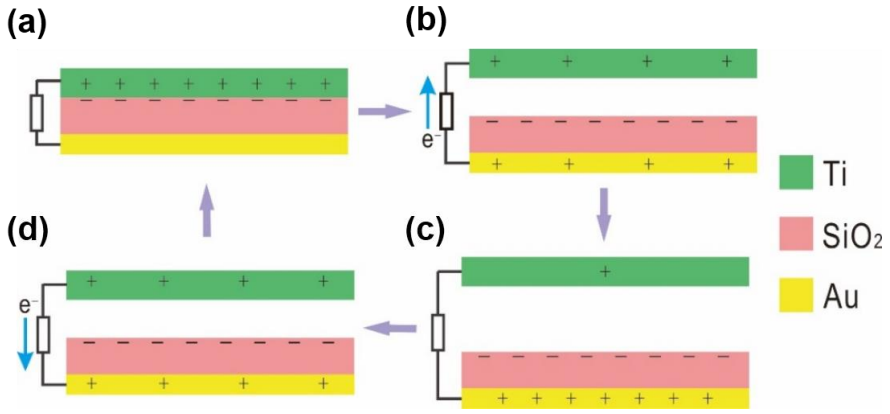

Figure 28. Working principle of the C-TENG. When Ti and SiO_2 come into contact, opposite triboelectric charges will be generated on the two surfaces with the same density: positive charges on the Ti and negative charges on SiO_2 (a). Upon release, the two oppositely charged surfaces start to separate from each other, inducing a potential difference between the Ti and Au electrode. This potential difference will drive electron flow from the Au electrode to Ti (b). When the separation between the two surfaces reaches a maximum, almost all the positive triboelectric charges on the Ti will be neutralized, so that the positive charges on the Au electrode equal the transferred charges on the Ti (c). Subsequently, when the Ti and SiO_2 are pressed to approach each other again, the reversed potential difference between the two electrodes will build, which leads to the back flow of all the transferred electrons from the Ti to the Au electrode (d).

The prepared S-TENG and its working principle are shown in **Figure 29** and **Figure 30**, respectively. The S-TENG generates over 15 V of V_{OC} with about 0.1 μA of I_{SC} and 6 nC of Q_{SC}. The fact that the output of S-TENG is much higher than that of C-TENG is attributed to the surface stiffness and roughness of SiO_2 plate. It makes the contact-separation mode difficult to realize perfect contact but creates more opportunities for the sliding mode to contact as much as possible between the SiO_2 plate and Ti foil. This increase of contact area leads to the S-TENG's higher output of V_{OC}, I_{SC} and Q_{SC}.

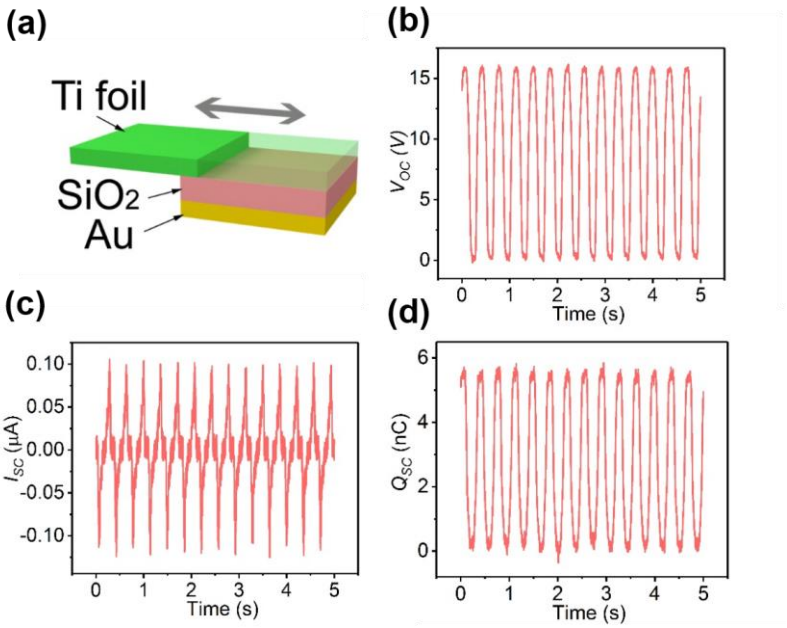

Figure 29. Performance of the S-TENG at room temperature. (a) Schematic illustration of the S-TENG. (b)-(d) V_{OC}, I_{SC} and Q_{SC} of the S-TENG at room temperature.

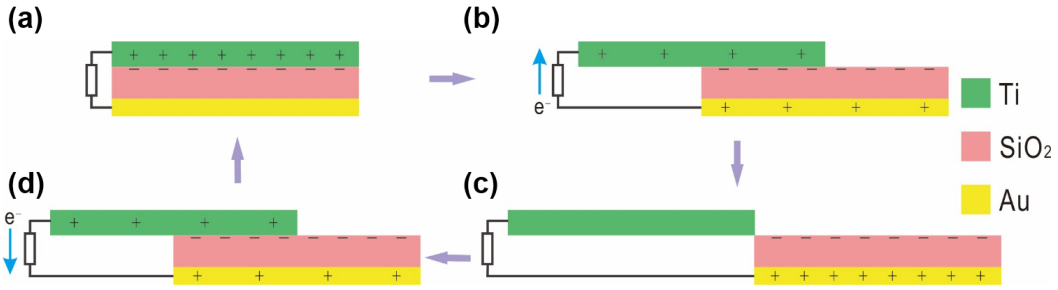

Figure 30. Working principle of the S-TENG. When Ti and SiO_2 get into contact, positive charges on the Ti and negative charges on SiO_2 will be generated (a). Once displacement is established, the uncompensated negative triboelectric charges on SiO_2 will repulsively drive electrons on the Au electrode to Ti, neutralizing the positive triboelectric charges and leaving behind positive induced charges (b). The flow of induced electrons lasts until the displacement reaches the maximum. At the fully displaced position, the positive triboelectric charges are completely balanced out by induced electrons (c), indicating no more current flow. As the displacement is diminished by the reciprocating force, the induced electrons flow back to the Au electrode (d).

Based on the aforementioned results, a rotating free-standing mode TENG (R-TENG) was prepared after making further improvements (**Figure 31a**). The R-TENG utilizes a SiO_2 tube whose thickness is the same as that of the SiO_2 plate. The inset in **Figure 31a** is an optical photograph of the R-TENG. **Figure 31b** and **33d** are the optical photographs of the SiO_2 tube and Ti foil, respectively. **Figure 31c** and **32e** are scanning electron microscopy (SEM) images of the surfaces of the SiO_2 tube and Ti foil, respectively. The surface of SiO_2 is smooth while that of the Ti foil has a rough raised texture. These two materials rub against each other through rotation to yield triboelectricity output.

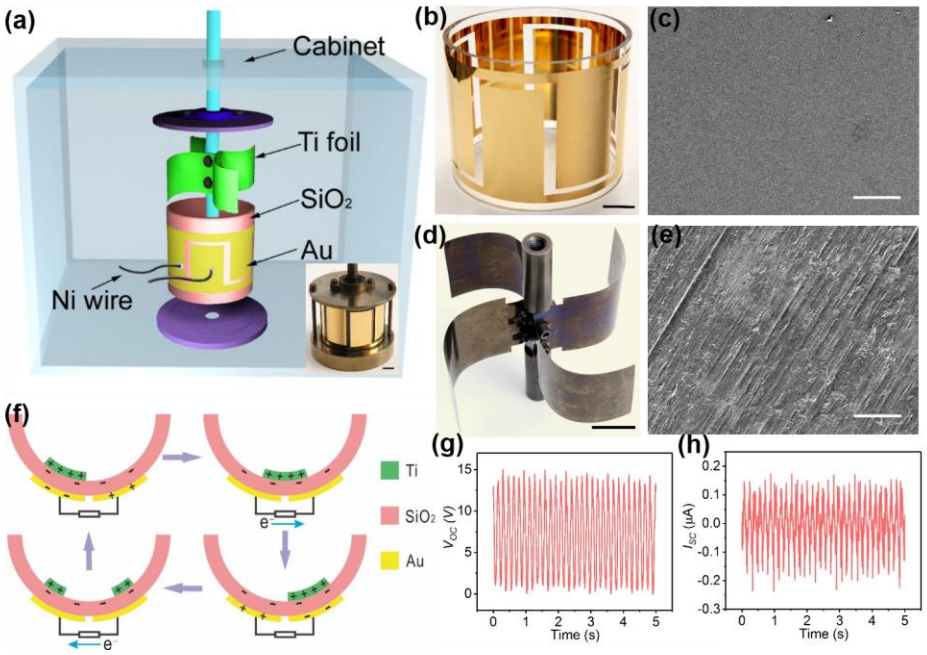

Figure 31. Performance of the R-TENG at room temperature. (a) Schematic illustration the R-TENG in the high-temperature measurement platform. Inset is an optical photograph of the R-TENG. (b), (c) Optical photograph and SEM image of SiO_2 tube. (d), (e) Optical photograph and SEM image of Ti foil. The black scale bar and white scale bar are 2 cm and 100 μm, respectively. (f) The working principle of the R-TENG. (g), (h) V_{OC} and I_{SC} of the R-TENG at room temperature.

The working principle of the R-TENG can be described by the coupling of CE and electrostatic induction. Here, a pair of rotation units including Ti foil and SiO_2 with a back Au electrode is selected to illustrate the process of electricity generation (**Figure 31f**). Upon contact between SiO_2 and Ti foil, electrons are transferred from Ti foil onto the surface of SiO_2. Since the two rotation surfaces are completely aligned, triboelectric charges with opposite polarities are fully balanced out, resulting in no electron flow in the external circuit. Once a relative rotation occurs, triboelectric charges on the mismatched areas cannot be compensated. The negative charges on the SiO_2 surface will drive free electrons from one back electrode to the other through the external circuit. The flow of the induced electrons lasts until Ti foil completely matches with the next SiO_2 division with a back Au electrode. As the relative rotation continues, Ti foil starts to leave the second SiO_2 division with a back Au electrode. Thus, the induced electrons will flow back in the opposite direction until the fully aligned position is restored. As shown in **Figure 31g-h**, the V_{OC} and I_{SC} generated from the R-TENG at room temperature reach 15 V and 0.2 μA, respectively.

Figure 32a is the schematic illustration of the Ti foil and SiO_2 tube layout of the R-TENG. **Figure 32b-d** are the V_{OC}, I_{SC} and Q_{SC} of the R-TENG at different rotation rates and temperatures.

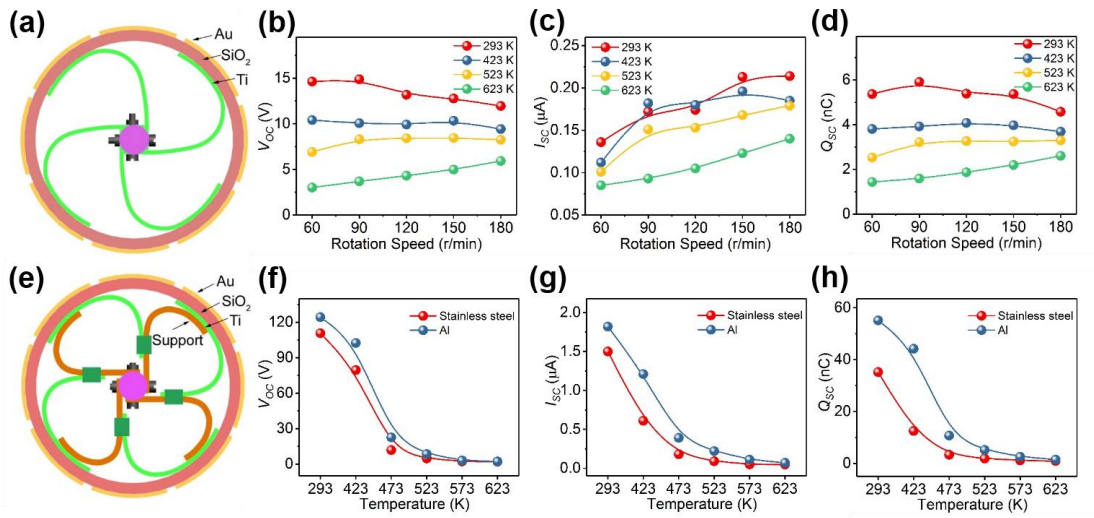

Figure 32. Effect of rotation speed and support material on the R-TENG at different temperatures. (a) Schematic illustration of Ti foil and SiO_2 tube of the R-TENG. (b)-(d) V_{OC}, I_{SC} and Q_{SC} at different rotation rates and temperatures. (e) Schematic illustration of the R-TENG with a support. (f)-(h) V_{OC}, I_{SC} and Q_{SC} of the R-TENG with different supports at different temperatures.

When the speed increases from 60 r/min to 180 r/min, V_{OC} at room temperature stays constant at first and then slightly declines while the current gradually increases. For the TENG operated at room temperature, according to our previous work, the amplitudes of V_{OC} and I_{SC} can be represented as:[8, 115]

$$V_{OC} = \frac{Q_{SC}}{C} = \frac{\sigma S}{C} \tag{8}$$

$$I_{SC} = \frac{n}{\pi}\frac{\sigma}{2} S\omega \tag{9}$$

where σ is the triboelectric charge density on the SiO_2 surface, S is the area of one electrode, C is the capacitance between the two electrodes, n is the number of segments on the rotator, and ω is the rotational angular velocity. Referring to Eqs. (8) and (9), by increasing the

rotation speed, the amplitude of V_{OC} and Q_{SC} will keep nearly constant; in the meanwhile, I_{SC} will increase proportionally. When the speed increases to 120 r/min, the slight decrease of V_{OC} and Q_{SC} may be due to the heating effect, which coincides with the results from increasing the working temperature as follows. With the temperature increase, **Figure 32b-d** also demonstrate some intriguing phenomena. One is that V_{OC}, I_{SC} and Q_{SC} all decline with the increase of the temperature. The other is, different from what happens at room temperature, V_{OC} and Q_{SC} gradually rise with the increase of the rotation rate. Both of the above phenomena can be attributed to the electron thermionic emission:[61, 62]

$$J = \lambda A_0 T^2 e^{\frac{W}{kT}} \left[e^{\frac{\Delta W}{kT}} - 1 \right] \tag{10}$$

where J is the thermionic emission current density, λ is the material-specific correction factor, A_0 is the Richardson constant of a free electron, T is the temperature, W is the height of the potential barrier, k is the Boltzmann constant, and ΔW is the potential barrier height variation due to the surface electric field. From Eq. (10), it shows that J increases with the increase of temperature, which leads to the decrease of σ on the SiO_2 surface and thus results in the decline of V_{OC}, I_{SC} and Q_{SC}. Meanwhile, the increase of the rotation rate inhibits the thermionic emission, resulting in the rise of V_{OC} and Q_{SC} to some extent. Here, to avoid the disadvantages of the heating effect, all the rotation rates of the R-TENGs are kept at 90 r/min afterwards.

Since the V_{OC} in **Figure 32b** is only around 15 V, a compound R-TENG with a support is further constructed to realize a V_{OC} improvement (**Figure 32e**). As shown in **Figure 32f-h**, V_{OC}, I_{SC} and Q_{SC} increase at room temperature when using either stainless

steel or Al as the support. For instance, the V_{OC} reaches 110 V with Al as the R-TENG support whereas a higher V_{OC} of over 120 V and nearly 2 μA of I_{SC} and 60 nC of Q_{SC} are obtained with stainless steel as the support. This is attributed to the fact that the support increases the friction between Ti foil and SiO_2 surface. Even though a higher output can be obtained by the R-TENG with a support at room temperature, V_{OC}, I_{SC} and Q_{SC} still decrease with the increase of temperature.

Figure 33a is the R-TENG constructed with double supports, which is expected to obtain more interaction force between the Ti foil and SiO_2 tube. Here, a simplified mechanic model is constructed in **Figure 33b** to make a theoretical static analysis of the R-TENG structure. The Ti foil of the R-TENG is regarded as a straight beam. It is fixed at the center and is bent by applying a force F_0 at the free end and then placed in the cylindrical shell with the initial deformed configuration. The deflection curve of the deformed configuration can be written as a function of $y(x)$. With the help of the Euler-Bernoulli nonlinear beam theory, the bending moment $M(x)$ of the beam at point x can be evaluated with the formula:[116]

$$M(x) = -E(T)I\rho(x) \tag{11}$$

Here, $\rho(x) = \frac{d^2y}{dx^2}\left[1+\left(\frac{dy}{dx}\right)^2\right]^{-3/2}$ is the curvature of the deflection of the beam at point x. $E(T)$ is the Young's modulus, which is constant along the beam, and is a function of temperature T. E decreases in approximate linearity with the increase of T. I is the cross-

sectional moment of inertia. For a rectangular cross-section beam with thickness h and width b, $I = \frac{1}{12} bh^3$. EI is the bending stiffness of the beam.

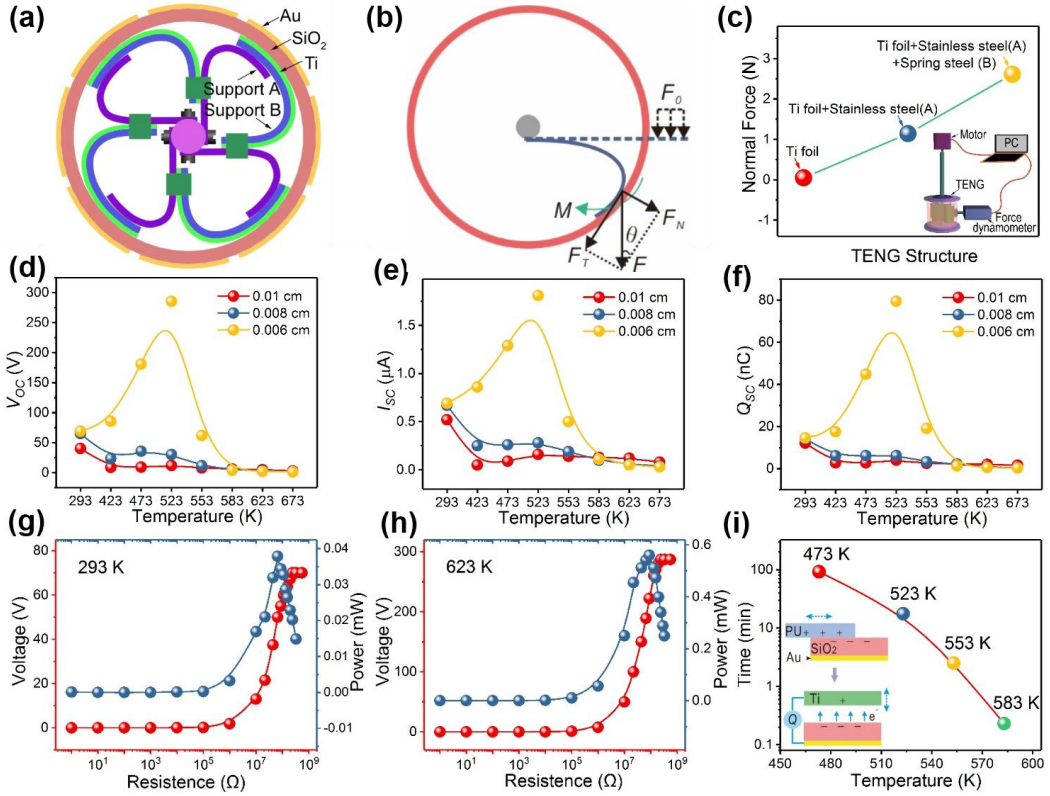

Figure 33. Performance of the R-TENG with double supports at different temperatures. (a) Schematic illustration of the R-TENG with double supports. (b) Simplified mechanical model of the R-TENG structure. (c) Set up of the force measurement platform and the experimental results of F_N. (d)-(f) V_{OC}, I_{SC} and Q_{SC} of the R-TENG with spring steel (support A) of different thickness under different temperatures. (g)-(h) Dependence of the output power of the R-TENG on resistive loads at 293 K and 623 K. (i) Procedure of the thermionic emission time measurement and the experimental results at different temperatures.

For a given initial deformation, the bending moment M linearly depends on the bending stiffness of EI. As a result of the equilibrium condition of the beam, the bending moment $M(A)$ equates $F_T R$ at the contact point A between Ti foil and SiO_2 tube. F_T is the

tangential force. R is the radius. The normal force F_N equates $F_T \tan\theta$. Thus, we can obtain the normal force:

$$F_N = -\frac{EI\rho(A)}{R}\tan\theta \tag{12}$$

Here, the value of $\frac{\rho(A)}{R}\tan\theta$ depends on the initial geometric configuration of the beam, which is denoted as G in our experiments. Hence, the normal force $F_N = -E(T)IG$ is proportional to the effective bending stiffness $EI = \frac{E(T)bh^3}{12}$ of the beam. For the R-TENG without supports in **Figure 32a**, the effective bending stiffness is $E_1 I_1 = \frac{bh^3}{12}E_{Ti}(T)$, where E_{Ti} is Young's modulus of Ti foil. Therefore, the normal force without support (F_{N1}) is:

$$F_{N1} = \frac{E_{Ti}(T)bh^3}{12}G \tag{13}$$

For the R-TENG with a support in **Figure 32e**, both Ti foil and the support can be regarded as cantilever beams which are pre-assembled together. For simplification, we assume that the two beams have the same cross-sections, and their Young's moduli are E_{Ti} and E_S, respectively. Therefore, the normal force with a support (F_{N2}) is:

$$F_{N2} = \frac{bh^3 G}{12}\left[E_{Ti}(T) + E_S(T)\right] \tag{14}$$

For the R-TENG with double supports in **Figure 33a**, the effective bending stiffness of the two-layered beam (Ti foil and support B) is $\frac{E_{Ti}(T)+E_B(T)}{3}bh^3$, where E_B is Young's modulus of the support B. The total normal force with double supports (F_{N3}) is:

$$F_{N3}=\frac{bh^3G}{12}\left[4E_{Ti}(T)+4E_B(T)+E_A(T)\right] \tag{15}$$

where E_A is Young's modulus of the support A. If the beams have the same initial geometric configurations, we have a relation of $F_{N1}<F_{N2}<F_{N3}$. Aside from the biggest force being able to be applied by the R-TENG with double supports, another advantage of this structure is having the most stable mechanical properties at high temperatures due to the increased effective bending stiffness.

For further quantitative study, a customized force measurement platform is set up to conduct a F_N test, as shown in the inset of **Figure 33c**. Prior to the test, trepanning was performed on the side wall of the SiO_2 tube and the probe of the force dynamometer was placed into the hole to contact the Ti foil. The test results show that the F_N of the R-TENGs without support, with a support, and with double supports are 0.2 nN, 1.2 nN and 2.8 nN, respectively. The increasing trend coincides with the conclusion drawn from theoretical analysis, demonstrating that the double support structure can improve the contact between Ti foil and SiO_2 tube. **Figure 33d-f** show the obtained V_{OC}, I_{SC} and Q_{SC} of the R-TENG after the variation in thickness of spring steel of support A in a double support structure (support B is the same as that in **Figure 32e**). **Figure 34** is F_N generated from different

thicknesses of spring steel, which shows that the increase of the thickness of spring steel leads to the linear rise of F_N.

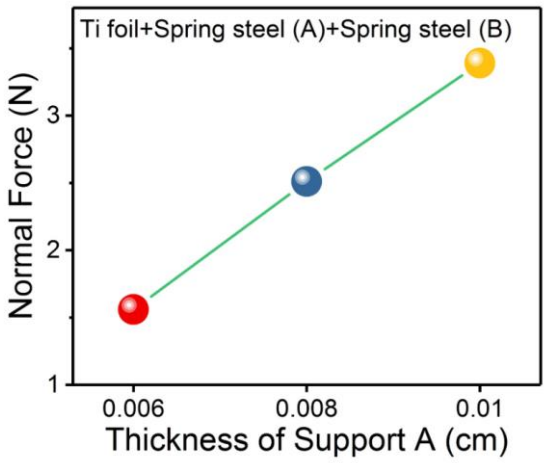

Figure 34. F_N varies with the thickness of support A (spring steel) of the R-TENG with two supports.

However, V_{OC}, I_{SC} and Q_{SC} in **Figure 33d-f** show that the phenomena differ from before. One phenomenon is that the increase of F_N decreases V_{OC}, I_{SC} and Q_{SC} at room temperature, demonstrating that over-imposed force leads to negative effects. Another intriguing phenomenon is that with temperature increase, V_{OC}, I_{SC} and Q_{SC} present a tendency to rise first and then descend, reaching their maximum values at around 523 K under all three steel thicknesses. Moreover, the V_{OC} of the R-TENG with spring steel thickness of 0.006 cm reaches almost 300 V at 523 K, more than three times its initial 70 V. The rise of temperature pushes the peak power up to nearly 0.6 mW at 523 K from the initial 0.04 nW at room temperature (**Figure 33g-h**). To further confirm whether this phenomenon occurred due to Ti foil or spring steel, we conducted different measurements

under the same conditions with Al foil to replace Ti foil and stainless steel to substitute spring steel respectively and found the same results for V_{OC} (**Figure 35**).

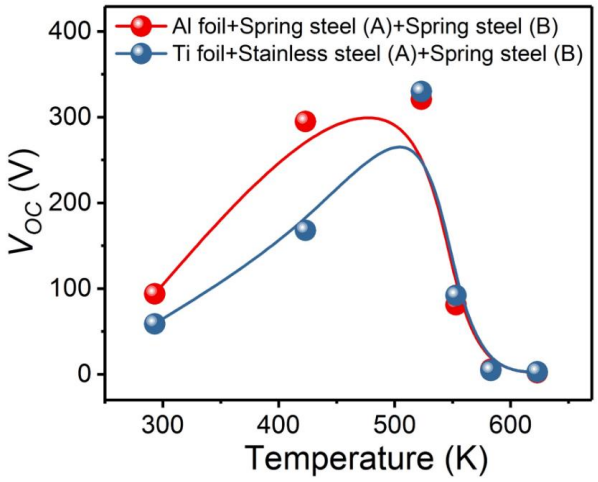

Figure 35. V_{OC} of the R-TENG at different temperatures. The red indicates the same structure as that in Figure 33a except that the Ti foil is replaced by Al foil. The blue indicates the same structure as that in Figure 33a except that support A is replaced by stainless steel.

This indicates that the phenomenon is not caused by any special material but is indeed related to the temperature. The reason behind this is the above proposed electron thermionic emission. To quantitatively explore the thermionic emission effect, we designed the thermionic emission time measurement shown in the inset of **Figure 33i**. First, a SiO_2 plate coated with an Au electrode was rubbed against polyurethane to be negatively charged with around 50 nC. Next, SiO_2 plate and Ti foil were assembled into the C-TENG in **Figure 27** to conduct charge tests until Q_{SC} decreased to 0.5 nC. The time used in this process was defined as the thermionic emission time. It should be noted that the measurement is simplified since the curved surface of the SiO_2 tube is replaced by the flat surface of the SiO_2 plate. **Figure 33i** shows that the time decays in an exponent-like from

463 K to 583 K. It is well known that usually one hundredth of a second to several seconds is needed for CE to accumulate charges until balance at room temperature.[76, 117] At higher temperatures, the charge accumulation process also occurs, which competes with the charge loss caused by the thermionic emission. At 523 K, the increase of temperature softens the surface of Ti foil and SiO_2 to some extent, enlarging the contact area, and then accumulates more charges under suitable force. However, the thermionic emission time at such a temperature is more than 10 min, which is insufficient to influence charge accumulation and balance processes, and therefore the R-TENG obtains the highest V_{OC}. When the temperature further increases to 553 K, the time decays to around 2 min and the thermionic emission begins to affect the charge accumulation process, leading to the decline of V_{OC}. When the temperature rises up to 583 K, the thermionic emission time, merely 0.2 min, is too short to realize charge accumulation. At that temperature, V_{OC} quickly declines to below 3 V, and I_{SC} and Q_{SC} dramatically decrease as well.

Although **Figure 33** demonstrates the detrimental effect of thermionic emission on CE, it also indicates that the charges are likely to be generated at higher temperatures (>583 K) once the thermionic emission is inhibited. Here, two forms of R-TENG improvements are adopted. One is to choose a Ni alloy and Ti alloy with more stable thermodynamic properties to replace spring steel as support A in **Figure 33a**, intended for better interaction force at high temperature. Despite a larger F_N (6.5 nN and 10.3 nN respectively) being obtained at room temperature, these two alloy-substituted R-TENGs still fail to improve V_{OC}, I_{SC} and Q_{SC} at more than 523 K (**Figure 36a-c**).

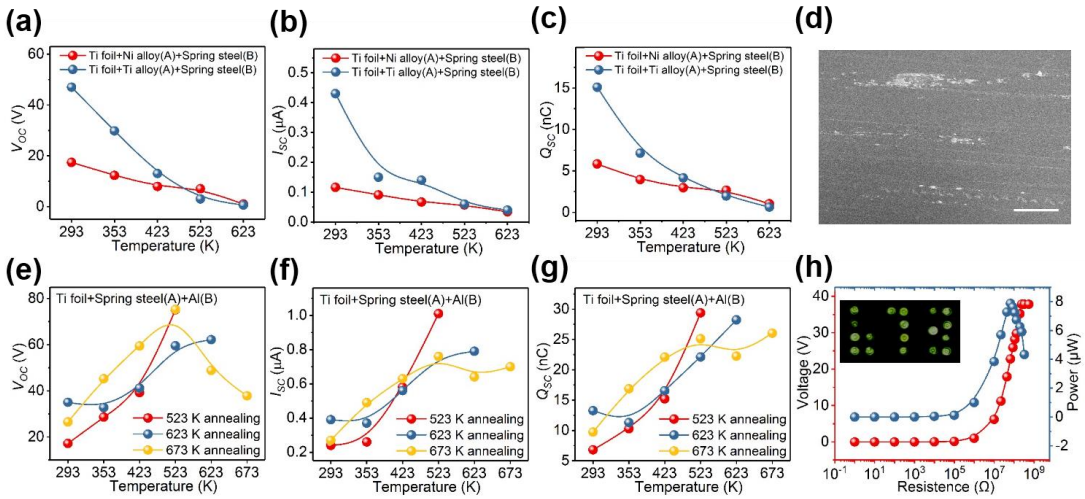

Figure 36. Performance of the double support R-TENGs with different materials and at different annealing temperatures. (a)-(c) V_{OC}, I_{SC} and Q_{SC} of the R-TENG with Ni alloy and Ti alloy as the support A. (d) SEM image of the SiO_2 surface after high temperature measurement. (e)-(g) V_{OC}, I_{SC} and Q_{SC} of the R-TENG with an Al sheet as support A after different temperature annealing. (h) Dependence of the output power of the R-TENG on resistive loads at 673 K. The inset shows that the LEDs can be lit by the R-TENG at 673 K.

One possible reason is that the larger exerted force causes the inner surface of the SiO_2 tube to be worn down. It is confirmed by SEM image that there are scratches after the high temperature measurement (**Figure 36d**). The enlarged images show some spalling and even holes on the SiO_2 surface (**Figure 37**).

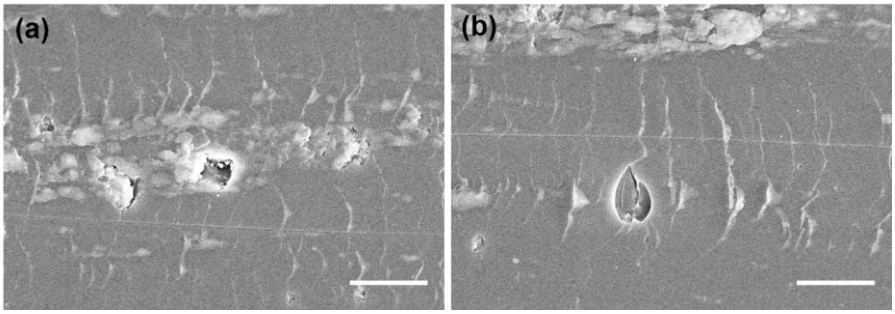

Figure 37. SEM images of SiO_2 surface after high temperature measurement. Scale bar indicates 10 μm.

Another attempt is to use an Al sheet with low heat resistance rather than spring steel as support A. First, we increased the interaction force between Al sheet and SiO_2 tube to a sufficiently large value (>15 nN) at room temperature. Then, pre-annealing at different temperatures was performed to the deformed Al sheet and tightly fit SiO_2 tube as close as possible under that temperature. **Figure 36e-g** show the obtained V_{OC}, I_{SC} and Q_{SC} of the R-TENG at different temperatures after pre-annealing. It is apparent to see that higher V_{OC}, I_{SC} and Q_{SC} can be obtained once the temperature increases to the annealing temperature, even though those at room temperature are not as high as expected, owing to the thermal expansion and contraction of the Al sheet. For example, after annealing at 623 K, in spite of the mere V_{OC} of less than 40 V at room temperature, over 60 V of V_{OC} can be obtained once the temperature rises up to 623 K. After annealing at 673 K, a V_{OC} of nearly 40 V can be obtained at that temperature. **Figure 36h** demonstrates that the maximum peak power of the R-TENG reaches 8 μW at 673 K. Under such high temperatures, the R-TENG still manages to light more than ten LEDs, which form the numbers of "673" (inset in **Figure 36h**).

3.3.2.1 Surface States Model: Metal-Dielectric Cases

According to the experimental results, we propose a CE mechanism between a metal and an insulator dielectric media at high temperatures by using the surface states model. In this model, the electrons in the metal conform to the Fermi-Dirac distribution function[118]. In the ideal condition, i.e. at absolute zero T_0 = 0 K, the electrons will fill up all available energy states below the Fermi level E_f. However, the reality is that the temperature is always above T_0, and thus some electrons are elevated to the level above the E_f, as shown in **Figure 38a** following the Fermi-Dirac function. When the metal is in

contact with the dielectric (**Figure 38b**), electrons located at high energy in the metal will transit to the surface states of the dielectric as indicated in process (1), i.e. triboelectrification. When the metal and the dielectric are separated (**Figure 38c**), the electrons entering into the dielectric surface can also escape because of the thermionic emission effect, i.e. thermionic emission of triboelectric charges, as indicated in process (2). Here, some charges still maintain on the dielectric surface due to its potential barrier, that is, CE occurs. In addition, the electron from the environment may transfer to the metal due to the positive charged surface, as indicated in process (3).

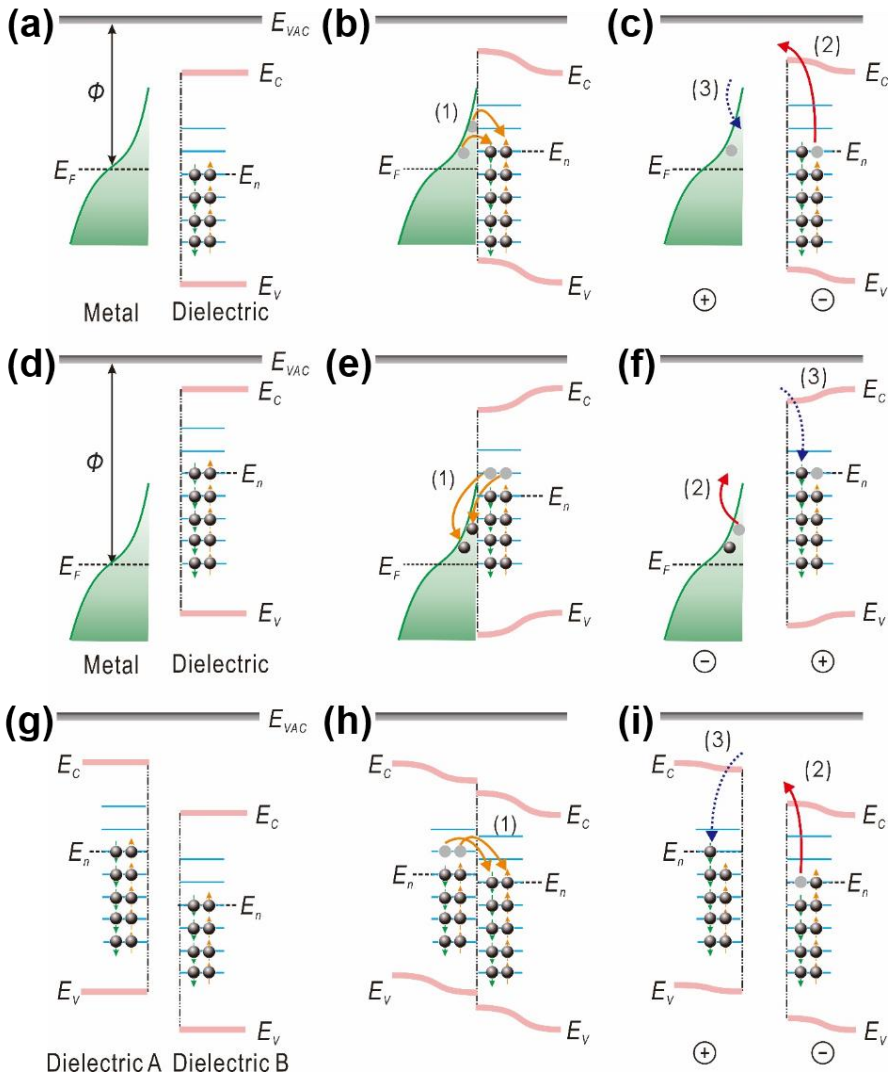

Figure 38. CE mechanism explained by surface states model at high temperatures. (a)-(c) Charge transfer before contact, in contact, and after contact between a metal and an insulator dielectric for a case that E_n is lower than E_F. Φ, metal work function; E_F, Fermi level; E_{VAC}, vacuum level; E_C, conduction band; E_n, neutral level of surface states, E_V, valence band. (d)-(f) Charge transfer before contact, in contact, and after contact between a metal and an insulator dielectric for a case that E_n is higher than E_F. (g)-(i) Charge transfer before contact, in contact, and after contact between two different insulator dielectrics for a case that E_n of the former is higher than that of the later.

Hence, the CE at high temperatures is mainly a competitive outcome of the triboelectrification and thermionic emission of electrons. The higher the temperature is, the more possible the thermionic emission of electrons occur, and the less the net charges remain at the dielectric surface. In any case, the dielectric is negatively charged and the metal is positively charged. It should be noted that, although the electron transfers from the metal to the dielectric in this study, alternatively, it can also transfer from the dielectric to the metal if the E_n is higher than the E_f, as shown in **Figure 38d-e**. Under this condition, the thermionic emission of triboelectric charges will occur at the metal surface rather than the dielectric surface (process (2) in **Figure 38f**). In this case, the dielectric is positively charged and the metal is negatively charged. Therefore, there is a possibility of a temperature-induced reversal in the sign of the triboelectric charges on the metal/dielectric surface depending on the interface electronic structure of the metal-dielectric system.

3.3.2.2 Surface States Model: Dielectric-Dielectric Cases

To extend the surface states model, it can be used to account for CE mechanism of two different types of insulator dielectrics at high temperatures. Assume that E_n of dielectric A is higher than that of dielectric B (**Figure 38g**). When the two dielectrics contact with each other (**Figure 38h**), the electron located at high energy states in dielectric A will transit to the low energy states of the surface states of dielectric B, as indicated in

process (1). It is similar to the metal-dielectric case in **Figure 38b**. After the two dielectrics are separated (**Figure 38i**), the transferred electrons in dielectric B escape from the surface because of thermionic emission, as shown in process (2). Meanwhile, since it currently has more positive charges, dielectric A is likely to capture electrons from the environment as indicated in process (3). Ultimately, dielectric A is positively charged, while dielectric B is negatively charged. It is anticipated that the sign of the transferred charges in this case would not reverse with the increase of temperature.

3.3.2.3 Electron Cloud Model: General Solid Materials

The previous proposed electron cloud-potential well model[38] is used to account for the CE mechanism of any two solid materials at high temperatures, such as polymers, cellular, amorphous or any materials that do not have a well-defined crystal structure. As for these systems, neither band structure nor surface states can be adopted to represent the electronic structure of the materials, but we can start from the atomic or molecular orbits model, which is always the case for a general material. **Figure 39a** shows that, prior to the atomic contact of the two materials, their respective electron clouds remain separated without overlap. The potential well binds the electrons and stops them from freely escaping, which is the case for non-conducting materials. When the two atoms belonging to two materials, respectively, get close to and contact with each other, the electron clouds overlap between the two atoms to form ionic or covalent bond. The initial single potential wells become an asymmetric double-well potential and then electrons can transit from one atom to the other, i.e. triboelectrification, as indicated in process (1) in **Figure 39b**.

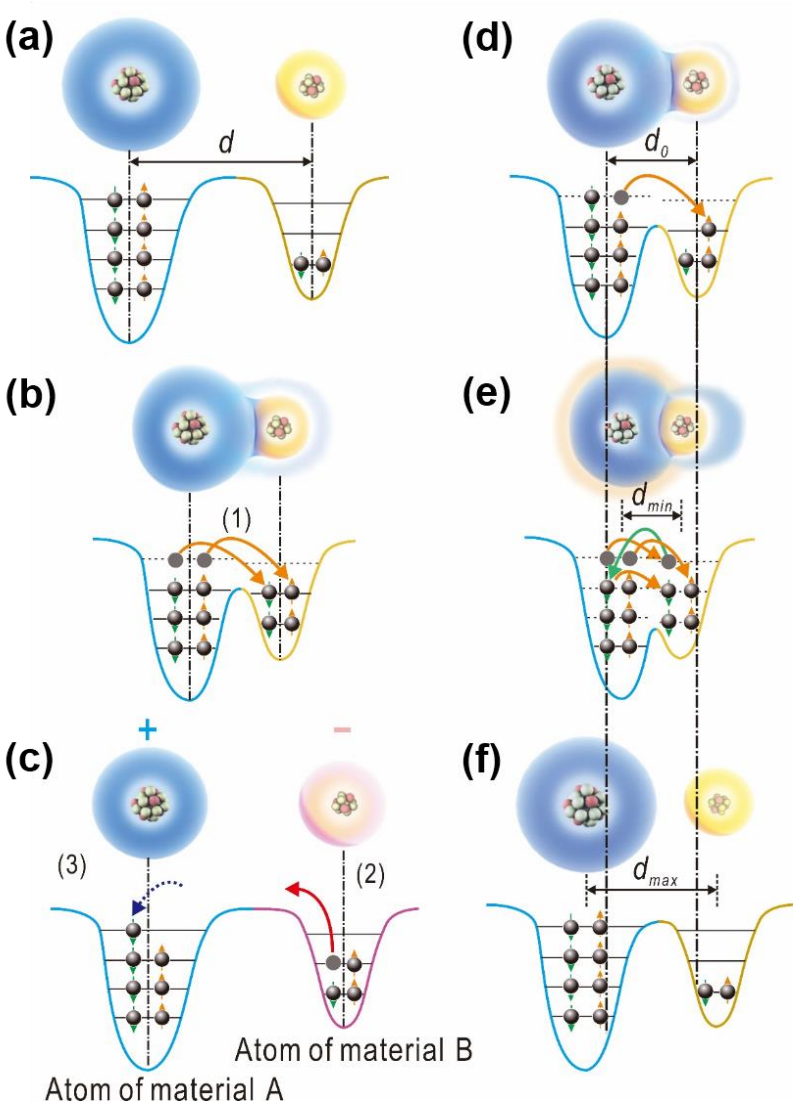

Figure 39. CE mechanism explained by electron cloud-potential well model at high temperatures. (a)-(c) Charge transfer before contact, in contact, and after contact between two atoms of any two solid materials that cannot be simply described by a band structure model. *d* is the distance between electron clouds of the two atoms belonging to materials A and B, respectively. (d)-(f) Effect of atomic thermal vibration on charge transfer at the distance of d_0, d_{min} and d_{max} between the two atoms when they are in contact.

The role played by mechanical contacting of the two materials is to shorten the distance between the atoms to cause overlap of their electron clouds, at least at the area at which the atomic-scale contact occurs. This also makes sense that more charges are transferred if one material scrubs the other harder/tighter. After being separated (**Figure**

39c), the transferred electrons remain, but the thermionic emission of triboelectric charges occurs, resulting the partial release of the electrons from the atom belonging to material B (process (2) in **Figure 39c**); at the same time, replenishment of electrons from the environment may be taken by the atom of material A (process (3) in **Figure 39c**), making it less negatively charged.

In practice, the thermionic emitted electrons in processes (2) can be accelerated significantly by the discharging field of the triboelectrification while traveling in vacuum, which can be as high as a few keV in energy. Thus, X-ray emissions can be generated by using the electron exciting a metal target.[119-121] Alternatively, visible light, microwave and even THz waves can be emitted by the electrons during transition from material A to material B owing to the energy release. Light emission is also possible by the thermionic emitted electrons as accelerated by the discharging triboelectric field. Based on the conventionally observed surface tribo-charge density in air, ~250 $uC.m^{-2}$,[122] the charge coverage on a surface is roughly one electron every 10,000 atoms. In other words, for a spherical particle of 20 nm in diameter, its surface has about 3 triboelectric induced electrons.

3.3.2.4 Effect of Atomic Thermal Vibration on CE

In the models above, we mainly focused on the effect of temperature on the electron transfer during the process of CE. However, besides its influence on the electron distribution and thermionic emission, temperature also affects the positions of the atoms in the material. For a crystalline material, the atomic vibration is well described by phonon models with well established dispersion relationship. One of the models is the Einstein

model in which all of the atoms are vibrating randomly. In this case, we tend to illustrate the effect of atomic thermal vibration on CE when two different atoms do mutual contact by using the electron cloud-potential well model. **Figure 39d** shows the situation in which the two atoms are in contact with each other. It is, in reality, a non-equilibrium dynamic process due to the atomic thermal vibration around the equilibrium position at high temperature. Suppose the distance between the two atomic nuclei is *d*, then:

$$d = d_0 + \Delta(T, t) \tag{16}$$

where d_0 is the equilibrium position of the atoms. $\Delta(T, t)$ is the vector difference of the two atoms deviating from the equilibrium position, the function of temperature T and time t. When the two atoms instantaneously separate by d_0, the electron clouds overlap, the electron with high energy in the atom of material A can transit to the atom of material B, because the transition speed of electrons is much faster than the speed at which the atom vibrates. When the distance between the two atoms instantaneously decreases to the minimum d_{min} (**Figure 39e**), the electron clouds overlap the most and the height of the connection place of the corresponding potential wells further decreases. For this case, the electron locates at higher energy in the atom of material A can transit to the atom of material B. Similarly, the electron at higher energy in the atom of material B can also transit to the low energy state in the atom of material A. When the two atoms are instantaneously separated by the maximum distance d_{max} (**Figure 39f**), it may well be that the electron clouds of the two atoms remain minimum. In this case, electron transfer does not occur. For all the abovementioned, atomic thermal vibration can influence CE and it is more significant with the temperature increases.

3.3.3 Conclusion

In conclusion, we designed and successfully constructed a R-TENG that worked up to 673 K. We found that the electron thermionic emission played an increasingly more important role for CE with the temperature increase. The surface states model and the electron cloud-potential well model were proposed, revealing that CE at high temperatures was mainly a competitive outcome of triboelectrification and thermionic emission of triboelectric charges. In addition, atomic thermal vibration also influenced CE and it was more significant with the temperature increases. These models contributed to the general CE mechanism with temperature effects for all types of materials. Our study might extend the temperature range of TENG applications to cases such as under diverse extreme environments on planets, in outer space, and even on exoplanets in the solar system.

3.3.4 Experimental Section

3.3.4.1 Fabrication of High Temperature Resistant TENGs

Ti foil (99.7%) with a thickness of 0.003 cm was purchased from Sigma-Aldrich Co. LLC. A SiO_2 (99%) plate with a thickness of 0.32 cm and a SiO_2 (99%) tube with a diameter of 10 cm and thickness of 0.32 cm were purchased from Technical Glass Products. Spring steel sheets with thicknesses of 0.006 cm, 0.008 cm and 0.01 cm were purchased from Lyon Industries. Al foil with a thickness of 0.002 cm, stainless steel sheet with a thickness of 0.01 cm, Al sheet with a thickness of 0.02 cm, Ni alloy sheet with a thickness of 0.03 cm, Ti alloy sheet with a thickness of 0.02 cm, and polyurethane foam were purchased from McMaster-Carr. Ti foil and SiO_2 were used as the electrification materials for all of the TENGs. An Au coating with a thickness of 300 nm was deposited

on the back of the SiO_2 plate or the outside of the SiO_2 tube as the electrode by using a Denton Explorer E-beam Evaporator. The deposition rate of Au coating was 0.2 nm/s. After Au deposition, the SiO_2 plate and tube were annealed at 673 K for 4 h in air. For both the C-TENG and the S-TENG, the maximum effective contact areas between the Ti foil and SiO_2 plate were 21 cm^2. For the R-TENG, there were 8 pieces of Au coating on the outside surface of the SiO_2 tube with two-two piece intervals connected in series to compose two electrodes. The maximum effective contact area between each Ti foil and SiO_2 segment with Au electrode was 19 cm^2.

3.3.4.2 Measurements of High Temperature TENG Performance

The TENGs were placed in a heating cabinet (Barnstead/Thermolyne 6000 furnace), which provided the desired temperature with an accuracy of ±5 K. The heating rate of the cabinet was about 7.5 K min^{-1}. For both the C-TENG and the S-TENG, a SiO_2 plate with Au coating was positioned on an insulating ceramic plate, and another ceramic plate was added between the Ti foil and steel holder. The top of the steel holder on the TENG extended out of the heating cabinet and was connected with a linear motor. Nickel wires were attached to the surfaces of the Au electrode and Ti foil and extended out of the heating cabinet. For the R-TENG, the SiO_2 tube was positioned between two stainless steel plates. There was a rotatable stainless-steel rod inside the SiO_2 tube with 4 pieces of Ti foils fixed on as rotor blades. The top of the steel rod extended out of the open hole on the heating cabinet and was connected with a rotary motor. Nickel wires were attached to the surfaces of each of the two Au electrodes and extended out of the heating cabinet. The environmental relative humidity was less than 30%. During the TENGs' performance measurements, the motor provided an accurate control of position and speed for the

mechanical stimulation, and the heating cabinet controlled the temperature. The relative humidity was measured by a Shaw Superdew 3 hygrometer. The open-circuit voltage V_{OC}, short-circuit current I_{SC} and short-circuit transfer charge Q_{SC} of the TENGs were tested under different temperatures after holding for 15 min by a Keithley 6514 electrometer. The microscope images of Ti foil and SiO_2 were measured by a Hitachi SU8010 field-emission SEM. The normal forces between Ti foil and the SiO_2 tube of the R-TENGs were measured by a Vernier LabQuest Mini force dynamometer.

CHAPTER 4. PEROVSKITE IN TRIBOELECTRIC NANOGENERATORS

4.1 Organo Metal Halide Perovskite Hybrid Photoelectric/Triboelectric Energy Harvesting Performance in a Triboelectric Nanogenerator and the Impacts of Surface Modification and Interfacial Engineering

4.1.1 Introduction

Triboelectric surfaces in TENGs may be fabricated from more or less any material with a characteristic charge affinity, including polymers, ceramics, textiles, and semiconductors. The triboelectric charge density transferred between two materials upon contact depends on the materials' capability to lose or gain electrons, which is dependent on physical properties. In recent years, organic-inorganic perovskites have attracted a great amount of interest due to their high power conversion efficiency (PCE) (> 20%) in solar cells, and could ideally replace silicon solar cells commercially given high enough performance enhancement, ease of access, and stability.[123, 124] They hold great potential in charge transport and energy harvesting, due to their high absorption coefficient of visible light, high carrier mobility, and long carrier recombination lifetime.[125-127] The generic chemical formula of perovskite is ABX_3, where the A^+ site contains monovalent cations (e.g., $CH_3NH_3^+$, $CH(NH_2)_2^+$, or Cs) and B^{++} sites contain divalent cations (e.g., Pb^{2+} or Sn^{2+}) and the X^- site contains anions (e.g., Cl, Br, I).[128] Challenges faced by the broad commercialization of organic-inorganic perovskite materials include stability in ambient environments, which may be improved by cation substitution and other methods, including

encapsulation by alumina/silica or amphiphilic diblock copolymers.[129-131] Hybridization of perovskite solar cells and TENGs has been performed before with great degrees of success, and produces more efficient natural energy conversion devices that still operate when there is a lack of either sunlight or rainwater/wind motion.[132] Not only can perovskite solar cells act as powerful light energy harvesters through charge separation, but perovskite itself has potential as a mechanical energy harvesting material.

Perovskites are appealing triboelectric materials for TENGs due to their unique dielectric and electric properties.[133, 134] Hybrid photoelectric/triboelectric nanogenerators have been made possible using perovskites such as methylammonium lead triiodide organometal halide ($MAPbI_3$), demonstrating the potential of electron-hole charge carrier separation in increasing surface electron density.[135] On one side, crystalline $MAPbI_3$ capped by $MAPbI_3$ nanoparticles was used as an electron-depleted surface with a 300-nm thick electron transfer layer made up of mesostructured TiO_2 beneath it, as well as fluoride doped tin oxide (FTO) coated glass as an electrode and substrate (**Figure 41a**). The opposing electron-donating triboelectric surface was composed of a conventional PTFE film attached to a copper electrode and an acrylic substrate. The underlying mechanism of surface charge enhancement relies on charge carrier separation from photon excitement and action of the electron transporting layer TiO_2, producing an even more positively charged $MAPbI_3$ surface by transporting electrons away from the triboelectric surface. The electrical output of the TENG was enhanced by the presence of simulated sunlight, as shown in **Figure 41b**, and by up to 11% for both the V_{OC} and I_{SC}, and 9% for the Q_{SC}. This study was the first to demonstrate a hybrid photoelectric and triboelectric energy harvesting device. However, similar studies, which would be of great interest, are very few and far

between. Only recently in 2019, results that showed similar trends were produced by Yang et al. using a $MaPbI_xCl_{3-x}$-based TENG with TiO_2 as an electron transport layer (ETL) and pentacene as a hole transport layer (HTL) and outermost triboelectric surface, all on a FTO-coated glass substrate (**Figure 41c**, where ETL and HTL are on the opposite side of the photoactive $MaPbI_xCl_{3-x}$ layer).[136]

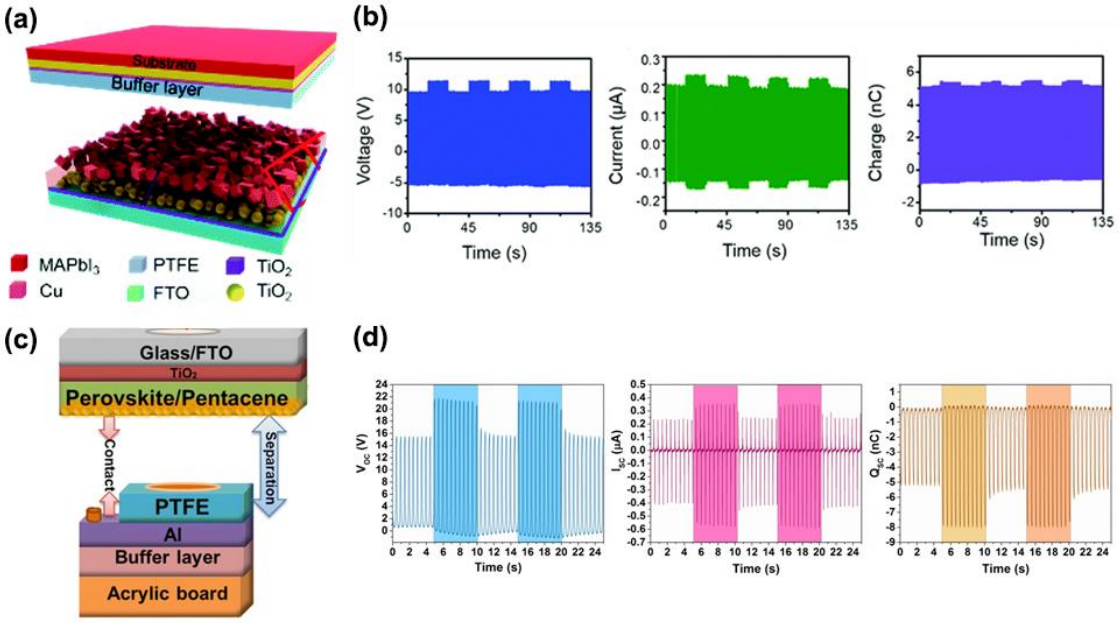

Figure 40. Hybrid photoelectric and mechanical energy harvesting perovskite TENGs. (a) Schematic of $MAPbI_3$ and TiO_2 ETL-containing TENG. (b) Electrical output of $MAPbI_3/TiO_2$ TENG under periodic visible light stimulation. Reproduced with permission.[135] Copyright 2016, The Royal Society of Chemistry. (c) Schematic of $MAPbI_3$, TiO_2 ETL, and pentacene HTL-containing TENG. (d) Electrical output of pentacene/$MaPbI_xCl_{3-x}/TiO_2$ TENG under periodic visible light stimulation. Reproduced with permission.[136] Copyright 2019, Springer Nature.

In this case, the reasoning behind the addition of TiO_2 was that the photo-induced electrons would increase the charge flow between the aluminum and FTO electrodes by traveling away from the perovskite. In addition, photo-induced holes would increase the positive triboelectric charges at the contact interface between PTFE and pentacene. With

an electron-donating opposing surface of PTFE and an aluminum electrode, the TENG was able to produce a 55.7% increase in V_{OC}, 50.8% in I_{SC}, and 58.2% in Q_{SC} (**Figure 41d**).

The significant increases in electrical output by the photoelectric charge carrier separation behavior of perovskites are demonstrative of their powerful application in TENGs. Also of recent interest is the potential of perovskites as triboelectric materials based on their unique dielectric characteristics and manipulability by surface passivation. Wang et al. used a $CsPbBr_3$ thin film in TENG measurements with varying degrees of Ba^{2+} ion doping in order to elucidate what factors improved the TENG's performance.[137] The opposing triboelectric surface was fabricated from a polyvinylidene fluoride (PVDF) film on a silver electrode, and the perovskite layer was fabricated atop a FTO layer on glass. Ba^{2+} ions were chosen as the dopant due to its large radius out of accessible alkaline-earth metals, which produces a greater extent of microstructure modulation, as well as its impact on the electrical properties of perovskite thin films.[138] As shown in **Figure 41a**, increases in Ba^{2+} ion concentration effectively reduced the grain size of the $CsPb_{1-x}Ba_xBr_3$. This was possible through reduction of perovskite formation energy and faster crystal nucleus formation by lattice expansion of the larger Ba^{2+} ions. Notably, the Ba^{2+} ion content of $CsPb_{1-x}Ba_xBr_3$ thin films should not pass a certain threshold ($x > 0.09$), since the possibility of pinholes and cracks forming break down the film's compactness, exposing the underlying FTO electrode to the PVDF and decreasing electrical output. According to electrical output data in **Figure 41b-c**, they were able to deduce that the highest electrical output was produced by a molar ratio of Pb:Ba of 0.91:0.09. Their perovskite thin film synthesis technique was also able to produce very large area devices (8.1 cm^2), and a $CsPb_{0.91}Ba_{0.09}Br_3$ TENG of this size was able to produce an impressive V_{OC} of 220 V and

a short circuit current density J_{SC} of 22.8 mA m^{-2}, with a power density of 3.07 W m^{-2}. This trend in improving perovskite TENG performance is the reverse of common methods to improve PCE of perovskite solar cells, which usually seek to enlarge grain size and passivate the surface.[139-141] Not only was the grain size effective in increasing TENG performance due to the increase in grain boundaries that serve as charge traps, but the dielectric constant of $CsPb_{1-x}Ba_xBr_3$ was also at its highest when the Pb:Ba ratio was 0.91:0.09 (**Figure 41d**). This is due to the space charge polarization enhancement from Ba^{2+} ions, which contributes to charge carrier migration in a material creating spatial inhomogeneity of charges, producing an electrostatic potential gradient in the perovskite film.[142] Moreover, the perovskite TENG devices maintained stability in performance after being stored in an ambient environment for 90 days, as well as full recovery of performance after mild degradation in varying humidity (30 to 80%) and temperature (20 to 80 °C) cycling. These factors all make cesium lead halide perovskite $CsPbX_3$ a highly appealing material for TENGs, and opens up a whole new application for stable inorganic halide perovskites owing to their particularly high dielectric constant (15-30) compared to conventional TENG materials (PTFE ~2.0, PET ~3.0, Kapton ~3.0, and SiO_2 being 3.9 to 4.5).

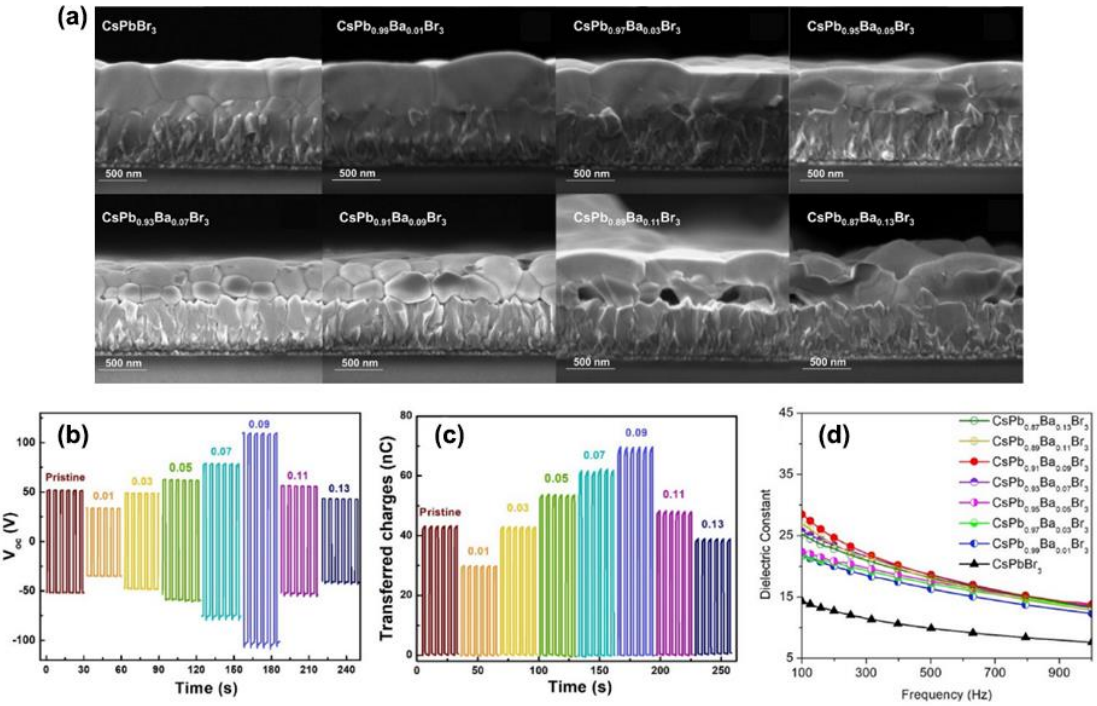

Figure 41. Characterization and performance of $CsPb_{1-x}Ba_xBr_3$ thin films in TENGs. (a) Cross-sectional SEM images taken from $CsPb_{1-x}Ba_xBr_3$ thin films while varying x from 0 to 0.13, on top of ITO-glass substrates. (b) Open circuit voltage (V_{OC}) and (c) transferred charge (Q_{SC}) measurements of $CsPb_{1-x}Ba_xBr_3$ TENGs with varying x. (d) Dielectric constant measurements taken over a frequency of 100 to 1000 Hz, while varying x from 0 to 0.13. Reproduced with permission.[137] Copyright 2020, Elsevier.

The historical usage of perovskite in TENGs has been brief and sporadic, and understandably so – perovskite is a material that is known for instability in ambient conditions and high temperature spin-coating and post-annealing processes. Moreover, synthesis methods and modulation techniques for perovskite are largely tuned for their usage in solar cells,[125, 126, 141, 143-157] and methods to improve their performance in TENGs are comparatively few and limited in scope.[135-137] However, the potential of perovskite as a TENG material is exceedingly high, as demonstrated not only by its possible hybrid photoelectric/triboelectric energy harvesting capabilities, but also by its exclusive electrical properties. In this context, we report a unique six component organic-inorganic lead halide

perovskite cesium formamidinium methyl ammonium lead bromide-iodide, or $Cs_y(MA_{0.17}FA_{0.83})_{(1-y)}Pb(I_{0.83}Br_{0.17})_3$, with its stability and facile synthesis making it a highly appealing triboelectric material. The addition of formamidinium (FA), $CH(NH_2)_2^+$, increases stability and extends light absorption thanks to a band gap that is closer than that of methylammonium (MA) to the optimal band gap for a single junction solar cell.[143, 144] FA-containing perovskites also have an absorption spectrum that further encompasses red wavelengths over MA-containing perovskites, leading to higher current densities.[158] However, FA being the sole A-site cation produces compounds that transform to the yellow polymorph δ phase, which is unsuitable for various perovskite applications since it is photovoltaically inactive.[159] In our case, mixing FA and MA prevents formation of the yellow polymorph and increases stability.[160] Cesium ions are added as inorganic cations to stabilize FA/MA-containing organic-inorganic perovskites in the desired α and β phases, due to the mixing entropy leading to a reduction of free energy in these phases.[145, 149] A Cs/FA/MA mixed cation perovskite was capable of maintaining its PCE above 18% at an unprecedented 250 hours in an ambient environment.[150] Additionally, Cs can induce highly uniform perovskite grains from the electron to the hole collecting layer, which promotes stable performances in applications.[150] Mixed halides may impact the refractive index, bandgap, extinction coefficient, and absorption coefficient of the perovskite, and partial iodide/bromide replacement has shown to be promising in enhancing current density.[146, 161]

Despite the seemingly high quantity of components of this perovskite, the fabrication process is a one-step spin-coating procedure and requires only a moderately high synthesis temperature. Therefore, the great appeal of $Cs_y(MA_{0.17}FA_{0.83})_{(1-}$

$_{y)}Pb(I_{0.83}Br_{0.17})_3$ in energy harvesting applications is evident, and should be investigated for both its excellent photoelectric and triboelectric capabilities. In this study, we investigate the impact of interfacial layers on electrical output of the TENG under illumination. Moreover, the surface topography of the perovskite, which is crucial to optimizing TENG output, may be readily manipulated through chemical passivation and variations in precursors. We also systematically vary the concentration of certain ions in the perovskite composition to observe the effects on grain size, crystallinity, and TENG electrical output. Our study would be one of few existing perovskite TENG investigations, the most recent being published in 2020, and would be of great merit towards expanding and commercializing functional material TENGs. Our findings would also promote this facile synthesis, high potential perovskite in the realm of solar cell and energy harvesting device enhancement.

4.1.2 Results and Discussion

4.1.2.1 Characterization of $Cs_y(MA_{0.17}FA_{0.83})_{(1-y)}Pb(I_{0.83}Br_{0.17})_3$ Perovskite Thin Films

A key factor of improving the performance of perovskite TENGs has been found to be diminishing the grain size (i.e., the presence of more grain boundaries) of perovskite while still maintaining the integrity of the crystalline thin film,[137] which may be accomplished by several methods. These include decreasing annealing temperatures, using a mesostructured ETL as a substrate for perovskite synthesis,[135, 162] and adjusting concentrations of perovskite precursors. These techniques have largely been extrapolated by a reversal of common surface passivation techniques that seek to enlarge grain size, in an effort to increase charge trap density and effective surface area on the perovskite surface.

The total precursor concentration has been shown to have an effect on grain size, as lower concentrations result in thinner films with smaller grain sizes,[152] yet this should be modulated carefully in order to not compromise the film integrity. In addition, the morphology of the perovskite film is also affected by its composition and the corresponding precursor solution. Therefore, we seek to systematically vary the molar concentration of CsI:(FAMA), which are all A-site cations of larger size, in order to impact the surface morphology of $Cs_y(MA_{0.17}FA_{0.83})_{(1-y)}Pb(I_{0.83}Br_{0.17})_3$.

We fabricated a range of triple cation mixed halide perovskite thin films on ITO substrates in order to act as TENG triboelectric materials. This was performed using a simple one-step spin coating method involving a precursor solution in DMF/DMSO and an antisolvent.[150] By adjusting the molar ratio of CsI in the precursor solution, we intend to manipulate the surface morphology and grain size of the $Cs_y(MA_{0.17}FA_{0.83})_{(1-y)}Pb(I_{0.83}Br_{0.17})_3$ thin films and observe their subsequent performance in TENGs. The UV-Vis spectra in **Figure 42a** shows that the absorbance generally decreased as a greater quantity of CsI was introduced into the precursors, particularly in the region of 800-550 nm wavelength. The films' spectra show a common band edge around 770 nm increasing up to 520 nm with a broad lead halide absorbance around 400-500 nm. Also, two secondary absorption peaks may be visible at around 440 nm for the samples with the highest Cs content (**Figure 42b**) that may have resulted from phase segregation due to the large size mismatch between Cs and FA, and formation of $CsPb(I_xBr_{1-x})_3$ from this separation.[163] We may infer that the perovskite thin film surface morphology and coverage may improve with less addition of CsI, albeit the benefits of Cs in suppressing the yellow phase and improving thermal stability and robustness have been well studied.[145, 150] Cs lowers the effective A-

site cation radius and shifts the tolerance factor towards a cubic lattice structure, which corresponds with the desired black perovskite phase.[164]

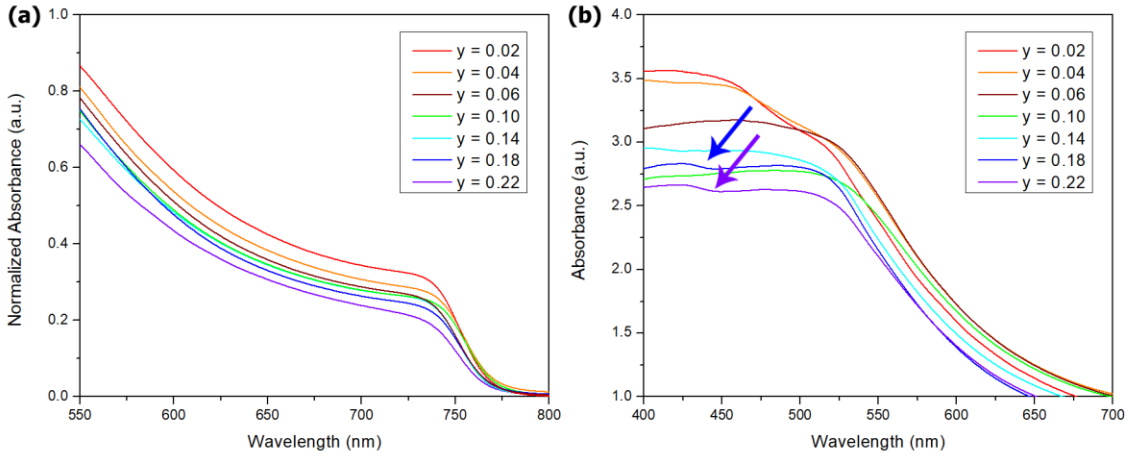

Figure 42. UV-Vis spectra of $Cs_y(MA_{0.17}FA_{0.83})_{(1-y)}Pb(I_{0.83}Br_{0.17})_3$ perovskite thin films with varying molar ratios of cesium. (a) Normalized UV-Vis spectra. (b) UV-Vis spectra showing possible $CsPb(I_xBr_{1-x})_3$ peaks from phase segregation.

The band gap energy for each specimen was calculated from the intercept of tangent lines to the UV-Vis peaks ranging from 725 to 775 nm using Equation 18:

$$E_g = \frac{1240}{\lambda} \tag{17}$$

where λ is the intercept of tangent lines to the UV-Vis peaks on X axis.[165] The band gap energy values for each sample are listed subsequently in **Table 2**. There was no apparent change in color to the visible eye with different molar ratios of CsI.

Table 2. Band gap values calculated from UV-Vis absorbance spectra for $Cs_y(MA_{0.17}FA_{0.83})_{(1-y)}Pb(I_{0.83}Br_{0.17})_3$ thin films.

Molar Ratio of Cs in $Cs_y(MA_{0.17}FA_{0.83})_{(1-y)}Pb(I_{0.83}Br_{0.17})_3$	Band Gap Energy (eV)
0.02	1.605
0.04	1.608
0.06	1.610
0.10	1.611
0.14	1.612
0.18	1.613
0.22	1.614

In general, the band gap energy tends to increase with increased Cs content in the perovskite thin film, which correlates with trends seen before in a study modulating Cs content in Pb-based perovskites.[166] This increase is very slight however, this is because the band gap of these metal halide perovskite materials is mainly determined by the orbitals of the halide and the divalent metal cation. The substitution of the cations (A-site) can also redefine the band gap of a perovskite due to octahedral tilting of the perovskite crystal lattice, reducing metal-halide orbital overlap and moves the bands to deeper energies thus increasing band gap.[167] FA (2.53 Å) and MA (2.17 Å) have larger ionic radii than Cs (1.67 Å),[167] so a higher Cs content in the perovskite would cause increased tilting from the reduced space filling offered by the smaller Cs ions. Although the band gap energy range achieved from CsI modulation is not very large based on our sample population, the role that A-site cations play in tuning this value is evident from our results. With slight precursor adjustments able to produce different band gap energies from 1.605 eV to 1.614 eV, it is possible that even more experimental variable manipulation could result in a greater variety of band gaps. There are a great number of unknown variables that could affect large scale production of perovskites, so every factor must be considered, including temperatures, spin

coating conditions, and annealing times. The addition of Cs increases thermal stability of triple cation mixed-halide perovskites,[150] but may also lead to unforeseen effects on the thin film integrity, i.e. phase segregation at high Cs molar ratios, as shown in our experiments.

The variation of CsI precursor also resulted in the variation of the perovskites' steady state photoluminescence (PL) spectra, as shown in **Figure 43a-b**. After normalization, the blue shift in PL from increasing the Cs molar ratio is apparent, especially in the magnified peak diagram in **Figure 43b**. This correlates to the blue shift from literature when Cs was increased from 0 to 15% in a similar triple cation mixed halide perovskite.[150] The peak apex wavelength for a Cs molar ratio of 0.02 is 776.7 nm, 0.04 is 776.3 nm, 0.06 is 776.02 nm, 0.10 is 775.4 nm, 0.14 is 774.9 nm, 0.18 is 774.5 nm, and 0.22 is 774.3 nm. From these values, we can see that the blue-shift in PL peak wavelength is not very drastic but still holds true, in good agreement with the slightly increased band gap of the corresponding perovskite films.

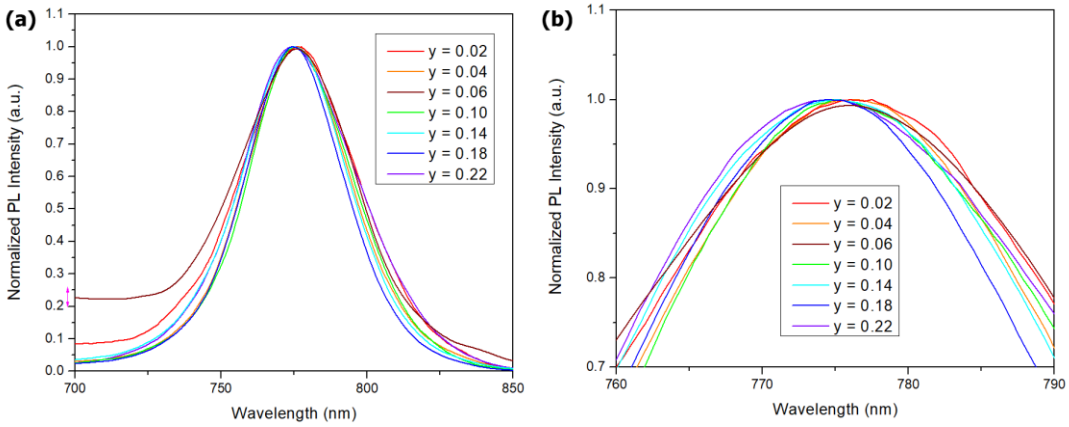

Figure 43. Normalized steady state PL spectra of $Cs_y(MA_{0.17}FA_{0.83})_{(1-y)}Pb(I_{0.83}Br_{0.17})_3$ perovskite thin films with varying molar ratios of cesium. (a) Normalized PL spectra. (b) Magnification of normalized peaks showing blue shift in PL with increase in Cs.

Our Cs-varying TENG experiments are less dependent on the band gap energy and photoelectric performance of $Cs_y(MA_{0.17}FA_{0.83})_{(1-y)}Pb(I_{0.83}Br_{0.17})_3$ and more so on the grain size and surface morphology due to the surface charge density-based current generation of TENGs. Therefore, it is imperative to investigate the effects of CsI variation on these factors. CsI was chosen as the precursor to manipulate due to its relatively smaller molar ratio in the entire composition as compared to the other A-site cations. In this way, changing it would likely have a lesser impact on the integrity and crystalline nature of the perovskite thin film. Indeed, the films fabricated with varied Cs content produced dark, stable layers of perovskite that showed little to no degradation from environmental factors such as light and humidity. Samples were stored in a desiccant container, and minimal exposure to these factors was maintained. Further stability tests may be performed in the future. Even after TENG operation using a linear motor that pressed the perovskite against a PTFE triboelectric surface, the perovskite films were imaged using a SEM following Au sputtering and showed few scratches and defects from this process (**Figure 44a-g**). It may be observed that several scratches are visible in a minority of the samples, particularly in the y = 0.18 CsI sample (**Figure 44f**), but overall the film was quite robust even under a strenuous process like TENG operation. Additionally, pinholes may be seen in **Figure 44e-g** since these films are not compact, and thus the higher CsI content may affect the crystallization of the perovskite and phase separation may have occurred.[150] From a brief glance, it may be observed that the grain sizes of $Cs_y(MA_{0.17}FA_{0.83})_{(1-y)}Pb(I_{0.83}Br_{0.17})_3$ generally increase with greater CsI concentration in the precursor solution. However, this also leads to somewhat of a decrease in structural integrity as more surface defects are visible following TENG operation. Since surface passivation is key for improving

photovoltaic device performance, it appears that modulating Cs may be an effective intrinsic method for producing perovskite thin films of tunable grain size. Also, optical microscope images of the perovskite grains in **Figure 44h-i** show a noteworthy pattern that emerges above a certain threshold concentration of CsI. At lower concentrations, the grains are uniform and very few aberrations may be observed. However, above y = 0.18, characteristic ridged formations appear in the perovskite, which may be unfavorable for photovoltaic applications that rely on the passage of light through the material. These ridges may have resulted from phase segregation due to high Cs content as seen in the UV-Vis results in **Figure 42b**. In order to harness CsI modulation as a surface passivation tool, its effects should be fully taken into consideration. Our TENG studies welcome the addition of surface roughness and reduction of grain size for improved triboelectric output, however, and the appearance of these patterns at higher CsI concentrations may be a boon.

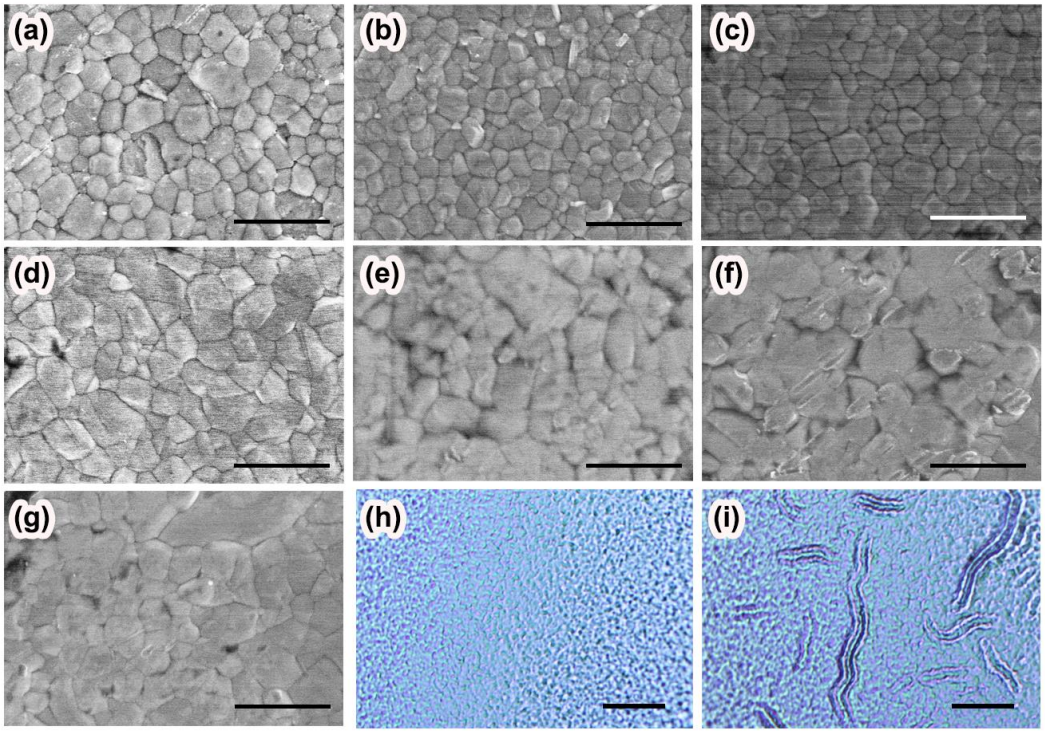

Figure 44. SEM and optical microscope images of $Cs_y(MA_{0.17}FA_{0.83})_{(1-y)}Pb(I_{0.83}Br_{0.17})_3$ thin films on ITO-coated glass substrates following TENG operation and Au sputtering. (a) SEM images of $Cs_y(MA_{0.17}FA_{0.83})_{(1-y)}Pb(I_{0.83}Br_{0.17})_3$ thin films with y = 0.02, (b) y = 0.04, (c) y = 0.06, (d) y = 0.10, (e) y = 0.14, (f) y = 0.18, and (g) y = 0.22. Scale bars indicate 1 μm. (h) Optical microscope images of $Cs_y(MA_{0.17}FA_{0.83})_{(1-y)}Pb(I_{0.83}Br_{0.17})_3$ thin films with y = 0.10 and (i) y = 0.22. Scale bars indicate 20 μm.

Further characterization of surface morphology is required in order to fully investigate the effects of CsI variation on the formation of the perovskite crystalline layer. Multiple atomic force microscopy (AFM) scans of each perovskite sample were obtained and used to calculate the distribution of grain sizes across each variant. As shown in **Figure 45**, larger grain sizes were observed for an increase in Cs content. The difference between the highest and lowest points of each scan was similar throughout at about 100 to 110 nm, with the greatest difference being that of the sample with a CsI molar ratio of 0.18, with a difference of 150 nm due to the presence of a particularly large grain (**Figure 45f**). Additionally, it appears as though the spacing and distinctiveness of each grain increases

with an increase in Cs content, along with the grain size. The grain boundaries grow more clear even with a slight increase in Cs in the composition, as they are not as enunciated in the perovskite layer with a CsI molar ratio of 0.02 (**Figure 45a**). As with the SEM images, noticeable morphological trends are observed in the AFM scans, and these characteristics all have the potential to affect the perovskite layer's performance in generating charge in a TENG. The average grain size was calculated using ImageJ software and both SEM and AFM images for all samples, and the results are tabulated in **Table 3**. The grain sizes more than double when Cs content is raised from a molar ratio of 0.02 to 0.18, and the increase tapers seems to taper off after this.

Table 3. Average grain size of $Cs_y(MA_{0.17}FA_{0.83})_{(1-y)}Pb(I_{0.83}Br_{0.17})_3$ perovskite thin films with varying Cs content.

Molar Ratio of Cs in $Cs_y(MA_{0.17}FA_{0.83})_{(1-y)}Pb(I_{0.83}Br_{0.17})_3$	Average Grain Size (μm^2)
0.02	3.86×10^{-2}
0.04	4.20×10^{-2}
0.06	5.01×10^{-2}
0.10	7.86×10^{-2}
0.14	8.96×10^{-2}
0.18	1.53×10^{-1}
0.22	1.13×10^{-1}

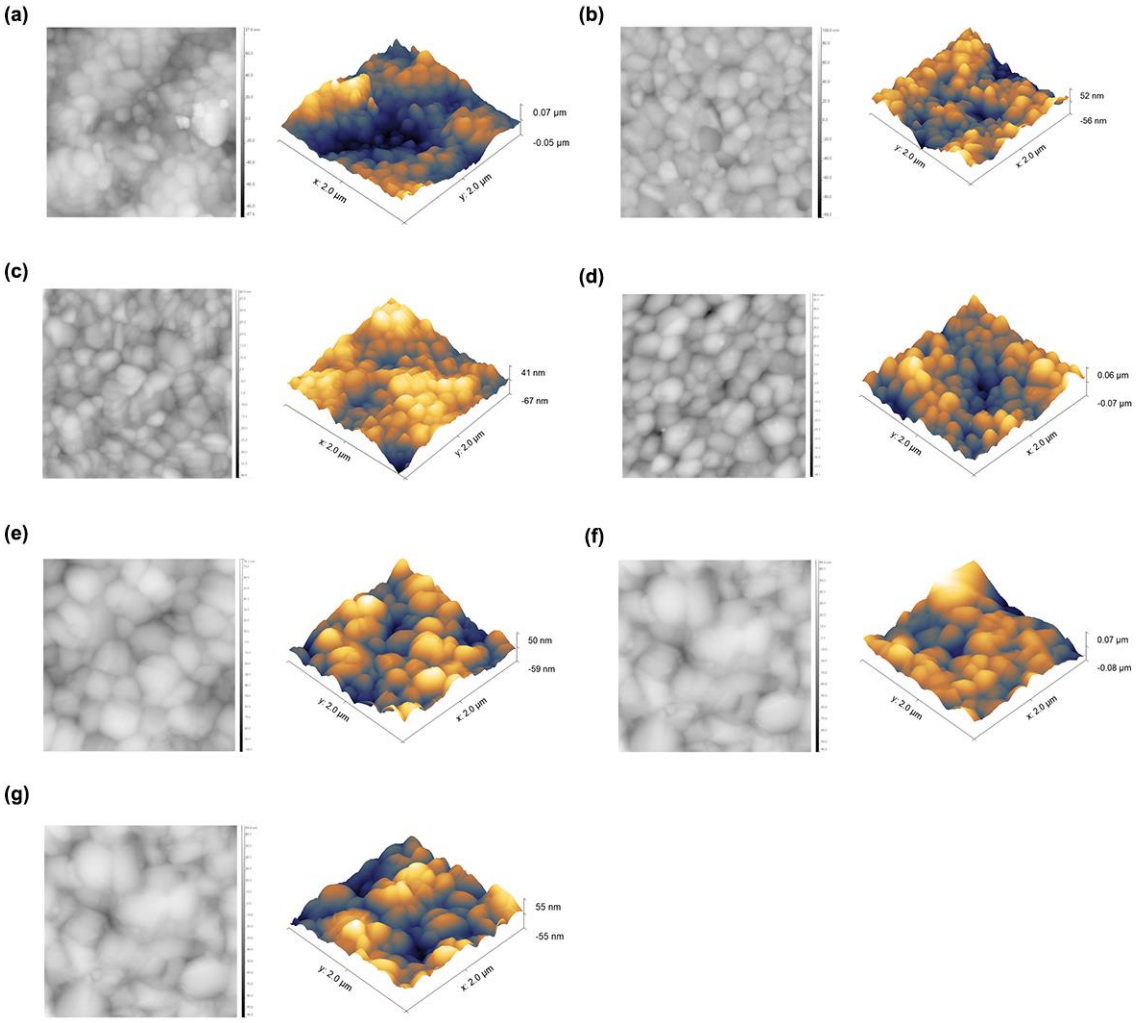

Figure 45. AFM scans of $Cs_y(MA_{0.17}FA_{0.83})_{(1-y)}Pb(I_{0.83}Br_{0.17})_3$ thin film surfaces in 2D and 3D representations. (a) Scan of $Cs_y(MA_{0.17}FA_{0.83})_{(1-y)}Pb(I_{0.83}Br_{0.17})_3$ with y = 0.02, (b) y = 0.04, (c) y = 0.06, (d) y = 0.10, (e) y = 0.14, (f) y = 0.18, and (g) y = 0.22. Dimensions of AFM scans are all 2 µm by 2 µm.

A grain size distribution analysis is performed in **Figure 46**, with the percentages per grain area plotted, showing an increased uniformity of grains with an increase of Cs content. For instance, the thin films of $Cs_y(MA_{0.17}FA_{0.83})_{(1-y)}Pb(I_{0.83}Br_{0.17})_3$ with y = 0.02, 0.04, 0.06, and 0.10 (**Figure 46a-d** respectively) demonstrate a wide variety of smaller grain sizes with few large outliers. However, in more Cs-heavy compositions, such as y = 0.14, 0.18, and 0.22 (**Figure 46e-g** respectively), there appear more than a few grains that

are far larger than the rest. It is important to analyze the impact of surface passivation or manipulation techniques, as methods to control grain size can affect the surface and bulk properties of the material, causing defects and effects on crystallinity.[123] Not only the area, but also the feature height of grains, can factor into the surface's performance in a TENG device, as shown in many surface modification studies of TENGs.[168-170] Often, the existence of nano/micro-scale features on a material surface improve its triboelectric performance over that of a feature-less bare surface. The root mean squared (RMS) roughness of each SEM image of each perovskite variant was averaged and plotted in **Figure 46h**, which may be calculated using the following equation for the standard deviation of Z_n values for a sample area:

$$\mathrm{R}_{rms} = \sqrt{\sum_{n=1}^{N} \frac{(z_n - \bar{z})^2}{N}} \tag{18}$$

where $\bar{Z}$ is the mean value of the surface height relative to the center plane and N is the number of points in the sample area.[171] The RMS roughness shows a steep drop at first as the amount of Cs additive increases, which then has an upward swing past a molar ratio of y = 0.10, and finally fluctuates around a more stable value afterwards. Considering surface roughness is a key factor in determining the efficiency of a triboelectric surface in generating charges upon contact electrification, it is likely that these differences in roughness will impact the electrical output of the perovskite layer. However, as with any TENG study, the results may differ from the expected outcome of higher roughness resulting in higher electrical output.

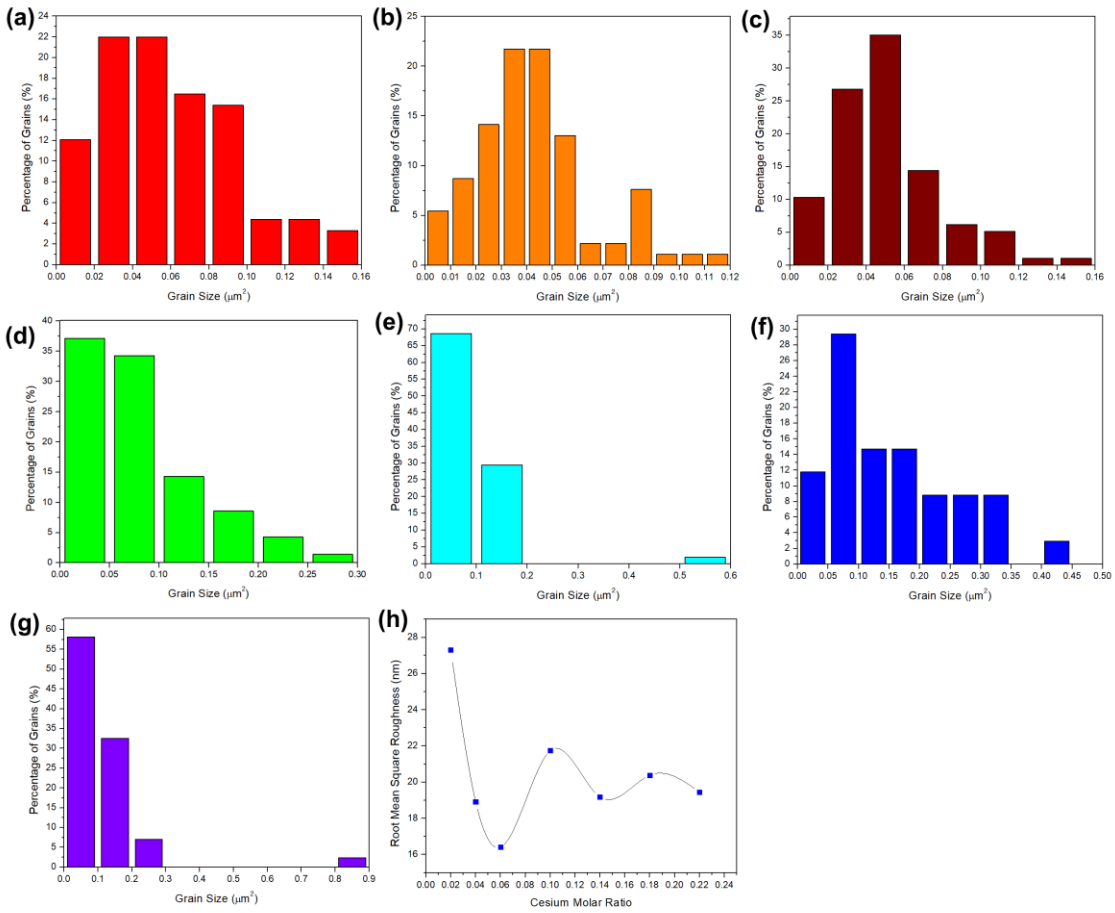

Figure 46. Grain size distributions from AFM and SEM image analysis. (a) Percentage of grain sizes for $Cs_y(MA_{0.17}FA_{0.83})_{(1-y)}Pb(I_{0.83}Br_{0.17})_3$ of y = 0.02, (b) y = 0.04, (c) y = 0.06, (d) y = 0.10, (e) y = 0.14, (f) y= 0.18, and (g) y = 0.22. (h) Plot of average root mean square (RMS) surface roughness calculated over all AFM images of each perovskite variant.

4.1.2.2 $Cs_y(MA_{0.17}FA_{0.83})_{(1-y)}Pb(I_{0.83}Br_{0.17})_3$ Grain Size Modulation and TENG Output

There exist many unique distinctions in the $Cs_y(MA_{0.17}FA_{0.83})_{(1-y)}Pb(I_{0.83}Br_{0.17})_3$ thin films fabricated using varying molar ratios of Cs, as can be observed in the topological characterizations of said films. However, the role these play in triboelectric charge generation as the films are used in TENGs must be further investigated. Indeed, there exists a clear trend in electrical output from these perovskite films, showing a clear difference in surface charge generation according to morphological differences. The perovskite-based

TENG was constructed using exposed ITO coating the glass substrate as the electrode of the perovskite side, and a copper film as the electrode of the PTFE side. The V_{OC}, I_{SC}, and Q_{SC} all show a distinct difference for $Cs_y(MA_{0.17}FA_{0.83})_{(1-y)}Pb(I_{0.83}Br_{0.17})_3$ with varying molar ratios of Cs (**Figure 47a-c**). The average grain sizes in **Figure 47d** may be used as a comparative measure. In fact, larger grain sizes decrease the electrical output up to 26.5% when comparing the V_{OC} of the TENGs made from perovskites of y = 0.02 and y = 0.14. However, even with their large grain sizes the perovskite specimens with y = 0.18 and y = 0.22 demonstrate electrical outputs that are almost on par with the samples with smaller grain sizes. We suggest that this could be tied to the unique features observed in those higher Cs content perovskites, such as the more easily damaged surface or lower robustness, which would be worse for long term TENG/photovoltaic performance due to the prevalence of defects and possible creation of holes. However, the malleability of the surface of these samples could lead to increased surface contact area of the perovskite with PTFE, resulting in higher electrical outputs despite the larger grain sizes.

The aforementioned reasoning behind smaller grain size perovskites performing better in TENG is that they increase charge traps and surface roughness, which are both beneficial to surface charge density.[137] Also, the appearance of unique ridges of the perovskites with Cs content greater than y = 0.18 as shown in **Figure 44i** may factor into increased surface roughness as compared to that of a more uniform grain spread seen in lower Cs content films. Using perovskite to create hybrid photoelectric/triboelectric devices of high efficiency requires compromising on the particular qualities that encourage better performance in both areas. Grain size diminishment is certainly one aspect that has a great deal of potential in improving TENG output, but it must be tempered due to its

impact on photoelectric effectiveness. When examining the trends in maximum grain height and RMS roughness of the portions of the perovskite layer imaged by AFM in **Figure 46h-i**, there appear to be a number of unique traits of each perovskite variant that are behind its electrical output performance. For instance, for y = 0.02, the high RMS roughness could contribute to its high TENG output, and subsequent decreasing of the RMS roughness does correspond to a decrease in electrical signals as well. However, at y = 0.10 the slight rise in RMS roughness did nothing to impede this decrease of electrical output, which perpetuates until y = 0.18, which shows a particularly large grain height and yet a lower RMS roughness. At this point, the electrical outputs start increasing with higher Cs content, despite y = 0.18 having the largest grain size of all the variants. However, the V_{OC}, I_{SC}, and Q_{SC} of the perovskite specimens above y = 0.18 Cs molar ratio have lower values overall compared to the smaller grain size variants below y = 0.06, showing that grain size does indeed have an impact on tempering electrical output in a TENG. The most ideal variant of our triple cation mixed-halide perovskite for generating triboelectric charges was $Cs_{0.02}(MA_{0.17}FA_{0.83})_{(1-y)}Pb(I_{0.83}Br_{0.17})_3$, which had the lowest average grain size. Also, it may be surmised that the lack of such deep divots and rises contributed to improved surface contact overall. Also, this variant had the highest RMS roughness overall, which may have contributed to its higher surface area for generating charges as well. The least electrical output was resultant from the $Cs_{0.14}(MA_{0.17}FA_{0.83})_{0.86}Pb(I_{0.83}Br_{0.17})_3$ samples, which did not have the lowest RMS roughness nor the largest average grain size, but lacked the ridge-like formations from phase segregation that the variants with y = 0.18 and y = 0.22 had. Therefore, without any countermeasures for its lower RMS roughness and large grain size, it may have performed the worst due to these factors.

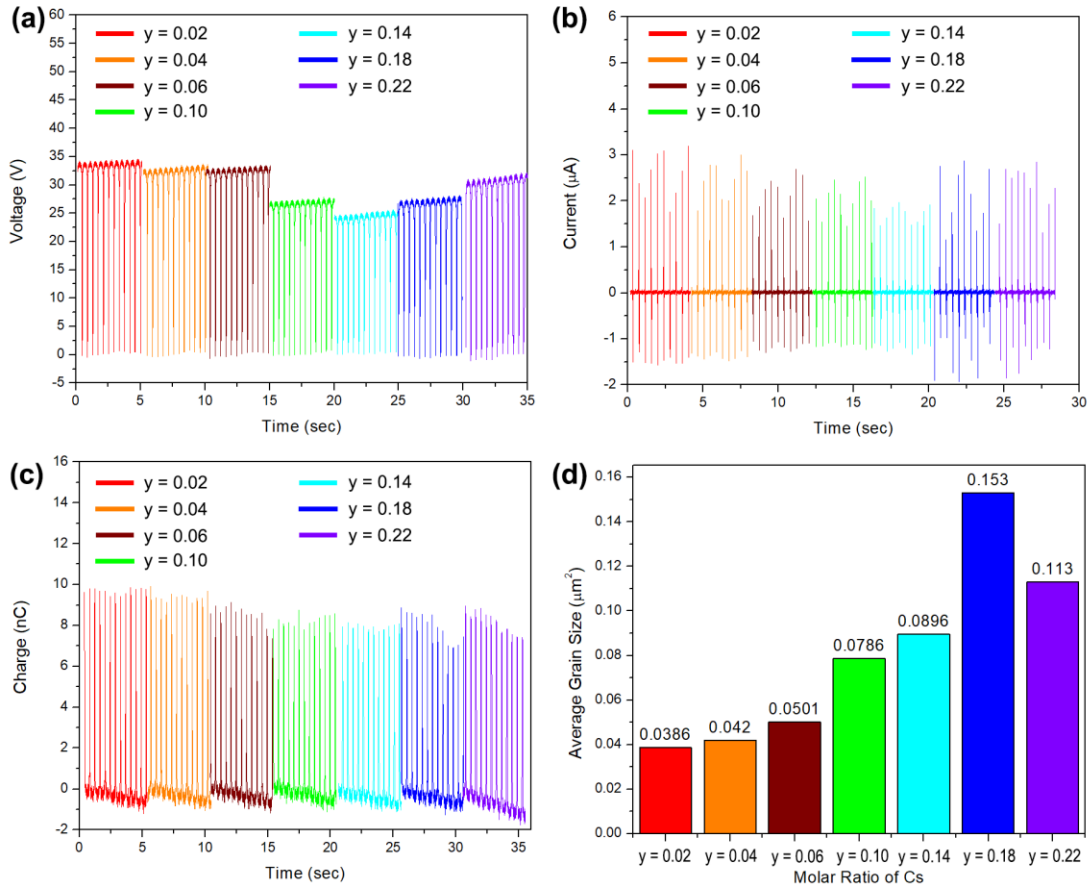

Figure 47. Performance of the $Cs_y(MA_{0.17}FA_{0.83})_{(1-y)}Pb(I_{0.83}Br_{0.17})_3$ films in a perovskite-based TENG. (a) Open circuit voltage V_{OC}, (b) short circuit current I_{SC}, and (c) transferred charge Q_{SC} are all plotted for each variant of Cs content. (d) Plot of average grain sizes of $Cs_y(MA_{0.17}FA_{0.83})_{(1-y)}Pb(I_{0.83}Br_{0.17})_3$ variants.

The variants with y = 0.04 and y = 0.06 had smaller average grain sizes than the highest performing composition, but their RMS roughness were much lower. The most robust perovskite thin films that showed the least friction damage after TENG operation were those with y = 0.06 and y = 0.10. Although a lower Cs content may result in smaller grain sizes, higher RMS roughness, and more contact surface area, the benefits of Cs in ensuring perovskite stability should not be entirely compromised for these factors. As a triboelectric material for TENGs, $Cs_y(MA_{0.17}FA_{0.83})_{(1-y)}Pb(I_{0.83}Br_{0.17})_3$ is both tunable

physically and chemically, and produces quite a significant electrical output for the small surface area of the device (~1.3 cm^2 effective contact area). Since the perovskite components are tailored for success as a highly stable and reliable optoelectronic application material, it presents an appealing material for use in making hybrid photon and mechanical energy harvesting devices.

4.1.2.3 Photoelectric Tests with $Cs_y(MA_{0.17}FA_{0.83})_{(1-y)}Pb(I_{0.83}Br_{0.17})_3$ TENG and Interfacial Layers

In order to investigate the photoelectric/triboelectric hybrid device potential of our unique six-component perovskite $Cs_{0.06}(MA_{0.17}FA_{0.83})_{(1-y)}Pb(I_{0.83}Br_{0.17})_3$, four main types of TENGs were fabricated according to **Figure 48**. We opted to use the y = 0.06 variant of perovskite due to its optimal performance in solar cell applications in existing literature, achieving a peak PCE of 21.1%.[150] Interfacial crystalline layers of SnO_2 acting as the ETL (as its crystalline form can be attained by spin-coating its precursors at room temperature) and 2,2',7,7'-Tetrakis[N,N-di(4-methoxyphenyl)amino]-9,9'-spirobifluorene (Spiro-MeOTAD) or poly(3-hexylthiophene) (P3HT), functioning as the HTL, were spin-coated on the perovskite triboelectric half. Since the SnO_2 is underneath the perovskite layer, it would pull electrons from photoinduced electron-hole pairs toward the electrode and increase charge flow between the indium tin oxide (ITO) electrode and copper electrode. Additionally, the HTL would promote a greater amount of positive charges generated once it contacts the PTFE film due to its tendency to attract holes. This would pair well with the

negatively charged PTFE film in producing an alternating current from contact-separation motion, and in turn enhance electrical output.

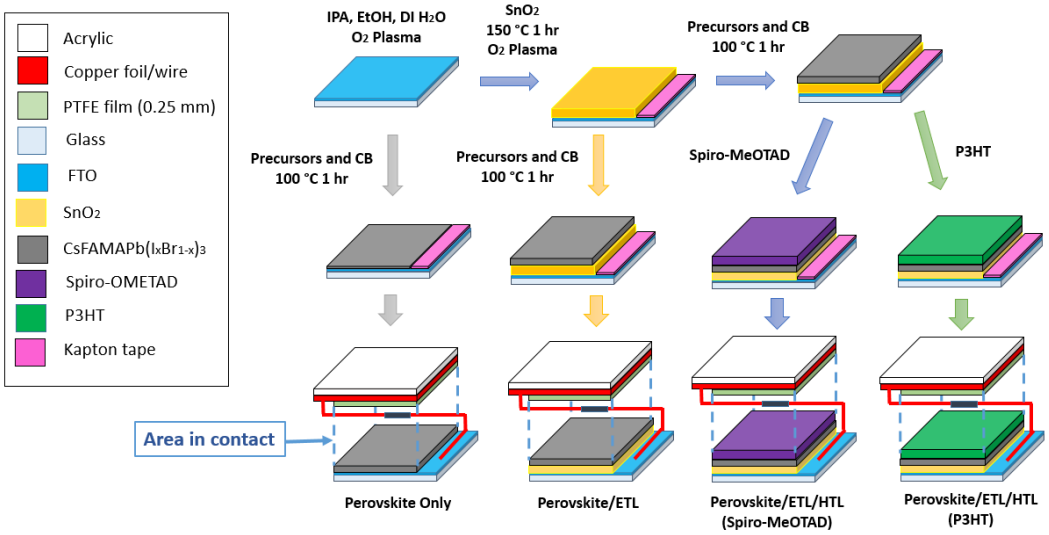

Figure 48. Fabrication schematic of $Cs_{0.06}(MA_{0.17}FA_{0.83})_{(1-y)}Pb(I_{0.83}Br_{0.17})_3$ TENGs. A flowchart showing the synthesis steps to achieve each variety of TENG with its individual interfacial layers.

The device surface area of each fabricated triboelectric half was 1.5 x 1.5 cm^2. The area in contact was smaller (1.5 x 1.2 cm^2) since the Kapton tape-masked area of the ITO electrode rendered a portion of the perovskite triboelectric half unable to contact the PTFE triboelectric half. It was found during testing that the Spiro-MeOTAD HTL was unsuitable as a TENG material, despite being ideal for solar cells due to its high solubility and suitable energy levels,[153] since the layer was too soft to keep its integrity during the contact-separation motion. The Spiro-MeOTAD would be abraded onto the PTFE half and cause erratic measurements from the electrometer that were unusable. However, replacing the HTL with P3HT, which also possesses greater stability, hole mobility, and conductivity than Spiro-MeOTAD,[155] solved the issue of material wear. The electrical output signals from the different types of TENGs tended to vary in their behavior when a lamp was shone

through the ITO glass backing the perovskite half in a darkened room. There were instances in which both the V_{OC} (**Figure 49a**) and I_{SC} (**Figure 49b**) increased upon exposure to light, which was the desired outcome. As observed by the distinctive patterns of both electrical outputs (**Figure 49c-d**), characteristic voltage peaks and an alternating current were obtained. This particular set of signals were obtained using a TENG with both an ETL and HTL, and when the lamp was stationed ~5 cm away from the perovskite layer. This increase was not consistent across the board of all the TENGs with both interfacial layers, and thus we are hesitant to attribute the rise in electrical output wholly to the addition of the HTL. Additionally, the switching on and off of the lamp failed to elicit the immediate enhancement and recovery of electrical output observed in previous hybrid studies.[135, 136] Many factors may play into the success of a hybrid photoelectric/triboelectric energy harvesting device, including individual qualities of the perovskite, conditions of testing, and quality of the contact between the layers of the TENG.

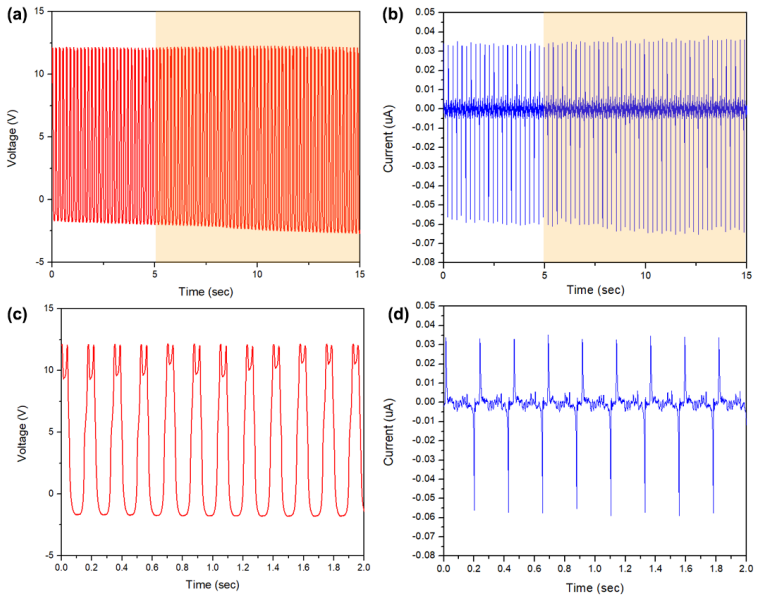

Figure 49. Increased electrical output signal using a $Cs_{0.06}(MA_{0.17}FA_{0.83})_{(1-y)}Pb(I_{0.83}Br_{0.17})_3/SnO_2$/P3HT TENG. (a) V_{OC} signal and (b) I_{SC} signal with a yellow

shaded box indicating when the lamp was turned on. (c) Distinctive patterns of the V_{OC} output and (d) I_{SC} output.

However, certain trends did surface from the data collected that are indicative of a measure of success. Overall, the interfacial engineering of the TENGs produced the most apparent differences in V_{OC} measurements, as shown in **Figure 50**. The TENGs with perovskite paired with an ETL and HTL tended to have an increase in V_{OC} upon illumination, with to a larger degree than that of those with perovskite and an ETL, or with only perovskite. Indeed, this suggests that the presence of a HTL in the TENG may increase the positive charge density on the surface of the perovskite triboelectric half upon contacting the PTFE film under illumination. This would in turn, improve the electrical output over that of the improvement from the presence of the ETL. The ETL can improve electrical output since it serves to drive electrons towards the ITO electrode to more efficiently under illumination, promoting greater electron flow between the ITO and copper electrodes to balance the potential difference from the operation of the TENG. However, not as much general improvement of I_{SC} was observed overall compared to V_{OC}, so this effect may not have been as pronounced in our measurements. According to the superposition principle of electric potential, triboelectric charge density can affect V_{OC}, I_{SC}, and Q_{SC}, but in this case the trends were not as strong for I_{SC} and Q_{SC} parameters as they were for V_{OC}.

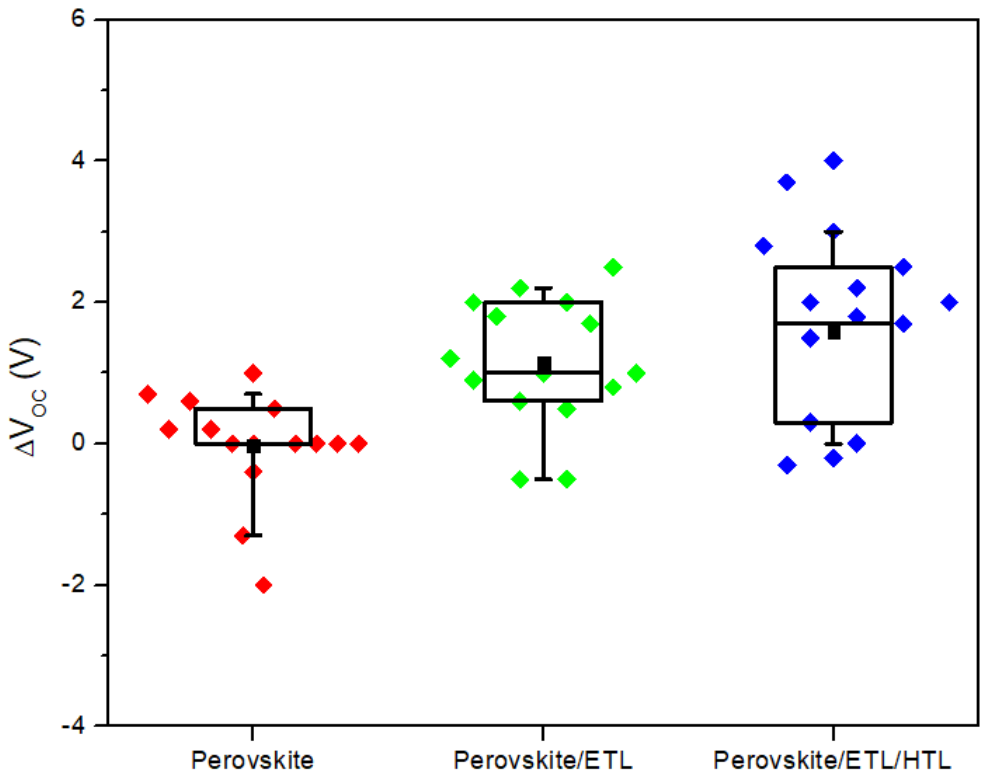

Figure 50. Box plot of changes in open circuit voltage under illumination.

The average increase in V_{OC} (2.11 V) of the $Cs_{0.06}(MA_{0.17}FA_{0.83})_{(1-y)}Pb(I_{0.83}Br_{0.17})_3/SnO_2$/P3HT TENG does not compare to the 6.9 V increase in the $MAPbI_xCl_{3-x}/TiO_2$/pentacene TENG from 2019,[136] but it is an improvement on the 1.7 V increase of the $MAPbI_3/TiO_2$ TENG from 2016.[135] This may be rationalized as follows: the addition of the P3HT hole transport layer increased the amount of positive charges that migrated to the surface due to its high hole affinity, so a perovskite TENG/photoelectric harvester made with only an ETL had less of an electrical output compared to one with an ETL and HTL. Also, pentacene (0.5 to 1.5 cm^2/Vs) has a much higher charge carrier mobility than P3HT (0.1 cm^2/Vs),[172] so it should also have a more effective improvement on perovskite photoelectric/triboelectric charge enhancement.

4.1.3 Conclusion

Perovskite has a great deal of potential both in energy harvesting applications using light as well as mechanical energy due to its tunable band gap energy, charge carrier mobility, and unique crystalline grain structure. Testing and characterizing the variety of thin films fabricated using a stable and high-performing triple cation mixed-halide perovskite $Cs_y(MA_{0.17}FA_{0.83})_{(1-y)}Pb(I_{0.83}Br_{0.17})_3$ showed that modulating the amount of CsI precursor had a profound effect on their surface morphology, hardness, RMS roughness, average grain size, and effective surface contact area. The synthesis technique was both facile and easily scalable, with a one-step spin coating scheme. Adding more Cs content both resulted in a higher band gap energy, lower absorption intensity, and a lower PL peak wavelength. We achieved the greatest amount of electrical output from a TENG using $Cs_{0.02}(MA_{0.17}FA_{0.83})_{0.98}Pb(I_{0.83}Br_{0.17})_3$, due to both its extremely high RMS roughness and its small average grain size. This variant produced the highest improvement in TENG output using these $Cs_y(MA_{0.17}FA_{0.83})_{(1-y)}Pb(I_{0.83}Br_{0.17})_3$ films, resulting in a 26.5% increase in V_{OC}, 24.4% increase in I_{SC}, and 17.5% increase in Q_{SC} over the lowest performing sample with a CsI molar ratio of 0.14. The hardest material resistant to scratches and surface defects following TENG testing was $Cs_{0.06}(MA_{0.17}FA_{0.83})_{0.94}Pb(I_{0.83}Br_{0.17})_3$, and the appearance of micro-scale ridges from possible phase segregation due to Cs and FA size mismatch on $Cs_{0.18}(MA_{0.17}FA_{0.83})_{0.82}Pb(I_{0.83}Br_{0.17})_{33}$ and $Cs_{0.22}(MA_{0.17}FA_{0.83})_{0.78}Pb(I_{0.83}Br_{0.17})_3$ seemed to offset some negative effects their larger grain size and lower RMS roughness would have on triboelectric charge generation. However, these ridges may have a negative impact on this perovskite material were it to be used in a hybrid photoelectric/triboelectric deice. Despite having the largest grain sizes

tested, the variants with the highest Cs molar ratios produced electrical signals that were higher than that of $Cs_{0.14}(MA_{0.17}FA_{0.83})_{0.86}Pb(I_{0.83}Br_{0.17})_3$ and $Cs_{0.10}(MA_{0.17}FA_{0.83})_{0.90}Pb(I_{0.83}Br_{0.17})_3$, which showed the lowest electrical output potential. If the beneficial stabilizing effects of Cs addition were to outweigh those of decreasing its concentration for the sake of smaller grain sizes and higher roughness, perhaps these higher Cs content samples would be ideal for fabricating hybrid photoelectric and triboelectric devices. However, these samples also faced the most surface frictional damage, so the benefits of adding Cs for hardness appear to fall off after a certain threshold point. In designing a stable, efficient, and ideal perovskite-based TENG, desired properties and which factors may lead to the optimal levels of those properties should be given much consideration. Further experimentation where other perovskite precursors and compositions should be carried out in order to determine the best path forward.

Stable perovskites hold great potential as multifunctional triboelectric materials capable of harvesting a myriad of sources of energy. In our study, a $Cs_{0.06}(MA_{0.17}FA_{0.83})_{(1-y)}Pb(I_{0.83}Br_{0.17})_3$ perovskite was used to create TENGs on its own and paired with interfacial layers of SnO_2, Spiro-MeOTAD, and P3HT. From our results, it can be seen that perovskites paired with an ETL and HTL perform better than those without (or with only an ETL or an HTL) in hybrid photoelectric/triboelectric energy conversion under illumination. As always, material selection should be carefully performed in order to create robust and high charge mobility interfacial layers. While Spiro-MeOTAD is a commonly used HTL in solar cells, its softer physical characteristics made it less suitable for TENG application. The qualities of $Cs_{0.06}(MA_{0.17}FA_{0.83})_{(1-y)}Pb(I_{0.83}Br_{0.17})_3$ that make it an ideal candidate for perovskite solar cells may not necessarily hold the same benefits for TENG

applications. Further experimentation is required in order to fully harness the favorable light harvesting characteristics of $Cs_{0.06}(MA_{0.17}FA_{0.83})_{(1-y)}Pb(I_{0.83}Br_{0.17})_3$ in a hybrid situation, and perhaps it would be more suitable to make a tandem triboelectric and photoelectric device with each component separate from the other. In this way, the unique photoelectric properties of the perovskite could be utilized to their maximum.

4.1.4 Experimental Section

Perovskite precursors, substrates, and anti-solvents, including cesium iodide (CsI, 99.999%), methylammonium bromide (MABr, ≥ 99%, anhydrous), lead(II) bromide ($PbBr_2$, 99.999%), lead(II) iodide (PbI2, 99.999%, perovskite grade), formamidinium iodide (FAI, ≥ 99%, anhydrous), indium tin oxide (ITO)-coated glass, and chlorobenzene (CB), were all purchased from Sigma-Aldrich. Solvents, including N,N-dimethylformamide (DMF, ≥ 99.8%), (trifiuoromethane)sulfonimide lithium salt, and dimethyl sulfoxide (DMSO, ≥ 99.9%), were purchased from VWR BDH. Interfacial layer materials, including Spiro-MeOTAD (99%), poly(3-hexylthiophene-2,5-diyl) (P3HT), and tin(IV) oxide (SnO2, ≥ 99.99%), were also purchased from Sigma-Aldrich. Acetonitrile was purchased from Alfa Aesar. All chemicals were used as received. TENG components, including 200 μm-thick PTFE film, Kapton tape, copper tape and wire, and 1/8 inch-thick acrylic sheets, were purchased from McMaster-Carr.

4.1.4.1 Fabrication of $Cs_y(MA_{0.17}FA_{0.83})_{(1-y)}Pb(I_{0.83}Br_{0.17})_3$ Perovskite Thin Films

In a glove box with an inert N_2 environment, the perovskite precursors were measured out for each synthesis batch in relative molar ratios of FAI (1) : PbI_2 (1.1) : MABr (0.2) : $PbBr_2$ (0.2) : CsI (0.006) : DMF (~8.6) : DMSO (~2.34). For the CsI precursor, a

1.5 M CsI in DMSO solution was prepared first and stirred until fully dissolved, and an aliquot was taken from that that varied according to the desired molar ratio. All perovskite precursors were mixed together and stirred for 24 hours until fully dissolved. In order to prepare the Spiro-MeOTAD for the HTL, 1 mL of a 72.3 mg/mL Spiro-MeOTAD in CB solution was added to 28.8 μL 4-tert-butylpyridine. Then, 520 mg/mL (trifiuoromethane)sulfonimide lithium salt in acetonitrile was prepared, and 17.5 μL of this solution was added to the Spiro-MeOTAD/CB/4-tert-butylpyridine solution. The P3HT HTL was prepared using 0.16 mM P3HT in chlorobenzene heated to 55 °C. The SnO_2 ETL was prepared at a 1:5 weight ratio of SnO_2 to DI H_2O and sonicated for 30 minutes.

ITO-coated glass was cut into 1.5 cm by 1.5 cm slides and sonicated in a mixture of isopropyl alcohol, ethanol, and DI water for 30 minutes. Kapton tape was used to mask a portion of the slide and the substrates were treated with O_2 plasma for 15 minutes. For samples that required an ETL, 50 μL of the SnO_2 solution was spin-coated at 2000 rpm with an acceleration of 1000 rpm/sec. These slides were annealed at 150 °C for one hour on a hot plate. The perovskite precursor solution and the Spiro-MeOTAD solutions were both filtered in preparation for spin-coating. The annealed slides were treated once more in O_2 plasma for 15 minutes, and then 30 μL of filtered precursor solution was spin-coated in a program that included 1000 rpm for 10 seconds, then 6000 rpm for 20 seconds. During this program, the anti-solvent 0.2 μL CB was added at the 24 second mark over the length of one second. The perovskite films were annealed at 100 °C for one hour after this. If a HTL was necessary for a sample, 30 μL of the Spiro-MeOTAD solution was spin-coated at 3000 rpm for 30 seconds. For the alternate HTL made of P3HT, the P3HT solution was filtered and 30 μL was spin-coated at 3000 rpm for 30 seconds. Kapton tape was removed

from the spin-coated slides in order to expose the ITO electrode for TENG testing. Many specimens of each type were synthesized for testing, including perovskite by itself, perovskite with an ETL, and perovskite with an ETL and HTL.

4.1.4.2 Characterization of $Cs_y(MA_{0.17}FA_{0.83})_{(1-y)}Pb(I_{0.83}Br_{0.17})_3$ Perovskite Thin Films

SEM images of the perovskite thin films and interfacial layers were taken using a Hitachi SU8010 SEM at 3.0 kV. Gold sputtering was performed before SEM imaging using a Quorum Q-150T ES sputterer. AFM characterization was performed using a Dimension FastScan by Bruker, Inc. UV-Vis spectra were obtained using a Hitachi U-3900 UV-Vis spectrophotometer. A Hitachi F-4600 fluorometer was used to measure the photoluminescence (PL) spectra. SEM images were processed using ImageJ software (National Institutes of Health, and the Laboratory for Optical and Computational Instrumentation at the University of Wisconsin). The AFM images were processed using Gwyddion software (David Nečas, Petr Klapetek) and Nanoscope Analysis software (Bruker).

4.1.4.3 Fabrication of Perovskite TENGs

The perovskite thin films on ITO glass substrates were treated as one triboelectric material in the TENG, and the other was composed of an acrylic substrate with a soft buffer layer of foam tape topped with a conductive copper tape electrode and a 200 μm-thick PTFE film. The purpose of the buffer layer is to improve contact area of the PTFE with perovskite since greater contact force may be applied using the linear motor. Copper wire was stripped down and attached to both the ITO electrode exposed on the perovskite thin film slides with copper tape, as well as the copper electrode underneath the PTFE layer. A

transparent acrylic backing was created in order to allow light to shine through to the perovskite and charge carrier transport layers.

4.1.4.4 TENG Device Measurements

The perovskite half of the TENG was affixed to a stationary XYZ linear translational stage (462-XYZ-M, Newport Inc.). The PTFE half of the TENG was attached to a programmable linear motor and the V_{OC} and I_{SC} were measured using a Keithley 6514 system electrometer. For photoelectric tests, TENG measurements were performed under illumination using a Newport 69911 Xe lamp without an AG filter (300 W).

CHAPTER 5. AZOPOLYMER IN TRIBOELECTRIC NANOGENERATORS

5.1 Effects of Light Responsiveness on Azobenzene-Containing Polymer Patterns and Self-Assembled Surfaces in Triboelectric Nanogenerators

5.1.1 Introduction

Functional polymers possess unique physical and chemical properties with which a great deal of novel applications may be realized. The –N=N– linkage is commonly termed an azo group or a diazene by systematic nomenclature. Polymers that contain aromatic azo moieties will be referred to as azo polymers from here on forward. Azo polymers contain two or more aromatic rings linked by one or several azo linkages, and show strong light absorption in the UV and visible ranges depending on the functional groups in the azo moieties, where photons can excite electrons from occupied low-energy orbitals to high-energy orbitals of the aromatic core.[173, 174] These excited electrons can cause variations in energy and structure of the molecules in a material. In particular, the azo functional group can exist in two configurations – the *trans* (E) form and the *cis* (Z) form, and switching between these isomers is termed *trans-cis* isomerization.[175] The decrease in the distance of para carbon atoms from 10 to 6 Å generates a significant nanoscale force[176, 177] that may induce further macroscopic photoactuation. This isomerization may be triggered by light irradiation and heat, producing hierarchical structure and property variations of azo polymers.[178] This molecular transformation is key to engineering a wide spectrum of applications, such as photofluidization lithography,[179] rewritable holograms,[180] and photonic elements such as diffraction gratings, microlens arrays, plasmonic sensors, and antireflection coatings.[181]

Of particular interest to our research are azobenzene containing polymers, where two benzene rings are linked by an azo group,[182-185] which are capable of converting isotropic structures to anisotropic structures through a directional mass-migration effect from linearly polarized light (LPL) irradiation.[186-190] Microparticles or arrays of micro/nano structures may be elongated along the polarization direction through reconfiguration of azobenzene units and photofluidization, allowing for precise manipulation of nanoscale elements with good repeatability and throughput.[191-194] The combination of *trans*-to-*cis* isomerization and *cis*-to-*trans* back isomerization gradually increases the number of azobenzene moieties with their transition moments perpendicular to the LPL polarization direction, which is termed the Weigert effect, and is unique to azobenzene-containing polymers.[195] This produces a macroscopic elongation of polymer structures and may change the surface area and morphological qualities of a material. Polymer networks that contain azobenzene liquid-crystal moieties can even change their macroscopic shape by photoisomerization, producing rapid photomechanical responses to Ar laser radiation and visible light in materials that are as thick as 320 μm.[196-202] A related study from our group in 2018 harnessed flow-enabled self-assembly in order to create photoswitchable liquid crystal azobenzene-containing polymer stripes on a glass substrate.[203] The hierarchical pattern was able to produce sequential reversible phase transitions due to the differences in thickness between the primary and secondary stripes under UV light. Photoexpansion of the stripes by 4% was observed due to *trans*-to-*cis* UV photoisomerization, and was partially recovered after visible light irradiation. Interestingly, another study found that covalently bound azobenzene units on a polymer backbone resulted in elongation of square pillars in the direction of the LPL, while non-covalently ionic bound azobenzene units resulted in their elongation perpendicular to the LPL direction.[204] Azobenzene polymers as functional materials have attracted a great deal of interest in recent decades due to the uniqueness and strength of the large scale material effects from small scale molecular changes.

Our research takes advantage of these morphological changes of azobenzene polymers through photofluidization, which can tune the wettability, surface area, and structural properties of patterned surfaces and particles. We have selected an azobenzene polymer, poly[6-(4-methoxy-4′-oxyazobenzene)hexyl methacrylate] (PAzoMA), which is a homopolymer with an azobenzene moiety in the side chain. This polymer has been widely integrated in amphiphilic graft block copolymer forms and on its own to form smart light-responsive material systems.[205-211] Herein, in order to investigate the effects of photoisomerized morphological changes on triboelectric energy harvesting, we seek to use facile methods to create distinct PAzoMA patterns that may exhibit obvious physical modification by mass migration. The breath figure method is traditionally used to fabricate ordered porous microstructured surfaces through the effects of atmospheric condensation and solvent evaporation.[212-216] The conventional breath figure process involves casting a drop of polymer solution onto a solid substrate and allowing it to evaporate in a humid environment.[217] We utilize the static breath figure method (**Figure 51a**), where solvent evaporation is completed spontaneously without aid of a gas flow.[218] Firstly, the humid environment inside a sealed vessel is established by prolonged containment of the desired atmosphere solvent, be it methanol, ethanol, or H_2O. The polymer solution is drop cast onto a glass substrate and allowed to evaporate, while atmosphere droplets condense onto the solution surface due to evaporative cooling (**Figure 51b-c**).[213] These droplets grow in size and sink into the solution partially due to Marangoni convection and thermocapillary effects,[219, 220] forming an array of porous structures on the completely evaporated solution/atmosphere layer (**Figure 51d-e**). The facile fabrication of breath figures opens up the possibility of precise manipulation of structure morphologies for a variety of applications including optical/optoelectronic devices,[221-223] templates,[224-227] micropatterning of biological molecules,[228-230] and sensors.[231-233]

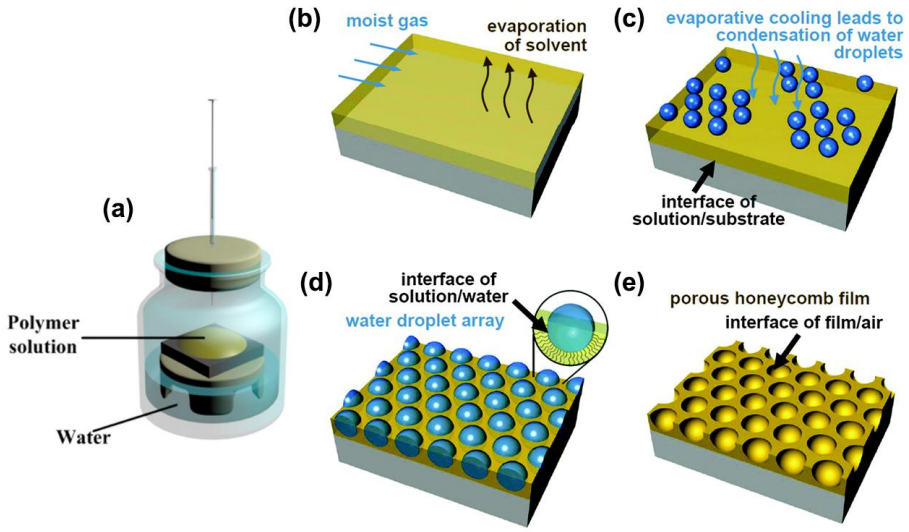

Figure 51. Conventional static breath figure method and mechanism. (a) Static breath figure setup schematic. Reproduced with permission.[215] Copyright 2015, American Chemical Society. (b-e) Model of mechanism for formation of honeycomb films by the breath figure method. Reproduced with permission.[213] Copyright 2014, Royal Society of Chemistry.

One study from our group in 2018 presented shape-memory polymers that are fabricated by the breath figure approach, with vapor crosslinking and LPL manipulation.[234] The ordered honeycomb porous films formed from a diblock copolymer of poly(4-vinylpyridine) (P4VP)-*block* –PazoMA were able to be converted from spherical pores to a variety of shapes, including rectangles, rhombi, and shrunken spherical micropores, all at room temperature. It has been documented that ordered PAzoMA microstructures other than pores may be realized through the reverse breath figure method, which involves concentration, solvent (**Figure 52a-d**), and atmosphere (**Figure 52e-g**) tuning, to produce a variety of different polymer material forms.[235] Gao et al. found that the optimal conditions to form ordered, uniform microspheres is to cast 5 mg mL^{-1} PAzoMA in $CHCl_3$ solution on a glass slide under an atmosphere of ethanol. The formation of microspheres over honeycomb films is thought to be brought about not by the vapor pressure of the solvent/atmosphere, but more likely by the surface tension of the polymer solution and condensed atmosphere droplets.[236] These microstructures, being composed of an

azobenzene-containing polymer, can be readily modified by their photoinduced *trans*-to-*cis* isomerization. Under LPL illumination of 3 hours, they were able to observe a microsphere aspect ratio of 1.79, and after 12 hours, the microstructures had elongated a great deal more, reaching an aspect ratio of 2.89 (**Figure 52h-i**). This was due to the elongation of the microspheres in the polarization direction, and this effect may be observed in a variety of other microstructures.[190, 192-194] Through this method, they were able to tune the wettability of the surface to a contact angle that was 12° higher. In this way, we can also fabricate functional, photoresponsive surfaces that may be easily modified to fit our needs.

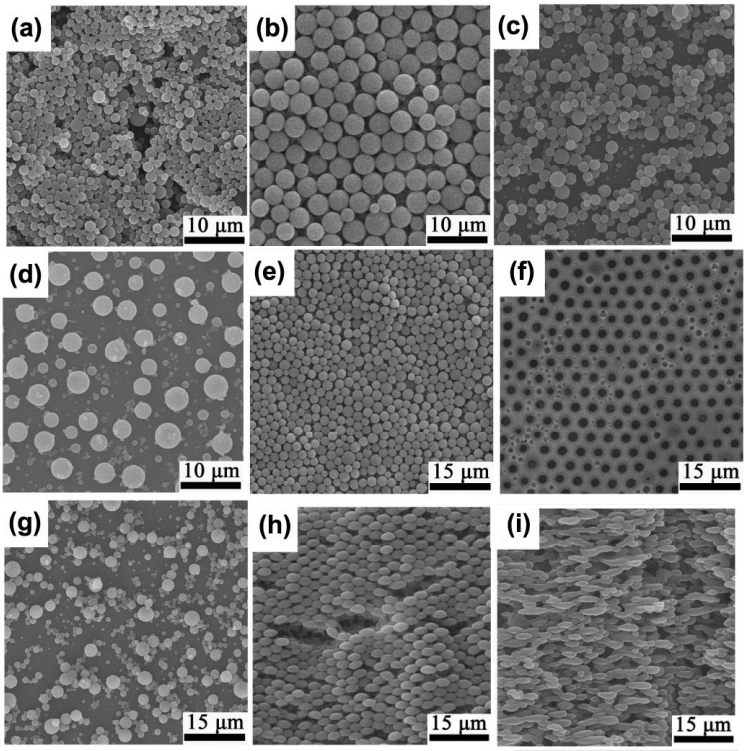

Figure 52. Varieties of microstructures produced by the breath figure method. Microspheres formed from reverse breath figure method with PAzoMA solution in (a) CH_2Cl_2, (b) $CHCL_3$, (c) THF, and (d) CS_2. Breath figures formed from PAzoMA under atmospheres of (e) ethanol, (f) water, and (g) methanol. Microspheres after blue LPL irradiation for (h) 3 hours and (i) 12 hours. Reproduced with permission.[235] Copyright 2018, American Chemical Society.

Improving the surface charge density of a TENG involves increasing surface area,[237] and elongation of microstructures on a TENG substrate would effectively do so. Herein, microspheres self-assembled by a reverse breath figure method[236, 238, 239] are subject to blue light-emitting diode (LED) LPL irradiation and the physical characteristics and TENG electrical output are characterized. While using a 450 nm LED light source at varying intensities and irradiation periods, we predict to see microspheres exhibiting greater degrees of expansion in the polarization direction under higher intensities and longer times. By not replacing or changing the material, but simply altering the surface morphology, we suggest that the electrical output of elongated PAzoMA microsphere arrays will be higher due to a greater amount of surface charges and surface contact area.

5.1.2 Results and Discussion

5.1.2.1 Characterization of PAzoMA Polymer

The PAzoMA polymer was supplied as synthesized by colleagues, and its chemical composition was characterized by ^{1}H NMR spectra as shown in **Figure 53**. The peaks at 7.72 and 7.66 are attributed to protons of the phenyl groups, and the peaks at 3.85 and 3.82 are attributed to the methylene and methoxyl groups, respectively. Peaks at 1.46 and 1.38 can be correlated to the methylene groups and methyl groups, and solvent peaks are labelled as well. This suggests that the PAzoMA sample does not have other functional groups that deviate from its implied chemical composition. The 1H NMR spectra matches that of literature on PAzoMA-containing compounds as well.[208, 240, 241]

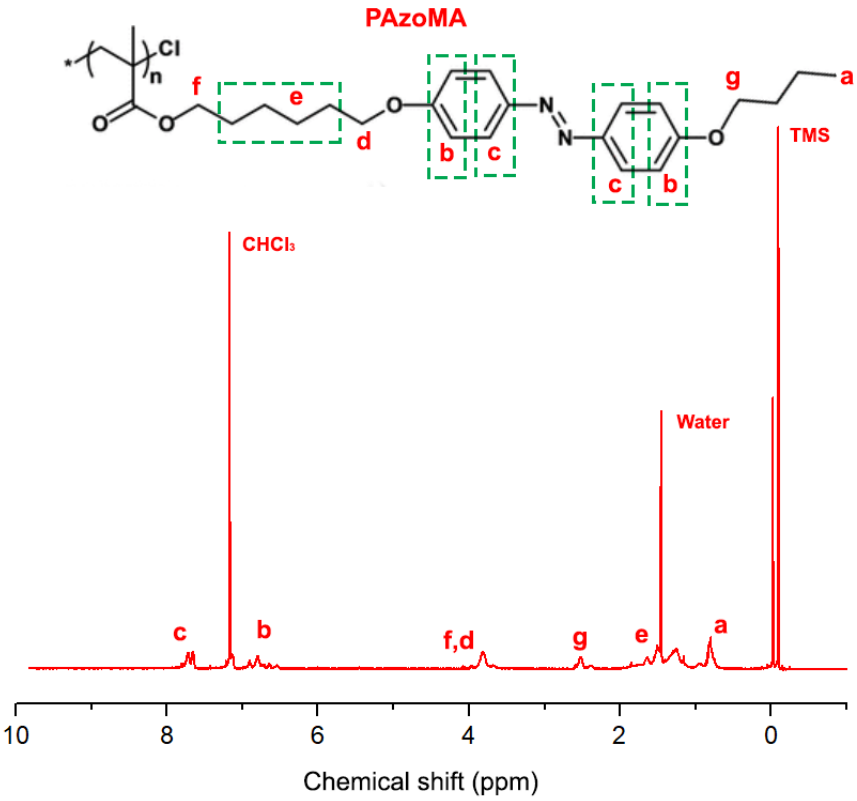

Figure 53. ^{1}H NMR spectra of linear homopolymer PAzoMA and corresponding hydrocarbon peak identities.

Gel permeation chromatography (GPC) measurements of PAzoMA were performed to investigate molecular weight characteristics, as shown in **Figure 54**. From spectra analysis, the number-average molecular weight (M_n) is 17.3 x 10^3 g mol^{-1} and the molecular weight distribution or polydispersity index (M_w/M_n) is 1.13. The polydispersity index value is below 1.2, or monodispersity, indicating that PAzoMA was synthesized with well controlled and consistent chain lengths. The lower molecular weight for a polymer corresponds well with the identity of PAzoMA as a linear homopolymer.

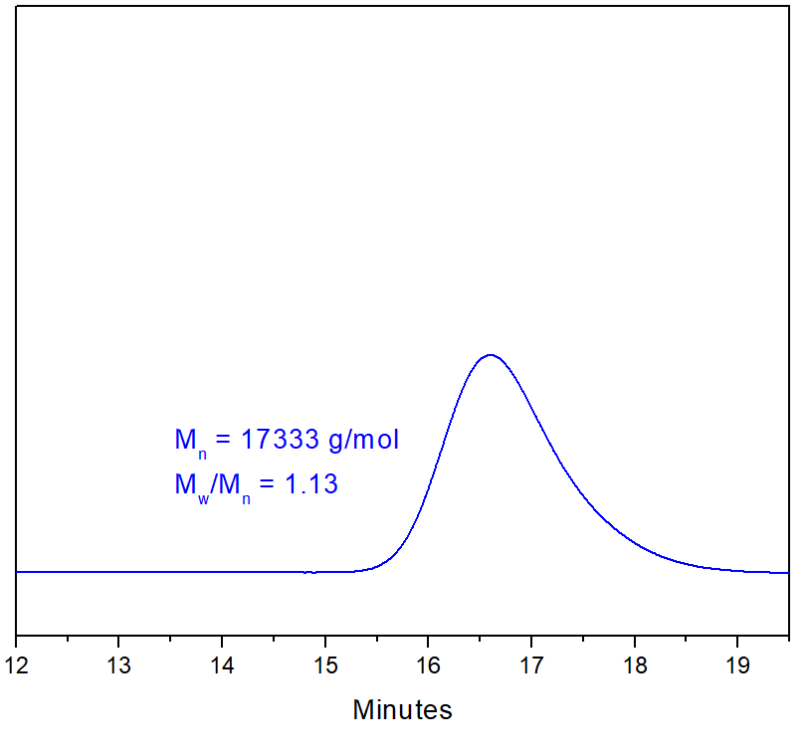

Figure 54. GPC traces of PAzoMA.

Since PAzoMA was synthesized using atomic transfer radical polymerization (ATRP), which allows for well-defined polymers with low PDI values.[242] The technique can also be used to produce block copolymers that also undergo photoisomerization due to azobenzene moieties, such as P4VP-*b*-PAzoMA[243] and poly(acrylic acid) (PAA)-*b*-PAzoMA-*b*-poly(*N*-isopropylacrylamide).[209] This shows the versatility of azobenzene-containing polymers in being highly functional and stimuli responsive regardless of other functional groups. However, some molecular modifications may be required in order to achieve photoactuation of greater magnitude or speed. For instance, photopolymerizing certain azobenzene monomers to form a liquid crystal network and using nematic cells to

create freestanding films produced photodriven actuators capable of rapid oscillating displacement.[244]

5.1.2.2 Irradiation of PAzoMA Microspheres by Reverse Breath Figure Method

Self-assembly of functional materials allows for unprecedented surface modification techniques that are both facile and effective. One-step patterning using a light responsive polymer offers a promising technique to improving the performance of TENGs that is scalable and easily modulated with simple experimental changes. Microspheres were fabricated using a reverse breath figure method with a solution of 5 mg mL^{-1} PAzoMA in chloroform, with ethanol as the atmosphere nonsolvent.[236] This method was carried out on ITO-coated glass substrates that were 1.5 x 1.5 cm, and formed uniform layers of microspheres as seen in **Figure 55a**. If the solvent and atmosphere were adjusted, it would be possible to create a variety of microstructures, including ordered porous arrays.[216] For our purposes, microspheres are ideal for modifying TENGs because they, similar to nanoparticles,[245] provide an increase in surface contact area as well as functionality. Due to the photoresponsive capabilities of azobenzene polymers, the dimensions of these microspheres are able to be modulated by using LPL to induce photoisomerization and mass migration in the direction of the light polarization. Herein, we used a blue LED with a linearly polarized filter to manipulate these microstructures into elongation, as shown in **Figure 55b-g**. Multiple intensities of LED light were tested at varying irradiation times in order to find the best suited modification technique for fabricating light responsive polymer TENGs. Using a 300 mW cm^{-2} LPL produced elongation that was visible under an optical microscope (**Figure 55e**), particularly after 3 hours of exposure. The PAzoMA microspheres that were irradiated by 600 mW cm^{-2} (**Figure 55c and 56f**) and 900 mW cm^{-}

^{2} (**Figure 55d and 56g)** showed even more intriguing architectures under the optical microscope**,** exhibiting obvious elongation in the polarization direction and morphological changes from photoisomerization. It may be observed that the microsphere layers had much fewer visible gaps when irradiated for longer periods of time at higher LED power, as seen in **Figure 55f-g**. This may be due to the high intensity of the light causing some shifting or settling of the polymer microstructures, and is investigated further using a higher resolution imaging technique.

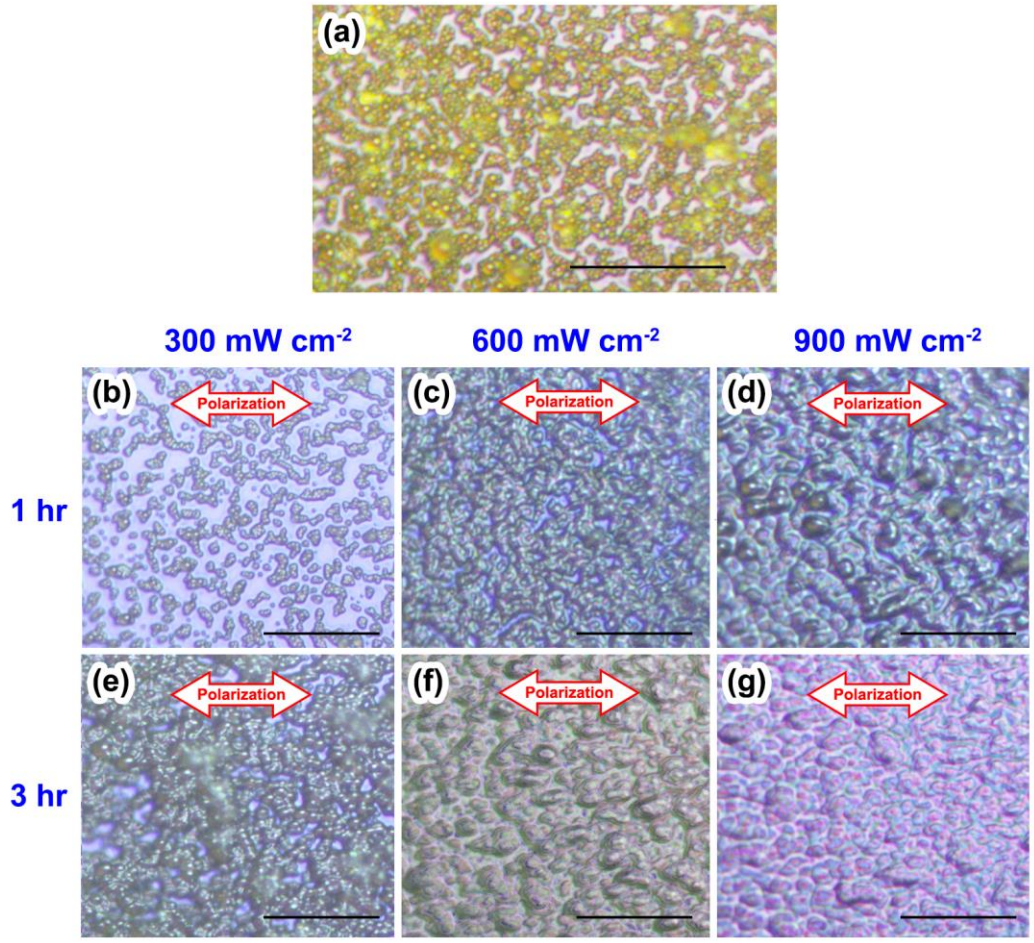

Figure 55. Optical microscope images of PAzoMA microspheres before and after irradiation under blue LPL at various intensities and times. (a) Original microspheres before irradiation. (b) After one hour irradiation at 300 mW cm^{-2}, (c) 600 mW cm^{-2}, and

(d) 900 mW cm^{-2}. (e) After three hour irradiation at 300 mW cm^{-2}, (f) 600 mW cm^{-2}, and (g) 900 mW cm^{-2}. Polarization direction of LPL indicated by red arrow. Scale bars indicate 20 μm (a-g).

PAzoMA is not a highly conductive polymer, so Au was deposited on the surface of the microspheres before SEM imaging. The images were taken following TENG testing, so further characterization done pre-TENG testing should be carried out in future work. The spherical form of the PAzoMA microspheres is plainly visible in **Figure 56a**, and polarization along the LPL direction may be observed for the samples irradiated by 300 mW cm^{-2} (**Figure 56b and 57e**) and 600 mW cm^{-2} (**Figure 56c and 57f**) blue LED light. The variation in microsphere size appears to be a result of experimental factors from the reverse breath figure method, so these should be carefully controlled as well. As for microspheres irradiated by the highest power intensity LED of 900 mW cm^{-2} (**Figure 56d and 57g**), it appears as though the robustness of these microstructures was decreased through light treatment. The highest intensity treatment resulted in the sample being compacted into a solid layer of PAzoMA instead of maintaining the microsphere shapes even following TENG operation as the other intensity treatments did. However, there exists some visible surface roughness on the compacted film, but this in effect negates the positive effects of light irradiation on microsphere dimensions. Therefore, in subsequent modifications of PAzoMA microstructures, the power of light irradiation should be moderated below 900 mW cm^{-2} in order to preserve their intricate geometries. As for the optimal LPL irradiation power and time to produce an ideal triboelectric material surface, further analysis of these images is carried out.

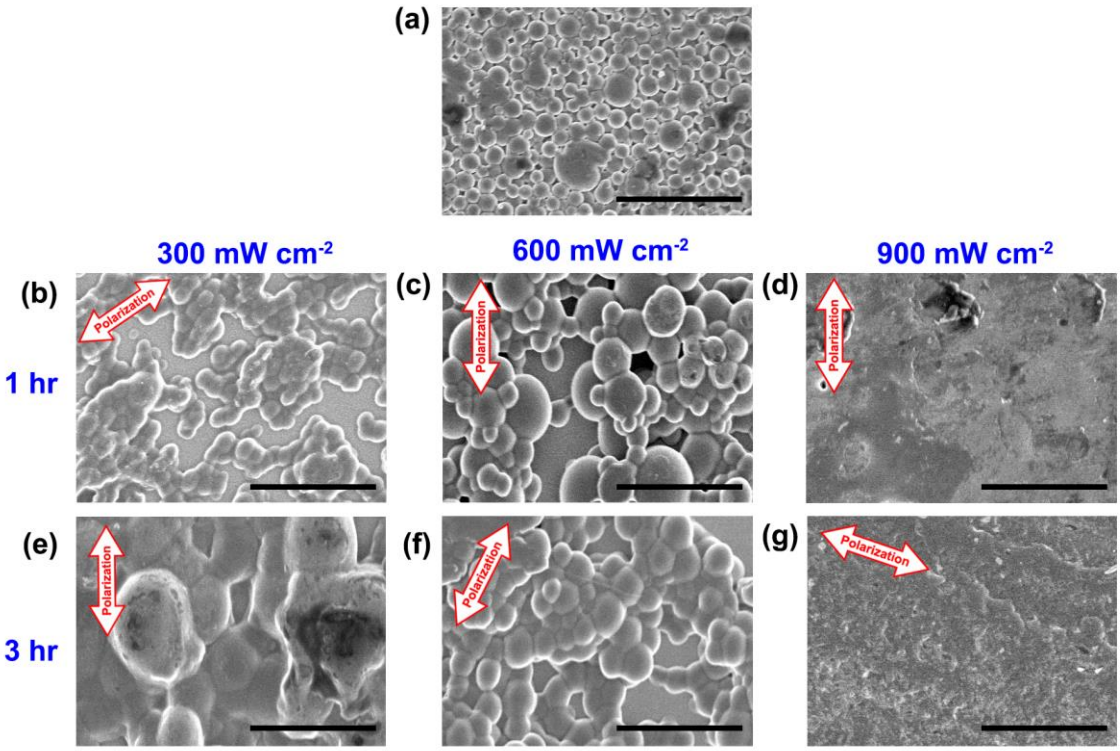

Figure 56. SEM images of PAzoMA microspheres before and after irradiation under blue LPL at various intensities and times and TENG operation. Specimens were coated in Au to improve SEM imaging resolution. (a) Original microspheres before irradiation. (b) After TENG operation following one hour irradiation at 300 mW cm^{-2}, (c) 600 mW cm^{-2}, and (d) 900 mW cm^{-2}. (e) After TENG operation following three hour irradiation at 300 mW cm^{-2}, (f) 600 mW cm^{-2}, and (g) 900 mW cm^{-2}. Polarization direction of LPL indicated by red arrow. Scale bars indicate 5 μm (a-g).

The aspect ratios of the PAzoMA microspheres were calculated using ImageJ software by measuring their lengths in the direction parallel to the LPL polarization direction, and dividing those by their lengths perpendicular to the polarization direction. Since the microstructures under 900 mW cm^{-2} irradiation were compacted into a film following TENG operation, the aspect ratio analysis for these samples was performed using the optical microscope images taken pre-TENG operation. The average values of those aspect ratios are listed in **Table 4**.

Table 4. Average aspect ratio of PAzoMA microspheres following blue LPL irradiation.

Light Intensity (mW cm^{-2})	Irradiation Time (hr)	Average Aspect Ratio (Parallel to Polarization over Perpendicular)
0	0	1.03
300	1	1.44
300	3	1.52
600	1	1.28
600	3	1.49
900	1	1.29
900	3	1.50

It may be observed that the greatest degree of robust photoinduced elongation was produced under three hours of irradiation at 300 mW cm^{-2}. In fact, irradiation at a lower power intensity (300 mW cm^{-2}) produced more distinct elongation overall compared to treatment at double the intensity. This may be due to the melting of the azo polymer at high light intensities, resulting in the sphere morphology being more difficult to maintain. Therefore, the photoinduced aspect ratio increase is not as pronounced in the higher intensity treatments. The microspheres irradiated under 900 mW cm^{-2} LPL failed to produce robust microstructures, with structural failure following a short period of TENG testing, showing that this condition would not be suitable for improvement of PAzoMA TENG surfaces. In fact, highly different results have been observed in photodeformation experiments involving azobenzene polymer films, in which higher intensity-irradiated samples may have experienced photothermal effects and photobleaching, resulting in some possible crosslinking from the large quantity of energy absorbed and increase in temperature from high light irradiance.[246] The desired surface relief grating in that experiment was only achieved at lower power intensities of light. When a sphere of

constant volume has been elongated into an ellipsoid of uneven dimensions in different axes, the surface area increases (**Figure 57**).

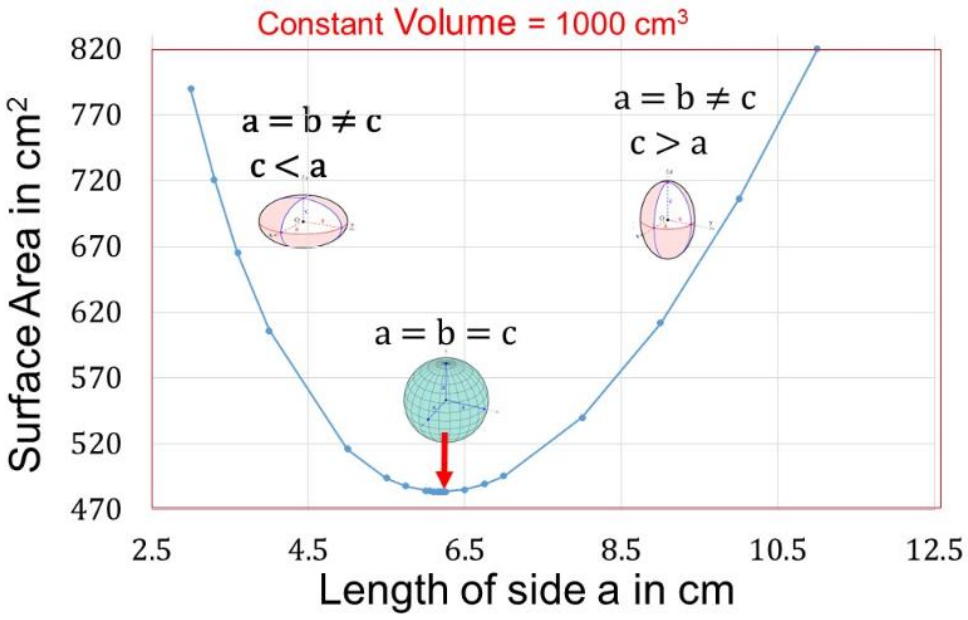

Figure 57. Variations in surface area when an ellipsoid's dimensions are altered. Reproduced with permission.[247]

Therefore, we may expect the photoisomerization of a microsphere layer to effectively increase the surface area available for contact with another triboelectric layer in a TENG. Surface modification has been an area of interest in TENG applications, and manipulating the geometry of a surface simply by using light irradiation could give rise to a scalable technique to fabricate light responsive TENGs for sensors and more.

5.1.2.3 TENG Electrical Output of PAzoMA Microsphere Layers

The LPL-treated microsphere-coated substrates were tested for their triboelectric charge generation capabilities in a TENG with PTFE as the opposing triboelectric layer. The results are plotted in **Figure 58a-c**, showing the V_{OC}, I_{SC}, and Q_{SC} signals from each

sample, with the average aspect ratios being exhibited in **Figure 58d** for comparison. Since the 300 mW cm^{-2} irradiation samples had a higher aspect ratio change post-treatment, the highest overall electrical output from the azopolymer-based TENGs resulted from using those samples. The V_{OC}, I_{SC}, and Q_{SC} were highest when using the microspheres illuminated by 300 mW cm^{-2} LPL for 3 hours, which resulted in an increase in aspect ratio along the polarization direction of 0.49. This most high performing microsphere sample achieved a 16% increase in V_{OC}, 20.8% increase in I_{SC}, and 10.7% increase in Q_{SC} over that of the original microspheres without LPL treatment.

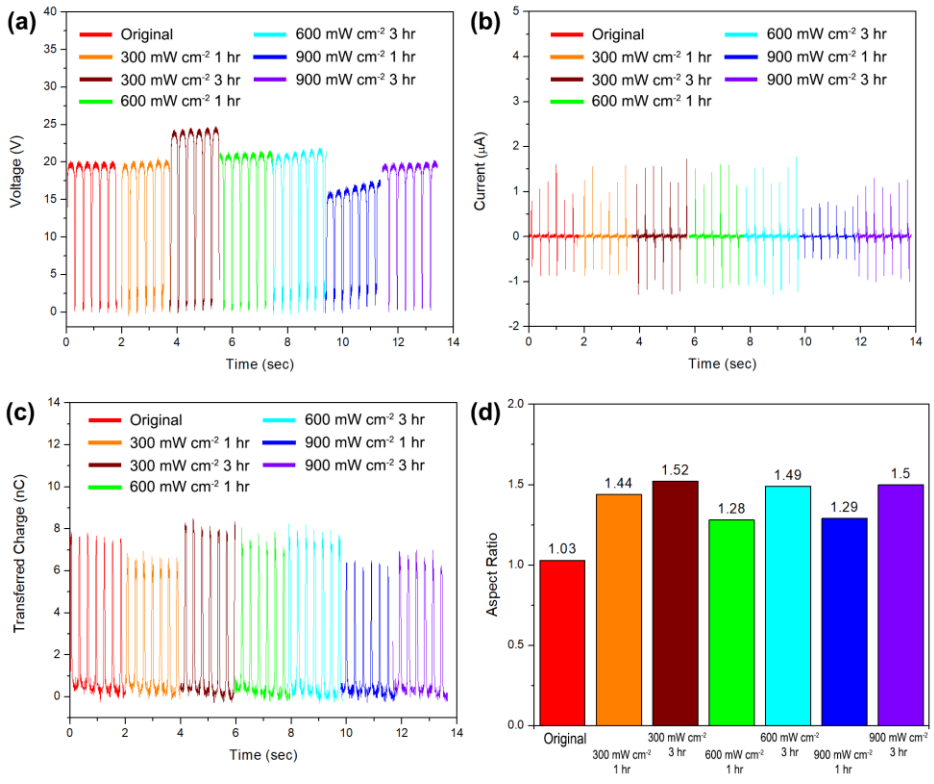

Figure 58. Performance of PAzoMA microsphere layers in a azopolymer-based TENG. (a) Open circuit voltage V_{OC}, (b) short circuit current I_{SC}, and (c) transferred charge Q_{SC} are all plotted for each LPL treatment condition. (d) Plot of aspect ratios of PAzoMA microspheres before and after varying intensities and times of LPL radiation.

Also of note is the fact that even though the LPL intensity was increased from 300 to 600 to 900 mW cm^{-2}, this did not promote the theorized increase in photoisomerization-induced elongation.[248] Perhaps this trend could be observed at lower intensities of light up to a threshold where PAzoMA starts to melt or become impacted by photothermal or photobleaching effects, and should be investigated using intensities of LPL like 100, 200, 400, and 500 mW cm^{-2}.

From the SEM images, it seems that the samples at 600 mW cm^{-2} were successfully elongated, albeit the physical size discrepancies between the microspheres may have resulted from an unknown variable in the breath figure process. The specimens irradiated at 600 mW cm^{-2} still showed a visible improvement in electrical output over the non-irradiated microspheres. The reason for the poorer electrical output performance of the samples irradiated at 900 mW cm^{-2} seems to be the compacting of the microsphere patterns into a solid layer following TENG testing. It appears from our results that using a LED of too high an intensity could lead to brittleness of the pattern. In this sense, further investigation into the effects of mass migration on the structural integrity of a material are needed.

5.1.3 Conclusion

Photoresponsive self-assembled structures have a great deal of potential in surface modification techniques for a variety of applications. In this study, we investigated their potential in improving the triboelectric charge generation of a microsphere layer formed from a reverse breath figure method using a photoactive azobenzene-containing polymer. PAzoMA was able to form microspheres that were successfully modified by using a 450

nm blue LED filtered by a linearly polarized lens to effectively induce photoisomerization of the azobenzene moieties. The longer the irradiation time, the greater the degree of photoinduced mass migration and elongation of microstructures along the polarization direction. When tested in a polymer TENG, the microspheres that were irradiated using 300 mW cm^{-2} light for 3 hours showed the greatest electrical output, and a general increase in charge generation was observed for samples of increasing light intensity and exposure time. This was correlated to the increasing aspect ratio of the microspheres above that of the original spherical dimensions, up until the samples that were modified using 900 mW cm^{-2} LPL. Using such a high intensity of light appeared to decrease the structural stability of these microsphere layers from the large quantity of energy being absorbed from the irradiance, resulting in the TENG frictional motion collapsing the microspheres and the material being compacted into a rough solid layer. Overall, more factors that may affect the surface morphology and physical properties should be investigated in developing this very new field of light-responsive mechanical energy harvesting materials, in order to fully harness their unique photo-induced qualities. Of particular interest would be to use azobenzene-containing polymers in liquid crystal networks with a wider range of motion and isomeric switching speed in order to create a fully light-driven energy harvesting device.

5.1.4 Experimental Section

PAzoMA was obtained as-synthesized from colleagues at Eastern China University of Science and Technology. Chloroform (≥99.8% stabilized), acetone (≥99.8%), and ethanol (absolute, KOPTEC) were purchased from VWR Chemicals BDH. Indium tin oxide (ITO)-coated glass and barium chloride dihydrate (≥99.999% trace metals basis)

were purchased from Sigma-Aldrich. TENG components, including 200 μm-thick PTFE film, Kapton tape, copper tape and wire, and 1/8 inch-thick acrylic sheets, were purchased from McMaster-Carr.

5.1.4.1 Fabrication of Microspheres by Reverse Breath Figure Method

ITO-covered glass was sectioned into 1.5 x 1.5 cm pieces and sonicated in a mixture of ethanol, acetone, and DI water for 30 minutes. Following this, the pieces were dried using N_2 gas and treated in O_2 plasma for 15 minutes. Kapton tape was used to cover a portion about 0.3 cm wide in order to expose the electrode for TENG testing later. In sealed glass bottles, a humid breath figure environment was maintained using a saturated $BaCl_2$ in ethanol solution. A static breath figure method was performed in these bottles by containing the ITO glass substrate for 30 minutes to recover the humid atmosphere, then aliquoting 50 μL of 5.0 mg mL^{-1} PAzoMA in chloroform solution on the surface of the substrates in the humid environment. The PAzoMA solution was allowed to fully evaporate the solvent for a period of 2 hours, and the substrates were removed and stored in a dark container before light irradiation experiments.

5.1.4.2 Blue LPL Irradiation and Characterization of PAzoMA Microspheres

An IUVOT High Intensity LED Spot Curing lamp was used for irradiation with a 450 nm blue LED attachment of a maximum light intensity of 1000 mW cm^{-2}. A linearly polarized lens was used to induce polarization of the LED light before reaching the irradiated sample. Photoisomerization experiments were carried out in an otherwise dark environment to minimize interference from other sources of light. Each PAzoMA microsphere specimen was subject to varying intensities of 450 nm LED light through the

LPL lens positioned in the same polarization direction, for varying amounts of time. Samples were immediately imaged using a Leica DM4000 M optical microscope and stored in a dark environment after the exposure time.

SEM images of the perovskite thin films and interfacial layers were taken using a Hitachi SU8010 SEM at 3.0 kV. Gold sputtering was performed before SEM imaging using a Quorum Q-150T ES sputterer. SEM images were processed using ImageJ software (National Institutes of Health, and the Laboratory for Optical and Computational Instrumentation at the University of Wisconsin).

5.1.4.3 Fabrication and Measurement of PAzoMA Microsphere-based TENGs

The microsphere layer on the ITO glass substrate was treated as one triboelectric material in the TENG, and the other was composed of an acrylic substrate with a soft buffer layer of foam tape topped with a conductive copper tape electrode and a 200 μm-thick PTFE film. The purpose of the buffer layer is to improve contact area of the PTFE with the microspheres since greater contact force may be applied using the linear motor. Copper wire was stripped down and attached to both the ITO electrode exposed on the perovskite thin film slides with copper tape, as well as the copper electrode underneath the PTFE layer. The PAzoMA half of the TENG was affixed to a stationary XYZ linear translational stage (462-XYZ-M, Newport Inc.). The PTFE half of the TENG was attached to a programmable linear motor and the V_{OC}, I_{SC}, and Q_{SC} were measured using a Keithley 6514 system electrometer.

CHAPTER 6. CONCLUSIONS AND OUTLOOK

6.1 Conclusions

Through our research, we have unraveled the underlying mechanisms of CE using high temperature resistant TENGs. We have correlated the exponential decay trends of surface charges on the contact-separation Ti-SiO_2 and Ti-Al_2O_3 TENGs in high temperatures to the model of thermionic emission of electrons. With this knowledge in hand, we have developed a surface states model for CE in metal-semiconductor pairs with clear energy levels and an electron cloud potential-well model for CE in metal-dielectric or dielectric-dielectric pairs, which could be extended to universal solid-solid CE. Electron cloud overlap was determined to be the driving force in electron transfer between materials, and even in identical materials, slight surface differences can affect surface states and instigate electron transfer. Also, since these studies were performed at temperatures where water would have boiled off and TENG charge transfer between these non-ionic materials still occurred, the theory of ion transfer does not hold as much weight in our models.

Investigating sliding mode Ti-SiO_2 TENGs at high temperature with a similar material setup resulted in an extension of those models for displacing surfaces compared to contacting and separating surfaces. The findings were that the sliding mode TENGs had a much longer time scale for complete charge emission in high temperature, and that as a whole they were more efficient in charge generation at these temperatures as well. In fact, they were even able to generate charges without any pre-charging of the SiO_2 substrates, which was essential for maintaining any charges in the contact-separation mode. This was suggested to be due to the shielding of the triboelectric surfaces from air breakdown and

thermionic emission through tight sliding contact. We determined that the model for the sliding mode TENG should be area-dependent, and when the displaced area is greater than the area in contact, thermionic emission has the potential to overtake the charge generation capabilities of the TENG. Overall, electron transfer being the dominant mechanism in CE between solids was disseminated from our results in these two studies.

Following our studies on thermionic emission and charge degradation on surfaces in high temperature, we developed a high temperature-resistant rotating TENG that was capable of generating and maintaining an appreciable level of charge even at 673 K. The rotating design integrates multiple sliding interactions at once and the grating pattern electrodes on the back of the encapsulating SiO_2 tube allow for displacement of the Ti foil from the electrodes at a high rate without compromising volume. Modifying factors such as increasing the rotational rate as well as constructing tightly contacting supports out of spring steel/Al foil and pre-annealing the supports resulted in a highly efficient R-TENG at extreme temperatures. By pre-annealing at higher temperatures, charge generation is even greater in extreme conditions (>600 K) due to thermal expansion of the Al sheet and contraction at room temperature, providing an extremely tight contact between the support, the Ti foil, and the SiO_2 tube interior. This design was able to achieve a peak power of 8 μW at 673 K, which is unprecedented for any other material system. Also, sources of rotary motion are more common in industrial settings than strong contact-separation motions, so this high temperature resistant R-TENG design is highly valuable for such environments.

With the potential of perovskite as a triboelectric material due to perovskite's unique dielectric properties and nanostructured surface, we investigated the effects of chemical precursor modulation on the surface morphology of $Cs_y(MA_{0.17}FA_{0.83})_{(1-}$

$_{y)}Pb(I_{0.83}Br_{0.17})_3$ thin films fabricated through a facile, one-step spin coating process. These films were robust, stable, and maintained the dark phase without degrading to a yellow δ phase. We found that by lowering the CsI molar ratio in the precursor solution to 0.02, we were still able to reap the benefits of cesium's thermal stability and dark phase maintenance, but also decrease the grain size and increase the RMS roughness of the perovskite thin film. This in turn produced the highest improvement in TENG output using these $Cs_y(MA_{0.17}FA_{0.83})_{(1-y)}Pb(I_{0.83}Br_{0.17})_3$ films, resulting in a 26.5% increase in V_{OC}, 24.4% increase in I_{SC}, and 17.5% increase in Q_{SC} over the lowest performing sample with a CsI molar ratio of 0.14. Additionally, a photoelectric test was performed using interfacial engineering to improve the effects of electron-hole separation from light irradiation and increase the surface charge density. A unique TENG triboelectric material design with $Cs_y(MA_{0.17}FA_{0.83})_{(1-y)}Pb(I_{0.83}Br_{0.17})_3$ paired with interfacial layers of SnO_2 and P3HT exhibited improved electrical output performance, particularly in V_{OC}, under solar simulator illumination compared to without. From our results, it can be suggested that perovskites paired with an ETL and HTL perform better than those without in hybrid photoelectric/triboelectric energy conversion.

Finally, we investigated the capabilities of light to impact the geometries of azobenzene-containing polymer microstructures and increase surface contact area. The physical properties of the surface would be change through photoisomerization of the azobenzene moieties in the polymers from *trans* to *cis*, resulting in mass migration and photofluidization of the polymer. Effective electrical output improvements were made on a PAzoMA microsphere-based TENG by using 450 nm blue LPL to irradiate said microspheres and produce elongations of up to an aspect ratio of 1.82 in the direction of

light polarization. These microspheres are an appealing form of surface modification since they only require a facile, one-step reverse breath figure process that can be easily scaled. It was found that irradiation at 300 mW cm^{-2} for 3 hours produced the greatest TENG output improvement over microspheres without light treatment, with a 16% increase in V_{OC}, 20.8% increase in I_{SC}, and 10.7% increase in Q_{SC}. When irradiated at higher intensities such as 600 and 900 mW cm^{-2}, the PAzoMA microstructures seem to have become less robust under such intense light treatment and the were even compacted into a solid layer after 900 mW cm^{-2} by a brief session of TENG testing. In the end, the optimal light treatment method of a self-assembled surface was determined through our research, and this could bring about a new subfield in nanogenerators for light-responsive materials.

6.2 Future Work

With the progress achieved in the research detailed in this thesis, we now have a great deal of progress in terms of the theory of CE and TENGs, as well as novel surface modification techniques for functional materials. The published studies in this thesis have paved the way for further investigation of CE theory, including studies on photon-excited emission of electrostatic charges to provide further evidence of electron transfer being the dominant mechanism in CE.[92] Also, we have performed studies involving identical materials and the effects of their surface curvatures on energy shifts in surface states and resulting CE between identical material surfaces.[249] Also, an intriguing study has taken place in recent months on solid-liquid CE, which shows that electron transfer may be the root of ion generation in an electric double layer, and that electrification could impact contact angle, which upends the entire study of goniometry.[250] Since CE is such a complex process with many variations and decades of study, we have only scratched the surface of

what is underlying this commonly experienced phenomenon. However, with TENGs as highly useful tools for studying these fundamental physics, we can expect to have a great deal more mechanistic studies on CE in the future.

Material surfaces have surface asperities and this influences how many points of electron cloud overlap and CE are possible from two surfaces in contact. Researchers in the field of tribology have found that many factors that influence the contact between surfaces, including nature and surface state of materials, ambient conditions, relative velocity of sliding, and contact pressure.[251] The density of charge transfer points is key to increasing electrical output of a TENG according to the Volta-Helmholtz hypothesis. As two surfaces are brought in contact, nanoscale asperities are the first points of contact, instantly deforming plastically and merging to create micro/nanostructures.[252] Each solid surface contains layers upon layers of these asperities, so the sliding interaction of triboloectric materials will result in a great deal of compaction and deformation occurring in order to oppose the applied load. Our model of CE would be able to be describe the constantly changing points of contact. A separate model has been proposed to describe the large gaps of contact with surface roughness due to restricted quantum tunneling of electrons or ions in such areas.[253] By scaling down hopping parameters of electrons between interfaces by a certain value α, the true surface area in solid-solid contact was more accurately modeled. In addition to the dielectric constant and electron population on atomic sites, hopping parameters between solid materials make up the quantum-mechanical model for studying CE that was proposed. In order to experimentally probe the true area of contact, exact methods to explore surface roughness and contact points should be considered. Methods to analyze individual points of contact have been performed using

AFM and KPFM techniques,[92, 94, 95, 113] but quantifying the entire range of contacting points across a surface would require careful and exact modulation of the surface roughness of both sides. KPFM may be used to map the surface charge mosaics of two contacting triboelectric material surfaces, and the differences in transferred charges after TENG operation may be quantified and used to further the model of CE between two solids.[51]

The film quality, consistency, and performance in increasing surface charge density of $Cs_y(MA_{0.17}FA_{0.83})_{(1-y)}Pb(I_{0.83}Br_{0.17})_3$ thin films could be worked on to further improve their hybrid photoelectric/triboelectric action in further experimentation. Also, more compositions of perovskite should be tested in order to broaden our knowledge of functional material-based TENGs. As shown by our results, novel methods for surface passivation for optoelectronic applications could be investigated as well as finding unexpected results from taking said methods too far, such as phase segregation. Additionally, probing of surface hardness by nanonindentation testing as well as crystallinity characterization by XRD could shed more light on the exact effects of Cs-moderated surface passivation on the integrity of the thin film. Also, the elongation performance of other intensities of LPL on PAzoMA microspheres should be tested for as well, since the one consensus that has been reached in existing literature has been that elongation increases with higher light power.[248] The material in our experiments appears to have experienced some weakening of mass migration due to the high intensity of light irradiance, bringing about possible photothermal and photobleaching effects. Therefore, testing the photoisomerization results on geometry over a lower range of light intensities could result in a trend of aspect ratios increasing with light power.

Developing theories on the underlying mechanisms of TENGs – CE and electrostatic induction – is key to improving the performance of TENGs for usage in applications as well. More commercially viable techniques to produce highly efficient, optimized, inexpensive TENGs are always sought after. Additionally, the understanding of functional materials and the factors that impact their performance in TENGs for sensors, energy harvesting, etc. may be further improved on with even more testing. Not only is improving triboelectric materials testing hybrid energy harvesting capabilities important to device development, but also it is imperative to investigate ideal methods of energy storage and power system integration to fully harness our target sources of mechanical energy. Using flexible, soft materials appears to help conform TENGs to biomechanical and natural sources of motion the most, so research in this area has continued to expand in recent years. Active sensing is an appealing trait of functional material TENGs as well, so we may use stimuli-responsive materials to improve on these applications. In the next decade, we may expect TENGs to begin having an important role in commercial products due to their portability, sustainability, ease of fabrication, and unique capabilities.

PUBLICATIONS

Google Scholar: https://scholar.google.com/citations?user=r-oC7bYAAAAJ&hl=en

Total citation **2340**; h index **24**

1. **Wang, A. C.**; Zhang, B.; Xu, C.; Zou, H.; Wang, Z. L., Unraveling Temperature-Dependent Contact Electrification between Sliding-Mode Triboelectric Pairs. *Advanced Functional Materials* **2020**, *30* (12), 1909384.

2. **Wang, A. C.**; Wu, C.; Pisignano, D.; Wang, Z. L.; Persano, L., Polymer nanogenerators: Opportunities and challenges for large-scale applications. *Journal of Applied Polymer Science* **2018,** *135* (24), 45674.

3. Xu*, C.; **Wang*, A. C.** (co-first author); Zou, H.; Zhang, B.; Zhang, C.; Zi, Y.; Pan, L.; Wang, P.; Feng, P.; Lin, Z., Raising the Working Temperature of a Triboelectric Nanogenerator by Quenching Down Electron Thermionic Emission in Contact-Electrification. *Advanced Materials* **2018,** *30* (38), 1803968.

4. Xu*, C.; Zi, Y.; **Wang*, A. C.**(co-first author); Zou, H.; Dai, Y.; He, X.; Wang, P.; Wang, Y. C.; Feng, P.; Li, D., On the Electron-Transfer Mechanism in the Contact-Electrification Effect. *Advanced Materials* **2018,** *30* (15), 1706790.

5. Xu*, C.; Zhang, B.; **Wang*, A. C.** (co-first author); Zou, H.; Liu, G.; Ding, W.; Wu, C.; Ma, M.; Feng, P.; Lin, Z.; Wang, Z. L., Contact-Electrification between Two Identical Materials: Curvature Effect. *ACS Nano* **2019,** *13* (2), 2034-2041.

6. Zou, H., Dai, H., **Wang, A. C**., Li, X., Zhang, S.L., Ding, W., Zhang, L., Zhang, Y., Wang, Z.L. "Alternating Current Photovoltaic Effect", *Adv. Mater*. **2020**, *32* (11), 1907249.

7. Pan, S.; Zou, H.; **Wang, A. C.**; Wang, Z.; Yu, J.; Lan, C.; Liu, Q.; Wang, Z. L.; Lian, T.; Peng, J.; Lin, Z. Rapid capillary-assisted solution printing of perovskite nanowire arrays enables scalable production of photodetectors, *Angew. Chem. Int. Ed. Engl.* **2020**, *59*, 2-10.

8. Qi, J.; **Wang, A. C.**; Yang, W.; Zhang, M.; Hou, C.; Zhang, Q.; Li, Y.; Wang, H., Hydrogel-based hierarchically wrinkled stretchable nanofibrous membrane for high performance wearable triboelectric nanogenerator. *Nano Energy* **2020,** *67*, 104206.

9. Cui, X.; Lei, S.; **Wang, A. C.**; Gao, L.; Zhang, Q.; Yang, Y.; Lin, Z. Emerging covalent organic frameworks tailored materials for electrocatalysts. *Nano Energy* **2020**, *70*, 104525.

10. Dong, J., Huang, J., **Wang, A.C.**, Biesold-McGee, G.V., Zhang, X., Gao, S., Wang, S., Lai, Y., Lin, Z., Vertically-aligned Pt-decorated MoS2 nanosheets coated on TiO2 nanotube arrays enable high-efficiency solar-light energy utilization for photocatalysis and self-cleaning SERS devices, *Nano Energy* **2020**, *71*, 104579.

11. Zhang, L., Qin, X., Zhao, S., **Wang, A.C.**, Luo, J., Wang, Z.L., Kang, F., Lin, Z., Li, B., Advanced Matrixes for Binder-Free Nanostructured Electrodes in Lithium-Ion Batteries, *Adv. Mater.* **2020**, 1908445.

12. Lin, Z., Pan, S., Zou, H., **Wang, A.C.**, Wang, Z., Yu, J., Lan, C., Liu, W., Wang, Z.L., Lian, T., Peng, J., Rapid Capillary-Assisted Solution Printing of Perovskite Nanowire Arrays Endables Scalable Production of Photodetectors, *Angew. Chem. Int. Ed*. **2020**, https://doi.org/10.1002/anie.202004912.

13. Lin, S.; Xu, L.; **Wang, A. C.**; Wang, Z. L., Quantifying electron-transfer in liquid-solid contact electrification and the formation of electric double-layer. *Nature Communications* **2020,** *11* (1), 1-8.

14. Dong, K.; Peng, X.; An, J.; **Wang, A. C.**; Luo, J.; Sun, B.; Wang, J.; Wang, Z. L. Shape adaptable and highly resilient 3D braided triboelectric nanogenerators as e-textiles for power and sensing, *Nature Commun.* **2020**, *11* (1), 1-11.

15. Ding, W.; **Wang, A. C.**; Wu, C.; Guo, H.; Wang, Z. L., Human–machine interfacing enabled by triboelectric nanogenerators and tribotronics. *Advanced Materials Technologies* **2019,** *4* (1), 1800487.

16. Wu, C.; **Wang, A. C.**; Ding, W.; Guo, H.; Wang, Z. L., Triboelectric nanogenerator: a foundation of the energy for the new era. *Advanced Energy Materials* **2019,** *9* (1), 1802906.

17. Xu, C.; Zhang, B.; **Wang, A. C.**; Cai, W.; Zi, Y.; Feng, P.; Wang, Z. L., Effects of Metal Work Function and Contact Potential Difference on Electron Thermionic Emission in Contact Electrification. *Advanced Functional Materials* **2019,** *29* (29), 1903142.

18. Zou, H.; Zhang, Y.; Guo, L.; Wang, P.; He, X.; Dai, G.; Zheng, H.; Chen, C.; **Wang, A. C.**; Xu, C.; Wang, Z. L., Quantifying the triboelectric series. *Nature Communications* **2019**, 10, 1427.

19. Wang, Z. L.; **Wang, A. C.**, On the origin of contact-electrification. *Materials Today* **2019**, 30, 34-51.

20. Lin, S.; Xu, L.; Xu, C.; Chen, X.; **Wang, A. C.**; Zhang, B.; Lin, P.; Yang, Y.; Zhao, H.; Wang, Z. L., Electron Transfer in Nanoscale Contact Electrification: Effect of Temperature in the Metal–Dielectric Case. *Advanced Materials* **2019,** *31* (17), 1808197.

21. Zou, H.; Li, X.; Dai, G.; Peng, W.; Ding, Y.; Zhang, Y.; **Wang, A. C.**; Zhang, S. L.; Xu, C.; Zhang, S.-L., Dramatically Enhanced Broadband Photodetection by Dual Inversion Layers and Fowler–Nordheim Tunneling. *ACS Nano* **2019,** *13* (2), 2289-2297.

22. Xu, C.; Zhang, B.; **Wang, A. C.**; Zou, H.; Liu, G.; Ding, W.; Wu, C.; Ma, M.; Feng, P.; Lin, Z., Contact-electrification between two identical materials: curvature effect. *ACS Nano* **2019,** *13* (2), 2034-2041.

23. Zou, H.; Zhang, Y.; Guo, L.; Wang, P.; He, X.; Dai, G.; Zheng, H.; Chen, C.; **Wang, A. C.**; Xu, C., Quantifying the triboelectric series. *Nature communications* **2019,** *10* (1), 1-9.

24. Qi, J.; Li, L.; Xiong, H.; **Wang, A. C.**; Hou, C.; Zhang, Q.; Li, Y.; Wang, H., Highly efficient walking perovskite solar cells based on thermomechanical polymer films. *Journal of Materials Chemistry A* **2019,** *7* (45), 26154-26161.

25. Luo, J.; Wang, Z.; Xu, L.; **Wang, A. C.**; Han, K.; Jiang, T.; Lai, Q.; Bai, Y.; Tang, W.; Fan, F. R., Flexible and durable wood-based triboelectric nanogenerators for self-powered sensing in athletic big data analytics. *Nature communications* **2019,** *10* (1), 1-9.

26. Zhao, L.; Li, H.; Meng, J.; **Wang, A. C.**; Tan, P.; Zou, Y.; Yuan, Z.; Lu, J.; Pan, C.; Fan, Y., Reversible Conversion between Schottky and Ohmic Contacts for Highly Sensitive, Multifunctional Biosensors. *Advanced Functional Materials* **2019**, 1907999.

27. Xu, M.; Wang, P.; Wang, Y. C.; Zhang, S. L.; **Wang, A. C.**; Zhang, C.; Wang, Z.; Pan, X.; Wang, Z. L., A soft and robust spring based triboelectric nanogenerator for harvesting arbitrary directional vibration energy and self-powered vibration sensing. *Advanced Energy Materials* **2018,** *8* (9), 1702432.

28. Jiang, Q.; Wu, C.; Wang, Z.; **Wang, A. C.**; He, J.-H.; Wang, Z. L.; Alshareef, H. N., MXene electrochemical microsupercapacitor integrated with triboelectric nanogenerator as a wearable self-charging power unit. *Nano Energy* **2018,** *45*, 266-272.

29. Li, X.; Li, B.; He, M.; Wang, W.; Wang, T.; **Wang, A.**; Yu, J.; Wang, Z.; Hong, S. W.; Byun, M., Convenient and robust route to photoswitchable hierarchical liquid crystal polymer stripes via flow-enabled self-assembly. *ACS applied materials & interfaces* **2018,** *10* (5), 4961-4970.

30. Liu, R.; Kuang, X.; Deng, J.; Wang, Y. C.; **Wang, A. C.**; Ding, W.; Lai, Y. C.; Chen, J.; Wang, P.; Lin, Z., Shape memory polymers for body motion energy harvesting and self-powered mechanosensing. *Advanced Materials* **2018,** *30* (8), 1705195.

31. Wang, W.; Shen, D.; Li, X.; Yao, Y.; Lin, J.; **Wang, A.**; Yu, J.; Wang, Z. L.; Hong, S. W.; Lin, Z., Light-Driven Shape-Memory Porous Films with Precisely Controlled Dimensions. *Angewandte Chemie International Edition* **2018,** *57* (8), 2139-2143.

32. Wu, C.; Ding, W.; Liu, R.; Wang, J.; **Wang, A. C.**; Wang, J.; Li, S.; Zi, Y.; Wang, Z. L., Keystroke dynamics enabled authentication and identification using triboelectric nanogenerator array. *Materials Today* **2018,** *21* (3), 216-222.

33. Deng, J.; Kuang, X.; Liu, R.; Ding, W.; **Wang, A. C.**; Lai, Y. C.; Dong, K.; Wen, Z.; Wang, Y.; Wang, L., Vitrimer elastomer-based jigsaw puzzle-like healable triboelectric nanogenerator for self-powered wearable electronics. *Advanced Materials* **2018,** *30* (14), 1705918.

34. Wang, Z. L.; **Wang, A. C.** In *Triboelectric nanogenerator for self-powered flexible electronics and Internet of Things*, Meeting Abstracts, The Electrochemical Society: 2018; pp 1533-1533.

35. Ding, W.; Wu, C.; Zi, Y.; Zou, H.; Wang, J.; Cheng, J.; **Wang, A. C.**; Wang, Z. L., Self-powered wireless optical transmission of mechanical agitation signals. *Nano Energy* **2018,** *47*, 566-572.

36. Dong, K.; Deng, J.; Ding, W.; **Wang, A. C.**; Wang, P.; Cheng, C.; Wang, Y. C.; Jin, L.; Gu, B.; Sun, B., Versatile core–sheath yarn for sustainable biomechanical energy harvesting and real-time human-interactive sensing. *Advanced Energy Materials* **2018,** *8* (23), 1801114.

37. Dong, K.; Wu, Z.; Deng, J.; **Wang, A. C.**; Zou, H.; Chen, C.; Hu, D.; Gu, B.; Sun, B.; Wang, Z. L., A stretchable yarn embedded triboelectric nanogenerator as electronic skin for biomechanical energy harvesting and multifunctional pressure sensing. *Advanced Materials* **2018,** *30* (43), 1804944.

38. Wang, J.; Wu, C.; Dai, Y.; Zhao, Z.; **Wang, A.**; Zhang, T.; Wang, Z. L., Achieving ultrahigh triboelectric charge density for efficient energy harvesting. *Nature Communications* **2017,** *8* (1), 88.

39. Peng, W.; Wang, X.; Yu, R.; Dai, Y.; Zou, H.; **Wang, A. C.**; He, Y.; Wang, Z. L., Enhanced Performance of a Self-Powered Organic/Inorganic Photodetector by Pyro-Phototronic and Piezo-Phototronic Effects. *Advanced Materials* **2017,** *29* (23), 1606698.

40. Wang, J.; Wu, C.; Dai, Y.; Zhao, Z.; **Wang, A.**; Zhang, T.; Wang, Z. L., Achieving ultrahigh triboelectric charge density for efficient energy harvesting. *Nature communications* **2017,** *8* (1), 1-8.

41. Zhu, G.; **Wang, A. C.**; Liu, Y.; Zhou, Y.; Wang, Z. L., Functional electrical stimulation by nanogenerator with 58 V output voltage. *Nano letters* **2012,** *12* (6), 3086-3090.

42. Li, Z.; Zhu, G.; Yang, R.; **Wang, A. C.**; Wang, Z. L., Muscle-driven in vivo nanogenerator. *Advanced materials* **2010,** *22* (23), 2534-2537.

43. Ding, Y.; Xu, S.; Zhang, Y.; **Wang, A. C.**; Wang, M. H.; Xiu, Y.; Wong, C. P.; Wang, Z. L., Modifying the anti-wetting property of butterfly wings and water strider legs by atomic layer deposition coating: surface materials versus geometry. *Nanotechnology* **2008,** *19* (35), 355708.

REFERENCES

1. Service, R. F., Solar energy. Is it time to shoot for the sun? *Science* **2005,** *309* (5734), 548-51.

2. Fan, F.-R.; Tian, Z.-Q.; Lin Wang, Z., Flexible triboelectric generator. *Nano Energy* **2012,** *1*, 328-334.

3. Wang, Z. L., Triboelectric nanogenerators as new energy technology and self-powered sensors – Principles, problems and perspectives. *Faraday Discussions* **2014,** *176* (0), 447-458.

4. Wang, Z. L., On Maxwell's displacement current for energy and sensors: the origin of nanogenerators. In *Materials Today*, 2017.

5. Niu, S.; Liu, Y.; Wang, S.; Lin, L.; Zhou, Y. S.; Hu, Y.; Wang, Z. L., Theoretical Investigation and Structural Optimization of Single-Electrode Triboelectric Nanogenerators. *Advanced Functional Materials* **2014,** *24* (22), 3332-3340.

6. Niu, S.; Wang, S.; Lin, L.; Liu, Y.; Zhou, Y. S.; Hu, Y.; Wang, Z. L., Theoretical study of contact-mode triboelectric nanogenerators as an effective power source. *Energy & Environmental Science* **2013,** *6* (12), 3576-3583.

7. Niu, S.; Liu, Y.; Wang, S.; Lin, L.; Zhou, Y. S.; Hu, Y.; Wang, Z. L., Theory of Sliding-Mode Triboelectric Nanogenerators. *Advanced Materials* **2013,** *25* (43), 6184-6193.

8. Niu, S.; Liu, Y.; Chen, X.; Wang, S.; Zhou, Y. S.; Lin, L.; Xie, Y.; Wang, Z. L., Theory of freestanding triboelectric-layer-based nanogenerators. *Nano Energy* **2015,** *12*, 760-774.

9. Zi, Y.; Niu, S.; Wang, J.; Wen, Z.; Tang, W.; Wang, Z. L., Standards and figure-of-merits for quantifying the performance of triboelectric nanogenerators. *Nature Communications* **2015,** *6*, 8376.

10. Yang, B.; Zeng, W.; Peng, Z.-H.; Liu, S.-R.; Chen, K.; Tao, X.-M., A Fully Verified Theoretical Analysis of Contact-Mode Triboelectric Nanogenerators as a Wearable Power Source. *Advanced Energy Materials* **2016,** *6* (16), 1600505.

11. Fu, J.; Xia, X.; Xu, G.; Li, X.; Zi, Y., On the Maximal Output Energy Density of Nanogenerators. *ACS Nano* **2019,** *13* (11), 13257-13263.

12. Wang, Z. L.; Wang, A. C., On the origin of contact-electrification. *Materials Today* **2019**.

13. Wang, S.; Mu, X.; Wang, X.; Gu, A. Y.; Wang, Z. L.; Yang, Y., Elasto-Aerodynamics-Driven Triboelectric Nanogenerator for Scavenging Air-Flow Energy. *ACS Nano* **2015,** *9* (10), 9554-9563.

14. Zhao, Z.; Pu, X.; Du, C.; Li, L.; Jiang, C.; Hu, W.; Wang, Z. L., Freestanding Flag-Type Triboelectric Nanogenerator for Harvesting High-Altitude Wind Energy from Arbitrary Directions. *ACS Nano* **2016,** *10* (2), 1780-1787.

15. Xie, Y.; Wang, S.; Niu, S.; Lin, L.; Jing, Q.; Yang, J.; Wu, Z.; Wang, Z. L., Grating-Structured Freestanding Triboelectric-Layer Nanogenerator for Harvesting Mechanical Energy at 85% Total Conversion Efficiency. *Advanced Materials* **2014,** *26* (38), 6599-6607.

16. Zhang, X.-S.; Han, M.-D.; Wang, R.-X.; Meng, B.; Zhu, F.-Y.; Sun, X.-M.; Hu, W.; Wang, W.; Li, Z.-H.; Zhang, H.-X., High-performance triboelectric nanogenerator with enhanced energy density based on single-step fluorocarbon plasma treatment. *Nano Energy* **2014,** *4*, 123-131.

17. Ding, W.; Wang, A. C.; Wu, C.; Guo, H.; Wang, Z. L., Human–Machine Interfacing Enabled by Triboelectric Nanogenerators and Tribotronics. *Advanced Materials Technologies* **2019,** *4* (1), 1800487.

18. Qi, J.; Wang, A. C.; Yang, W.; Zhang, M.; Hou, C.; Zhang, Q.; Li, Y.; Wang, H., Hydrogel-based hierarchically wrinkled stretchable nanofibrous membrane for high performance wearable triboelectric nanogenerator. *Nano Energy* **2020,** *67*, 104206.

19. Chen, J.; Yang, J.; Li, Z.; Fan, X.; Zi, Y.; Jing, Q.; Guo, H.; Wen, Z.; Pradel, K. C.; Niu, S.; Wang, Z. L., Networks of Triboelectric Nanogenerators for Harvesting Water Wave Energy: A Potential Approach toward Blue Energy. *ACS Nano* **2015,** *9* (3), 3324-3331.

20. Xu, M.; Wang, P.; Wang, Y. C.; Zhang, S. L.; Wang, A. C.; Zhang, C.; Wang, Z.; Pan, X.; Wang, Z. L., A soft and robust spring based triboelectric nanogenerator for harvesting arbitrary directional vibration energy and self-powered vibration sensing. *Advanced Energy Materials* **2018,** *8* (9), 1702432.

21. Dong, K.; Wu, Z.; Deng, J.; Wang, A. C.; Zou, H.; Chen, C.; Hu, D.; Gu, B.; Sun, B.; Wang, Z. L., A stretchable yarn embedded triboelectric nanogenerator as electronic skin for biomechanical energy harvesting and multifunctional pressure sensing. *Advanced Materials* **2018,** *30* (43), 1804944.

22. Deng, J.; Kuang, X.; Liu, R.; Ding, W.; Wang, A. C.; Lai, Y. C.; Dong, K.; Wen, Z.; Wang, Y.; Wang, L., Vitrimer elastomer-based jigsaw puzzle-like healable triboelectric nanogenerator for self-powered wearable electronics. *Advanced Materials* **2018,** *30* (14), 1705918.

23. Xia, K.; Du, C.; Zhu, Z.; Wang, R.; Zhang, H.; Xu, Z., Sliding-mode triboelectric nanogenerator based on paper and as a self-powered velocity and force sensor. *Applied Materials Today* **2018,** *13*, 190-197.

24. Yi, F.; Wang, X.; Niu, S.; Li, S.; Yin, Y.; Dai, K.; Zhang, G.; Lin, L.; Wen, Z.; Guo, H.; Wang, J.; Yeh, M.-H.; Zi, Y.; Liao, Q.; You, Z.; Zhang, Y.; Wang, Z. L., A highly shape-adaptive, stretchable design based on conductive liquid for energy harvesting and self-powered biomechanical monitoring. *Science Advances* **2016,** *2* (6), e1501624.

25. Wen, Z.; Shen, Q.; Sun, X., Nanogenerators for Self-Powered Gas Sensing. *Nano-Micro Letters* **2017,** *9* (4), 45.

26. Wang, Z. L.; Chen, J.; Lin, L., Progress in triboelectric nanogenerators as a new energy technology and self-powered sensors. *Energy & Environmental Science* **2015,** *8*, 2250-2282.

27. Yang, Y.; Zhou, Y.; Wu, J. M.; Wang, Z. L., Single Micro/Nanowire Pyroelectric Nanogenerators as Self-Powered Temperature Sensors. *ACS Nano* **2012,** *6* (9), 8456-8461.

28. Chen, H.; Miao, L.; Su, Z.; Song, Y.; Han, M.; Chen, X.; Cheng, X.; Chen, D.; Zhang, H., Fingertip-inspired electronic skin based on triboelectric sliding sensing and porous piezoresistive pressure detection. *Nano Energy* **2017,** *40*, 65-72.

29. Luo, J.; Wang, Z.; Xu, L.; Wang, A. C.; Han, K.; Jiang, T.; Lai, Q.; Bai, Y.; Tang, W.; Fan, F. R., Flexible and durable wood-based triboelectric nanogenerators for self-powered sensing in athletic big data analytics. *Nature communications* **2019,** *10* (1), 1-9.

30. Wang, J.; Wu, C.; Dai, Y.; Zhao, Z.; Wang, A.; Zhang, T.; Wang, Z. L., Achieving ultrahigh triboelectric charge density for efficient energy harvesting. *Nature communications* **2017,** *8* (1), 1-8.

31. Xu, L.; Bu, T. Z.; Yang, X. D.; Zhang, C.; Wang, Z. L., Ultrahigh charge density realized by charge pumping at ambient conditions for triboelectric nanogenerators. *Nano Energy* **2018,** *49*, 625-633.

32. Zou, H.; Zhang, Y.; Guo, L.; Wang, P.; He, X.; Dai, G.; Zheng, H.; Chen, C.; Wang, A. C.; Xu, C.; Wang, Z. L., Quantifying the triboelectric series. *Nature Communications* **2019**.

33. Zhang, C.; Bu, T.; Zhao, J.; Liu, G.; Yang, H.; Wang, Z. L., Tribotronics for Active Mechanosensation and Self-Powered Microsystems. *Advanced Functional Materials* **2019,** *29* (41), 1808114.

34. Peng, W.; Wang, X.; Yu, R.; Dai, Y.; Zou, H.; Wang, A. C.; He, Y.; Wang, Z. L., Enhanced Performance of a Self-Powered Organic/Inorganic Photodetector by Pyro-Phototronic and Piezo-Phototronic Effects. *Advanced Materials* **2017,** *29* (23), 1606698.

35. Pan, C.; Zhai, J.; Wang, Z. L., Piezotronics and Piezo-phototronics of Third Generation Semiconductor Nanowires. *Chemical Reviews* **2019,** *119* (15), 9303-9359.

36. Hu, W.; Zhang, C.; Wang, Z. L., Recent progress in piezotronics and tribotronics. *Nanotechnology* **2019,** *30* (4), 042001.

37. Zhang, C.; Wang, Z. L., Tribotronics—A new field by coupling triboelectricity and semiconductor. *Nano Today* **2016,** *11* (4), 521-536.

38. Xu, C.; Zi, Y.; Wang, A. C.; Zou, H.; Dai, Y.; He, X.; Wang, P.; Wang, Y. C.; Feng, P.; Li, D.; Wang, Z. L., On the Electron-Transfer Mechanism in the Contact-Electrification Effect. *Adv Mater* **2018,** *30* (15), e1706790.

39. Wang, A. C.; Zhang, B.; Xu, C.; Zou, H.; Lin, Z.; Wang, Z. L., Unraveling Temperature-Dependent Contact Electrification between Sliding-Mode Triboelectric Pairs. *Advanced Functional Materials* **2020,** *30* (12), 1909384.

40. Xu, C.; Wang, A. C.; Zou, H.; Zhang, B.; Zhang, C.; Zi, Y.; Pan, L.; Wang, P.; Feng, P.; Lin, Z., Raising the Working Temperature of a Triboelectric Nanogenerator by Quenching Down Electron Thermionic Emission in Contact-Electrification. *Advanced Materials* **2018,** *30* (38), 1803968.

41. Lowell, J., Contact electrification of metals. *Journal of Physics D: Applied Physics* **1975,** *8* (1), 53-63.

42. Harper, W. R.; Thomson, G. P., The Volta effect as a cause of static electrification. *Proceedings of the Royal Society of London. Series A. Mathematical and Physical Sciences* **1951,** *205* (1080), 83-103.

43. Lacks, D. J.; Mohan Sankaran, R., Contact electrification of insulating materials. *Journal of Physics D: Applied Physics* **2011,** *44* (45), 453001.

44. Hays, D. A., Contact electrification between mercury and polyethylene: Effect of surface oxidation. *The Journal of Chemical Physics* **1974,** *61* (4), 1455-1462.

45. Lowell, J., Surface states and the contact electrification of polymers. *Journal of Physics D: Applied Physics* **1977,** *10* (1), 65-71.

46. Liu, C.-y.; Bard, A. J., Electrons on dielectrics and contact electrification. *Chemical Physics Letters* **2009,** *480* (4), 145-156.

47. Shaw, P. E.; Barton, E. H., Experiments on tribo-electricity. I.—The tribo-electric series. *Proceedings of the Royal Society of London. Series A, Containing Papers of a Mathematical and Physical Character* **1917,** *94* (656), 16-33.

48. Mizes, H. A.; Conwell, E. M.; Salamida, D. P., Direct observation of ion transfer in contact charging between a metal and a polymer. *Applied Physics Letters* **1990,** *56* (16), 1597-1599.

49. Wiles, J. A.; Fialkowski, M.; Radowski, M. R.; Whitesides, G. M.; Grzybowski, B. A., Effects of Surface Modification and Moisture on the Rates of Charge Transfer between Metals and Organic Materials. *The Journal of Physical Chemistry B* **2004,** *108* (52), 20296-20302.

50. Wang, S.; Zi, Y.; Zhou, Y. S.; Li, S.; Fan, F.; Lin, L.; Wang, Z. L., Molecular surface functionalization to enhance the power output of triboelectric nanogenerators. *Journal of Materials Chemistry A* **2016,** *4* (10), 3728-3734.

51. Baytekin, H. T.; Patashinski, A. Z.; Branicki, M.; Baytekin, B.; Soh, S.; Grzybowski, B. A., The Mosaic of Surface Charge in Contact Electrification. *Science* **2011,** *333* (6040), 308-312.

52. Davies, D. K., Charge generation on dielectric surfaces. *Journal of Physics D: Applied Physics* **1969,** *2* (11), 1533-1537.

53. Horn, R. G.; Smith, D. T.; Grabbe, A., Contact electrification induced by monolayer modification of a surface and relation to acid–base interactions. *Nature* **1993,** *366* (6454), 442-443.

54. Liu, C.; Bard, A. J., Electrostatic electrochemistry at insulators. *Nature Materials* **2008,** *7*, 505.

55. Piperno, S.; Cohen, H.; Bendikov, T.; Lahav, M.; Lubomirsky, I., The Absence of Redox Reactions for Palladium(II) and Copper(II) on Electrostatically Charged Teflon: Relevance to the Concept of "Cryptoelectrons". *Angewandte Chemie International Edition* **2011,** *50* (25), 5654-5657.

56. Wiles, J. A.; Grzybowski, B. A.; Winkleman, A.; Whitesides, G. M., A Tool for Studying Contact Electrification in Systems Comprising Metals and Insulating Polymers. *Analytical Chemistry* **2003,** *75* (18), 4859-4867.

57. Yang, Y.; Zhang, H.; Chen, J.; Jing, Q.; Zhou, Y. S.; Wen, X.; Wang, Z. L., Single-Electrode-Based Sliding Triboelectric Nanogenerator for Self-Powered Displacement Vector Sensor System. *ACS Nano* **2013,** *7* (8), 7342-7351.

58. Wang, Z. L.; Jiang, T.; Xu, L., Toward the blue energy dream by triboelectric nanogenerator networks. In *Nano Energy*, 2017.

59. Seol, M.-L.; Han, J.-W.; Moon, D.-I.; Meyyappan, M., Triboelectric Nanogenerator for Mars Environment. *Nano Energy* **2017,** *39*.

60. Lu, C. X.; Han, C. B.; Gu, G. Q.; Chen, J.; Yang, Z. W.; Jiang, T.; He, C.; Wang, Z. L., Temperature Effect on Performance of Triboelectric Nanogenerator. *Advanced Engineering Materials* **2017,** *19* (12), 1700275.

61. Crowell, C. R., The Richardson constant for thermionic emission in Schottky barrier diodes. *Solid-State Electronics* **1965,** *8* (4), 395-399.

62. Racko, J.; Grmanova, A.; Breza, J., Extended thermionic emission-diffusion theory of charge transport through a schottky diode. *Solid-State Electronics* **1996**.

63. McCarty, L. S.; Whitesides, G. M., Electrostatic Charging Due to Separation of Ions at Interfaces: Contact Electrification of Ionic Electrets. *Angewandte Chemie International Edition* **2008,** *47* (12), 2188-2207.

64. Diaz, A.; Fenzel-Alexander, D.; Wollmann, D.; Barker, J. A., Importance of dissociated ions in contact charging. *Langmuir* **1992,** *8* (11), 2698-2706.

65. Harper, W. R., *Contact and frictional electrification*. Clarendon press: 1967.

66. Ruckdeschel, F. R.; Hunter, L. P., Thermionic return currents in contact electrification. *Journal of Applied Physics* **1977,** *48* (12), 4898-4902.

67. Burgo, T. A. d. L.; Rezende, C. A.; Bertazzo, S.; Galembeck, A.; Galembeck, F., Electric potential decay on polyethylene: Role of atmospheric water on electric charge build-up and dissipation. *Journal of Electrostatics* **2011**.

68. Naik, S.; Mukherjee, R.; Chaudhuri, B., Triboelectrification: A review of experimental and mechanistic modeling approaches with a special focus on pharmaceutical powders. *International journal of pharmaceutics* **2016,** *510* (1), 375-385.

69. Nguyen, V.; Yang, R., Effect of humidity and pressure on the triboelectric nanogenerator. *Nano Energy* **2013**.

70. Baytekin, H. T.; Baytekin, B.; Soh, S.; Grzybowski, B. A., Is Water Necessary for Contact Electrification? *Angewandte Chemie International Edition* **2011,** *50* (30), 6766-6770.

71. Wen, X.; Su, Y.; Yang, Y.; Zhang, H.; Wang, Z., Applicability of triboelectric generator over a wide range of temperature. *Nano Energy* **2014,** *4*, 150-156.

72. Wang, J.; Wu, C.; Dai, Y.; Zhao, Z.; Wang, A.; Zhang, T.; Wang, Z. L., Achieving ultrahigh triboelectric charge density for efficient energy harvesting. *Nature Communications* **2017,** *8* (1), 88.

73. Zhou, Y. S.; Wang, S.; Yang, Y.; Zhu, G.; Niu, S.; Lin, Z.-H.; Liu, Y.; Wang, Z. L., Manipulating Nanoscale Contact Electrification by an Applied Electric Field. *Nano Letters* **2014,** *14* (3), 1567-1572.

74. Horn, R. G.; Smith, D. T., Contact Electrification and Adhesion Between Dissimilar Materials. *Science* **1992,** *256* (5055), 362-364.

75. Cowley, A. M.; Sze, S. M., Surface States and Barrier Height of Metal-Semiconductor Systems. *Journal of Applied Physics* **1965,** *36* (10), 3212-3220.

76. Lowell, J.; Rose-Innes, A. C., Contact electrification. *Advances in Physics* **1980,** *29* (6), 947-1023.

77. McKinney, P. C.; Barrow, G. M., Chemical Bond. III. A One-Dimensional Theory of the Energetics and Ionic Character of the Hydrogen Bond. *The Journal of Chemical Physics* **1959,** *31* (2), 294-299.

78. Majerz, I.; Olovsson, I., The shape of the potential energy curves for NHN+ hydrogen bonds and the influence of non-linearity. *Physical Chemistry Chemical Physics* **2008,** *10* (21), 3043-3051.

79. Castle, G. S. P., Contact charging between insulators. *Journal of Electrostatics* **1997**.

80. Bailey, A. G., The charging of insulator surfaces. *Journal of Electrostatics* **2001,** *51-52*, 82-90.

81. Németh, E.; Albrecht, V.; Schubert, G.; Simon, F., Polymer tribo-electric charging: dependence on thermodynamic surface properties and relative humidity. *Journal of Electrostatics* **2003,** *58* (1-2), 3-16.

82. Mizutani, T.; Takai, Y.; Osawa, T.; Ieda, M., Barrier heights and surface states of metal-polymer (PET) contacts. *Journal of Physics D: Applied Physics* **1976,** *9* (15), 2253-2259.

83. Zhang, Y.; Shao, T., Effect of contact deformation on contact electrification: A first-principles calculation. *Journal of Physics D: Applied Physics* **2013**.

84. Shen, X.; Wang, A. E.; Sankaran, R. M.; Lacks, D. J., First-principles calculation of contact electrification and validation by experiment. *Journal of Electrostatics* **2016**.

85. Wang, Z. L., Piezoelectric Nanogenerators Based on Zinc Oxide Nanowire Arrays. *Science* **2006,** *312* (5771), 242-246.

86. Wang, Z.; Zhu, G.; Yang, Y.; Wang, S.; Pan, C., *Progress in nanogenerators for portable electronics*. 2012; Vol. 15, p 532–543.

87. Wu, C.; Wang, A. C.; Ding, W.; Guo, H.; Wang, Z. L., Triboelectric Nanogenerator: A Foundation of the Energy for the New Era. *Advanced Energy Materials* **2019,** *9* (1), 1802906.

88. Yi, F.; Wang, J.; Wang, X.; Niu, S.; Li, S.; Liao, Q.; Xu, Y.; You, Z.; Zhang, Y.; Wang, Z. L., Stretchable and Waterproof Self-Charging Power System for Harvesting Energy from Diverse Deformation and Powering Wearable Electronics. *ACS Nano* **2016,** *10* (7), 6519-6525.

89. Yu, Y.; Wang, X., Chemical modification of polymer surfaces for advanced triboelectric nanogenerator development. *Extreme Mechanics Letters* **2016,** *9*, 514-530.

90. Zhang, C.; Tang, W.; Han, C.; Fan, F.; Wang, Z. L., Theoretical Comparison, Equivalent Transformation, and Conjunction Operations of Electromagnetic Induction Generator and Triboelectric Nanogenerator for Harvesting Mechanical Energy. *Advanced Materials* **2014,** *26* (22), 3580-3591.

91. Nie, J.; Wang, Z.; Ren, Z.; Li, S.; Chen, X.; Lin Wang, Z., Power generation from the interaction of a liquid droplet and a liquid membrane. *Nature Communications* **2019**.

92. Lin, S.; Xu, L.; Zhu, L.; Chen, X.; Wang, Z. L., Electron Transfer in Nanoscale Contact Electrification: Photon Excitation Effect. *Advanced Materials* **2019,** *31* (27), 1901418.

93. Verdaguer, A.; Cardellach, M.; Segura, J. J.; Sacha, G. M.; Moser, J.; Zdrojek, M.; Bachtold, A.; Fraxedas, J., Charging and discharging of graphene in ambient conditions studied with scanning probe microscopy. *Applied Physics Letters* **2009,** *94*, 233105.

94. Sun, H.; Chu, H.; Wang, J.; Ding, L.; Li, Y., Kelvin probe force microscopy study on nanotriboelectrification. *Applied Physics Letters* **2010**.

95. Li, S.; Zhou, Y.; Zi, Y.; Zhang, G.; Wang, Z. L., Excluding Contact Electrification in Surface Potential Measurement Using Kelvin Probe Force Microscopy. *ACS Nano* **2016**.

96. Willatzen, M.; Lin Wang, Z., Theory of contact electrification: Optical transitions in two-level systems. *Nano Energy* **2018**.

97. Xu, C.; Zi, Y.; Wang, A. C.; Zou, H.; Dai, Y.; He, X.; Wang, P.; Wang, Y. C.; Feng, P.; Li, D., On the Electron-Transfer Mechanism in the Contact-Electrification Effect. *Advanced Materials* **2018,** *30* (15), 1706790.

98. Murphy, E. L.; Good, R. H., THERMIONIC EMISSION, FIELD EMISSION, AND THE TRANSITION REGION. *Physical Review* **1956,** *102* (6), 1464-1473.

99. Nicholson, K.; Newcastle, U. o.; Ireland, P.; Wanless, E.; Jameson, G., Design and construction of a laboratory scale cyclone tribocharger. Engineers Australia: 2008.

100. Ireland, P. M., Triboelectrification of particulate flows on surfaces: Part II — Mechanisms and models. *Powder Technology* **2010,** *198* (2), 199-210.

101. Hu, J.; Gu, P.; Zhou, Q.; Liang, C.; Liu, D.; Chen, X., Experimental and modeling study on mechanisms of sliding and rolling electrification. *Powder Technology* **2018,** *340*, 484-494.

102. Tokeshi, T.; Hiratsuka, K. i.; Sasaki, A.; Uchiyama, S.; Kajdas, C., Triboelectrification in Sliding/Rolling Contacts Using Twin-Ring Tribometer. *Tribology Transactions* **2009,** *52* (6), 759-767.

103. Rymuza, Z., Tribology of Polymers. *Archives of Civil and Mechanical Engineering* **2007,** *7* (4), 177-184.

104. Jia, B.-B.; Li, T.-S.; Liu, X.-J.; Cong, P.-H., Tribological behaviors of several polymer–polymer sliding combinations under dry friction and oil-lubricated conditions. *Wear* **2007,** *262* (11-12), 1353-1359.

105. Eiss, N. S.; McCann, B. P., Frictional Instabilities in Polymer-Polymer Sliding. *Tribology Transactions* **1993,** *36* (4), 686-692.

106. Rojsatean, J.; Larpsuriyakul, P.; Prakymoramas, N.; Thanomjitr, D.; Kaewket, S.; Singsom, T.; Srinun, D., Friction characteristics of self-lubricating ABS under different surface roughnesses and temperatures. *Tribology International* **2017,** *109*, 229-237.

107. Sayfidinov, K.; Cezan, S. D.; Baytekin, B.; Baytekin, H. T., Minimizing friction, wear, and energy losses by eliminating contact charging. *Science Advances* **2018**.

108. Ireland, P. M., The role of changing contact in sliding triboelectrification. *Journal of Physics D: Applied Physics* **2008,** *41* (2).

109. Wåhlin, A.; Bäckström, G., Sliding electrification of Teflon by metals. *Journal of Applied Physics* **1974,** *45* (5), 2058-2064.

110. Lin, S.; Xu, L.; Xu, C.; Chen, X.; Wang, A. C.; Zhang, B.; Lin, P.; Yang, Y.; Zhao, H.; Wang, Z. L., Electron Transfer in Nanoscale Contact Electrification: Effect of Temperature in the Metal–Dielectric Case. *Advanced Materials* **2019,** *31* (17), 1808197.

111. Hughes, J. F., Electrostatics: Principles, Problems and Applications. *Physics Bulletin* **1987,** *38* (11), 424-424.

112. Vick, F. A., Theory of contact electrification. *British Journal of Applied Physics* **1953,** *4*, S1-S5.

113. Zhou, Y. S.; Liu, Y.; Zhu, G.; Lin, Z.-H.; Pan, C.; Jing, Q.; Wang, Z. L., In Situ Quantitative Study of Nanoscale Triboelectrification and Patterning. *Nano Letters* **2013,** *13*, 2771-2776.

114. Sun, N.; Wen, Z.; Zhao, F.; Yang, Y.; Shao, H.; Zhou, C.; Shen, Q.; Feng, K.; Peng, M.; Li, Y.; Sun, X., All flexible electrospun papers based self-charging power system. *Nano Energy* **2017,** *38*, 210-217.

115. Lin, L.; Wang, S.; Xie, Y.; Jing, Q.; Niu, S.; Hu, Y.; Wang, Z. L., Segmentally Structured Disk Triboelectric Nanogenerator for Harvesting Rotational Mechanical Energy. *Nano Letters* **2013,** *13* (6), 2916-2923.

116. Fertis, D. G., *Nonlinear Structural Engineering: With Unique Theories and Methods to Solve Effectively Complex Nonlinear Problems*. Springer Berlin Heidelberg: 2007.

117. Cottrell, G. A., The measurement of true contact charge density using soft rubber. *Journal of Physics D: Applied Physics* **1978,** *11* (5), 681-687.

118. Reif, F., *Fundamentals of statistical and thermal physics / [by] F. Reif*. McGraw-Hill Kogakusha: Tokyo, 1965.

119. Camara, C. G.; Escobar, J. V.; Hird, J. R.; Putterman, S. J., Correlation between nanosecond X-ray flashes and stick-slip friction in peeling tape. *Nature* **2008**.

120. Stöcker, H.; Rühl, M.; Heinrich, A.; Mehner, E.; Meyer, D. C., Generation of hard X-ray radiation using the triboelectric effect bypeeling adhesive tape. *Journal of Electrostatics* **2013**.

121. Nakayama, K., Triboplasma Generation and Triboluminescence: Influence of Stationary Sliding Partner. *Tribology Letters* **2010,** *37* (2), 215-228.

122. Wang, J.; Li, S.; Yi, F.; Zi, Y.; Lin, J.; Wang, X.; Xu, Y.; Wang, Z. L., Sustainably powering wearable electronics solely by biomechanical energy. *Nature Communications* **2016,** *7* (1), 12744.

123. Chu, Z.; Yang, M.; Schulz, P.; Wu, D.; Ma, X.; Seifert, E.; Sun, L.; Li, X.; Zhu, K.; Lai, K., Impact of grain boundaries on efficiency and stability of organic-inorganic trihalide perovskites. *Nat Commun* **2017,** *8* (1), 2230.

124. Tai, Q.; Tang, K.-C.; Yan, F., Recent progress of inorganic perovskite solar cells. *Energy & Environmental Science* **2019,** *12* (8), 2375-2405.

125. Shi, D.; Adinolfi, V.; Comin, R.; Yuan, M.; Alarousu, E.; Buin, A.; Chen, Y.; Hoogland, S.; Rothenberger, A.; Katsiev, K.; Losovyj, Y.; Zhang, X.; Dowben, P. A.; Mohammed, O. F.; Sargent, E. H.; Bakr, O. M., Low trap-state density and long carrier diffusion in organolead trihalide perovskite single crystals. *Science* **2015,** *347* (6221), 519-522.

126. Ponseca, C. S., Jr.; Savenije, T. J.; Abdellah, M.; Zheng, K.; Yartsev, A.; Pascher, T.; Harlang, T.; Chabera, P.; Pullerits, T.; Stepanov, A.; Wolf, J. P.; Sundstrom, V., Organometal halide perovskite solar cell materials rationalized: ultrafast charge generation, high and microsecond-long balanced mobilities, and slow recombination. *J Am Chem Soc* **2014,** *136* (14), 5189-92.

127. Oga, H.; Saeki, A.; Ogomi, Y.; Hayase, S.; Seki, S., Improved understanding of the electronic and energetic landscapes of perovskite solar cells: high local charge carrier mobility, reduced recombination, and extremely shallow traps. *J Am Chem Soc* **2014,** *136* (39), 13818-25.

128. He, Y.; Yoon, Y. J.; Harn, Y. W.; Biesold-McGee, G. V.; Liang, S.; Lin, C. H.; Tsukruk, V. V.; Thadhani, N.; Kang, Z.; Lin, Z., Unconventional route to dual-shelled organolead halide perovskite nanocrystals with controlled dimensions, surface chemistry, and stabilities. *Science Advances* **2019,** *5* (11), eaax4424.

129. Yoon, Y. J.; Chang, Y.; Zhang, S.; Zhang, M.; Pan, S.; He, Y.; Lin, C. H.; Yu, S.; Chen, Y.; Wang, Z.; Ding, Y.; Jung, J.; Thadhani, N.; Tsukruk, V. V.; Kang, Z.; Lin, Z., Enabling Tailorable Optical Properties and Markedly Enhanced Stability of Perovskite Quantum Dots by Permanently Ligating with Polymer Hairs. *Adv Mater* **2019,** *31* (32), e1901602.

130. Loiudice, A.; Saris, S.; Oveisi, E.; Alexander, D. T. L.; Buonsanti, R., CsPbBr(3) QD/AlO(x) Inorganic Nanocomposites with Exceptional Stability in Water, Light, and Heat. *Angew Chem Int Ed Engl* **2017,** *56* (36), 10696-10701.

131. Wang, H. C.; Lin, S. Y.; Tang, A. C.; Singh, B. P.; Tong, H. C.; Chen, C. Y.; Lee, Y. C.; Tsai, T. L.; Liu, R. S., Mesoporous Silica Particles Integrated with All-Inorganic CsPbBr3 Perovskite Quantum-Dot Nanocomposites (MP-PQDs) with High Stability and Wide Color Gamut Used for Backlight Display. *Angew Chem Int Ed Engl* **2016,** *55* (28), 7924-9.

132. Liu, Y.; Sun, N.; Liu, J.; Wen, Z.; Sun, X.; Lee, S. T.; Sun, B., Integrating a Silicon Solar Cell with a Triboelectric Nanogenerator via a Mutual Electrode for Harvesting Energy from Sunlight and Raindrops. *ACS Nano* **2018,** *12* (3), 2893-2899.

133. Semwal, B. S.; Panwar, N. S., Dielectric properties of perovskite crystals. *Bulletin of Materials Science* **1992,** *15* (3), 237.

134. Ming, W.; Shi, H.; Du, M.-H., Large dielectric constant, high acceptor density, and deep electron traps in perovskite solar cell material CsGeI3. *Journal of Materials Chemistry A* **2016,** *4* (36), 13852-13858.

135. Su, L.; Zhao, Z.; Li, H.; Wang, Y.; Kuang, S.; Cao, G.; Wang, Z.; Zhu, G., Photoinduced enhancement of a triboelectric nanogenerator based on an organolead halide perovskite. *Journal of Materials Chemistry C* **2016,** *4* (43), 10395-10399.

136. Yang, X. D.; Han, J. J.; Wang, G.; Liao, L. P.; Xu, C. Y.; Hu, W.; Li, P.; Wu, B.; Elseman, A. M.; Zhou, G. D.; Song, Q. L., Robust perovskite-based triboelectric nanogenerator enhanced by broadband light and interface engineering. *Journal of Materials Science* **2019,** *54* (12), 9004-9016.

137. Wang, Y.; Duan, J.; Yang, X.; Liu, L.; Zhao, L.; Tang, Q., The unique dielectricity of inorganic perovskites toward high-performance triboelectric nanogenerators. *Nano Energy* **2020,** *69*.

138. Yang, C.; Jiang, J.-S.; Qian, F.-Z.; Jiang, D.-M.; Wang, C.-M.; Zhang, W.-G., Effect of Ba doping on magnetic and dielectric properties of nanocrystalline BiFeO3 at room temperature. *Journal of Alloys and Compounds* **2010,** *507* (1), 29-32.

139. Mahapatra, A.; Prochowicz, D.; Tavakoli, M. M.; Trivedi, S.; Kumar, P.; Yadav, P., A review of aspects of additive engineering in perovskite solar cells. *Journal of Materials Chemistry A* **2020,** *8* (1), 27-54.

140. Yang, J.; Chen, S.; Xu, J.; Zhang, Q.; Liu, H.; Liu, Z.; Yuan, M., A Review on Improving the Quality of Perovskite Films in Perovskite Solar Cells via the Weak Forces Induced by Additives. *Applied Sciences* **2019,** *9* (20).

141. Li, Y.; Ji, L.; Liu, R.; Zhang, C.; Mak, C. H.; Zou, X.; Shen, H.-H.; Leu, S.-Y.; Hsu, H.-Y., A review on morphology engineering for highly efficient and stable hybrid perovskite solar cells. *Journal of Materials Chemistry A* **2018,** *6* (27), 12842-12875.

142. Wilson, J. N.; Frost, J. M.; Wallace, S. K.; Walsh, A., Dielectric and ferroic properties of metal halide perovskites. *APL Materials* **2019,** *7* (1).

143. Yang, W. S.; Noh, J. H.; Jeon, N. J.; Kim, Y. C.; Ryu, S.; Seo, J.; Seok, S. I., High-performance photovoltaic perovskite layers fabricated through intramolecular exchange. *Science 348* (6240), 1234-1237.

144. Lee, J. W.; Seol, D. J.; Cho, A. N.; Park, N. G., High-efficiency perovskite solar cells based on the black polymorph of HC(NH2)2 PbI3. *Adv Mater* **2014,** *26* (29), 4991-8.

145. Choi, H.; Jeong, J.; Kim, H.-B.; Kim, S.; Walker, B.; Kim, G.-H.; Kim, J. Y., Cesium-doped methylammonium lead iodide perovskite light absorber for hybrid solar cells. *Nano Energy* **2014,** *7*, 80-85.

146. Sadhanala, A.; Deschler, F.; Thomas, T. H.; Dutton, S. E.; Goedel, K. C.; Hanusch, F. C.; Lai, M. L.; Steiner, U.; Bein, T.; Docampo, P.; Cahen, D.; Friend, R. H., Preparation of Single-Phase Films of CH3NH3Pb(I1-xBrx)3 with Sharp Optical Band Edges. *J Phys Chem Lett* **2014,** *5* (15), 2501-5.

147. Im, J. H.; Jang, I. H.; Pellet, N.; Gratzel, M.; Park, N. G., Growth of CH3NH3PbI3 cuboids with controlled size for high-efficiency perovskite solar cells. *Nat Nanotechnol* **2014,** *9* (11), 927-32.

148. Hoke, E. T.; Slotcavage, D. J.; Dohner, E. R.; Bowring, A. R.; Karunadasa, H. I.; McGehee, M. D., Reversible photo-induced trap formation in mixed-halide hybrid perovskites for photovoltaics. *Chem Sci* **2015,** *6* (1), 613-617.

149. Yi, C.; Luo, J.; Meloni, S.; Boziki, A.; Ashari-Astani, N.; Grätzel, C.; Zakeeruddin, S. M.; Röthlisberger, U.; Grätzel, M., Entropic stabilization of mixed A-cation ABX3 metal halide perovskites for high performance perovskite solar cells. *Energy & Environmental Science* **2016,** *9* (2), 656-662.

150. Saliba, M.; Matsui, T.; Seo, J. Y.; Domanski, K.; Correa-Baena, J. P.; Nazeeruddin, M. K.; Zakeeruddin, S. M.; Tress, W.; Abate, A.; Hagfeldt, A.; Gratzel, M., Cesium-containing triple cation perovskite solar cells: improved stability, reproducibility and high efficiency. *Energy Environ Sci* **2016,** *9* (6), 1989-1997.

151. Jesper Jacobsson, T.; Correa-Baena, J.-P.; Pazoki, M.; Saliba, M.; Schenk, K.; Grätzel, M.; Hagfeldt, A., Exploration of the compositional space for mixed lead halogen

perovskites for high efficiency solar cells. *Energy & Environmental Science* **2016,** *9* (5), 1706-1724.

152. Bi, D.; Luo, J.; Zhang, F.; Magrez, A.; Athanasopoulou, E. N.; Hagfeldt, A.; Gratzel, M., Morphology Engineering: A Route to Highly Reproducible and High Efficiency Perovskite Solar Cells. *ChemSusChem* **2017,** *10* (7), 1624-1630.

153. Hawash, Z.; Ono, L. K.; Qi, Y., Recent Advances in Spiro-MeOTAD Hole Transport Material and Its Applications in Organic–Inorganic Halide Perovskite Solar Cells. *Advanced Materials Interfaces* **2017,** *5* (1).

154. Lee, J.-W.; Bae, S.-H.; De Marco, N.; Hsieh, Y.-T.; Dai, Z.; Yang, Y., The role of grain boundaries in perovskite solar cells. *Materials Today Energy* **2018,** *7*, 149-160.

155. Zhou, P.; Bu, T.; Shi, S.; Li, L.; Zhang, Y.; Ku, Z.; Peng, Y.; Zhong, J.; Cheng, Y.-B.; Huang, F., Efficient and stable mixed perovskite solar cells using P3HT as a hole transporting layer. *Journal of Materials Chemistry C* **2018,** *6* (21), 5733-5737.

156. Qi, J.; Li, L.; Xiong, H.; Wang, A. C.; Hou, C.; Zhang, Q.; Li, Y.; Wang, H., Highly efficient walking perovskite solar cells based on thermomechanical polymer films. *Journal of Materials Chemistry A* **2019,** *7* (45), 26154-26161.

157. Nukunudompanich, M.; Budiutama, G.; Suzuki, K.; Hasegawa, K.; Ihara, M., Dominant effect of the grain size of the MAPbI3 perovskite controlled by the surface roughness of TiO2 on the performance of perovskite solar cells. *CrystEngComm* **2020,** *22* (16), 2718-2727.

158. Weber, O. J.; Charles, B.; Weller, M. T., Phase behaviour and composition in the formamidinium–methylammonium hybrid lead iodide perovskite solid solution. *Journal of Materials Chemistry A* **2016,** *4* (40), 15375-15382.

159. Fu, K.; Ho-Baillie, A. W.; Mulmudi, H. K.; Trang, P. T. T., *Perovskite Solar Cells: Technology and Practices*. Apple Academic Press: 2019.

160. Pellet, N.; Gao, P.; Gregori, G.; Yang, T. Y.; Nazeeruddin, M. K.; Maier, J.; Gratzel, M., Mixed-organic-cation perovskite photovoltaics for enhanced solar-light harvesting. *Angew Chem Int Ed Engl* **2014,** *53* (12), 3151-7.

161. Mohebpour, M. A.; Saffari, M.; Soleimani, H. R.; Tagani, M. B., High performance of mixed halide perovskite solar cells: Role of halogen atom and plasmonic nanoparticles on the ideal current density of cell. *Physica E: Low-dimensional Systems and Nanostructures* **2018,** *97*, 282-289.

162. Su, L.; Zhao, Z. X.; Li, H. Y.; Yuan, J.; Wang, Z. L.; Cao, G. Z.; Zhu, G., High-Performance Organolead Halide Perovskite-Based Self-Powered Triboelectric Photodetector. *ACS Nano* **2015,** *9* (11), 11310–11316.

163. Kubicki, D. J.; Prochowicz, D.; Hofstetter, A.; Zakeeruddin, S. M.; Grätzel, M.; Emsley, L., Phase Segregation in Cs-, Rb- and K-Doped Mixed-Cation (MA)x(FA)1–xPbI3 Hybrid Perovskites from Solid-State NMR. *Journal of the American Chemical Society* **2017,** *139* (40), 14173-14180.

164. Xu, J.; Boyd, C. C.; Yu, Z. J.; Palmstrom, A. F.; Witter, D. J.; Larson, B. W.; France, R. M.; Werner, J.; Harvey, S. P.; Wolf, E. J.; Weigand, W.; Manzoor, S.; van Hest, M. F. A. M.; Berry, J. J.; Luther, J. M.; Holman, Z. C.; McGehee, M. D., Triple-halide wide–band gap perovskites with suppressed phase segregation for efficient tandems. *Science* **2020,** *367* (6482), 1097-1104.

165. Rahman, M.; Edvinsson, T.; Hagfeldt, A.; Pazoki, M., *CHARACTERIZATION TECHNIQUES FOR PEROVSKITE SOLAR CELL MATERIALS*. 2019.

166. Prasanna, R.; Gold-Parker, A.; Leijtens, T.; Conings, B.; Babayigit, A.; Boyen, H.-G.; Toney, M. F.; McGehee, M. D., Band Gap Tuning via Lattice Contraction and Octahedral Tilting in Perovskite Materials for Photovoltaics. *Journal of the American Chemical Society* **2017,** *139* (32), 11117-11124.

167. Ghosh, D.; Walsh Atkins, P.; Islam, M. S.; Walker, A. B.; Eames, C., Good Vibrations: Locking of Octahedral Tilting in Mixed-Cation Iodide Perovskites for Solar Cells. *ACS Energy Letters* **2017,** *2* (10), 2424-2429.

168. Kim, D.; Tcho, I.-W.; Jin, I. K.; Park, S.-J.; Jeon, S.-B.; Kim, W.-G.; Cho, H.-S.; Lee, H.-S.; Jeoung, S. C.; Choi, Y.-K., Direct-laser-patterned friction layer for the output enhancement of a triboelectric nanogenerator. *Nano Energy* **2017,** *35*, 379-386.

169. Jeong, C. K.; Baek, K. M.; Niu, S.; Nam, T. W.; Hur, Y. H.; Park, D. Y.; Hwang, G.-T.; Byun, M.; Wang, Z. L.; Jung, Y. S.; Lee, K. J., Topographically-Designed Triboelectric Nanogenerator via Block Copolymer Self-Assembly. *Nano Letters* **2014,** *14* (12), 7031-7038.

170. Saadatnia, Z.; Esmailzadeh, E.; Naguib, H. E., High Performance Triboelectric Nanogenerator by Hot Embossing on Self-Assembled Micro-Particles. *Advanced Engineering Materials* **2019,** *21* (1), 1700957.

171. Kumar, B.; Rao, T., AFM studies on surface morphology, topography and texture of nanostructured zinc aluminum oxide thin films. *Digest Journal of Nanomaterials and Biostructures* **2012,** *7*, 1881-1889.

172. Kaushik, B. K.; Kumar, B.; Prajapati, S.; Mittal, P., *Organic Thin-Film Transistor Applications: Materials to Circuits*. CRC Press: 2016.

173. Wang, X., *Azo Polymers Synthesis, Functions and Applications*. Springer: Berlin, 2017.

174. Harada, J.; Ogawa, K.; Tomoda, S., Molecular Motion and Conformational Interconversion of Azobenzenes in Crystals as Studied by X-ray Diffraction. *Acta Crystallographica Section B* **1997,** *53* (4), 662-672.

175. Hartley, G. S., The cis-Form of Azobenzene and the Velocity of the Thermal cis --> trans-Conversion of Ambenzene and Some Derivatives. *J. Chem. Soc.* **1938**, 633-642.

176. Hugel, T.; Holland, N. B.; Cattani, A.; Moroder, L.; Seitz, M.; Gaub, H. E., Single-Molecule Optomechanical Cycle. *Science* **2002,** *296* (5570), 1103-1106.

177. Holland, N. B.; Hugel, T.; Neuert, G.; Cattani-Scholz, A.; Renner, C.; Oesterhelt, D.; Moroder, L.; Seitz, M.; Gaub, H. E., Single Molecule Force Spectroscopy of Azobenzene Polymers: Switching Elasticity of Single Photochromic Macromolecules. *Macromolecules* **2003,** *36* (6), 2015-2023.

178. Natansohn, A.; Rochon, P., Photoinduced Motions in Azo-Containing Polymers. *Chem. Rev.* **2002,** *102*, 4139-4175.

179. Lee, S.; Kang, H. S.; Park, J. K., Directional photofluidization lithography: micro/nanostructural evolution by photofluidic motions of azobenzene materials. *Adv Mater* **2012,** *24* (16), 2069-103.

180. Shishido, A., Rewritable holograms based on azobenzene-containing liquid-crystalline polymers. *Polymer Journal* **2010,** *42* (7), 525-533.

181. Priimagi, A.; Shevchenko, A., Azopolymer-based micro- and nanopatterning for photonic applications. *Journal of Polymer Science Part B: Polymer Physics* **2014,** *52* (3), 163-182.

182. Fu, S.; Zhao, Y., Orientation of Azobenzene Mesogens in Side-Chain Liquid Crystalline Polymers: Interplay between Effects of Mechanical Stretching, Photoisomerization and Thermal Annealing. *Macromolecules* **2015,** *48* (15), 5088-5098.

183. Lu, X.; Guo, S.; Tong, X.; Xia, H.; Zhao, Y., Tunable Photocontrolled Motions Using Stored Strain Energy in Malleable Azobenzene Liquid Crystalline Polymer Actuators. *Adv Mater* **2017,** *29* (28).

184. Lv, J. A.; Liu, Y.; Wei, J.; Chen, E.; Qin, L.; Yu, Y., Photocontrol of fluid slugs in liquid crystal polymer microactuators. *Nature* **2016,** *537* (7619), 179-84.

185. Wang, D.; Wang, X., Amphiphilic azo polymers: Molecular engineering, self-assembly and photoresponsive properties. *Progress in Polymer Science* **2013,** *38* (2), 271-301.

186. Choi, J.; Cho, W.; Jung, Y. S.; Kang, H. S.; Kim, H. T., Direct Fabrication of Micro/Nano-Patterned Surfaces by Vertical-Directional Photofluidization of Azobenzene Materials. *ACS Nano* **2017,** *11* (2), 1320-1327.

187. Oscurato, S. L.; Borbone, F.; Maddalena, P.; Ambrosio, A., Light-Driven Wettability Tailoring of Azopolymer Surfaces with Reconfigured Three-Dimensional Posts. *ACS Appl Mater Interfaces* **2017,** *9* (35), 30133-30142.

188. Wang, D.; Ye, G.; Zhu, Y.; Wang, X., Photoinduced Mass-Migration Behavior of Two Amphiphilic Side-Chain Azo Diblock Copolymers with Different Length Flexible Spacers. *Macromolecules* **2009,** *42*, 2651-2657.

189. Lee, S.; Kang, H. S.; Ambrosio, A.; Park, J. K.; Marrucci, L., Directional Superficial Photofluidization for Deterministic Shaping of Complex 3D Architectures. *ACS Appl Mater Interfaces* **2015,** *7* (15), 8209-17.

190. Li, Y.; He, Y.; Tong, X.; Wang, X., Photoinduced Deformation of Amphiphilic Azo Polymer Colloidal Spheres. *J. Am. Chem. Soc.* **2005,** *127*, 2402-2403.

191. Wang, W.; Du, C.; Wang, X.; He, X.; Lin, J.; Li, L.; Lin, S., Directional photomanipulation of breath figure arrays. *Angew Chem Int Ed Engl* **2014,** *53* (45), 12116-9.

192. Li, J.; Chen, L.; Xu, J.; Wang, K.; Wang, X.; He, X.; Dong, H.; Lin, S.; Zhu, J., Photoguided Shape Deformation of Azobenzene-Containing Polymer Microparticles. *Langmuir* **2015,** *31* (48), 13094-100.

193. Kong, X.; Wang, X.; Luo, T.; Yao, Y.; Li, L.; Lin, S., Photomanipulated Architecture and Patterning of Azopolymer Array. *ACS Appl Mater Interfaces* **2017,** *9* (22), 19345-19353.

194. Wang, W.; Yao, Y.; Luo, T.; Chen, L.; Lin, J.; Li, L.; Lin, S., Deterministic Reshaping of Breath Figure Arrays by Directional Photomanipulation. *ACS Appl Mater Interfaces* **2017,** *9* (4), 4223-4230.

195. Weigert, F., Dichroism induced in a fine-grain silverchloride emulsion by a beam of linearly polarized light. *Verh. Dtsch. Phys. Ges* **1919,** *21*, 479-483.

196. Gelebart, A. H.; Jan Mulder, D.; Varga, M.; Konya, A.; Vantomme, G.; Meijer, E. W.; Selinger, R. L. B.; Broer, D. J., Making waves in a photoactive polymer film. *Nature* **2017,** *546* (7660), 632-636.

197. Kumar, K.; Knie, C.; Bleger, D.; Peletier, M. A.; Friedrich, H.; Hecht, S.; Broer, D. J.; Debije, M. G.; Schenning, A. P., A chaotic self-oscillating sunlight-driven polymer actuator. *Nat Commun* **2016,** *7*, 11975.

198. Takeshima, T.; Liao, W.-y.; Nagashima, Y.; Beppu, K.; Hara, M.; Nagano, S.; Seki, T., Photoresponsive Surface Wrinkle Morphologies in Liquid Crystalline Polymer Films. *Macromolecules* **2015,** *48* (18), 6378-6384.

199. Serak, S.; Tabiryan, N.; Vergara, R.; White, T. J.; Vaia, R. A.; Bunning, T. J., Liquid crystalline polymer cantilever oscillators fueled by light. *Soft Matter* **2010,** *6* (4), 779-783.

200. Tabiryan, N.; Serak, S.; Dai, X.-M.; Bunning, T., Polymer film with optically controlled form and actuation. *Optics Express* **2005,** *13* (19), 7442-7448.

201. White, T. J.; Tabiryan, N. V.; Serak, S. V.; Hrozhyk, U. A.; Tondiglia, V. P.; Koerner, H.; Vaia, R. A.; Bunning, T. J., A high frequency photodriven polymer oscillator. *Soft Matter* **2008,** *4* (9).

202. Yu, Y.; Nakano, M.; Shishido, A.; Shiono, T.; Ikeda, T., Effect of Cross-linking Density on Photoinduced Bending Behavior of Oriented Liquid-Crystalline Network Films Containing Azobenzene. *Chem. Mater.* **2004,** *16*, 1637-1643.

203. Li, X.; Li, B.; He, M.; Wang, W.; Wang, T.; Wang, A.; Yu, J.; Wang, Z.; Hong, S. W.; Byun, M., Convenient and robust route to photoswitchable hierarchical liquid crystal polymer stripes via flow-enabled self-assembly. *ACS applied materials & interfaces* **2018,** *10* (5), 4961-4970.

204. Gritsai, Y.; Goldenberg, L. M.; Stumpe, J., Efficient single-beam light manipulation of 3D microstructures in azobenzene-containing materials. *Optics express* **2011,** *19* (19), 18687-18695.

205. Wang, G.; Tong, X.; Zhao, Y., Preparation of azobenzene-containing amphiphilic diblock copolymers for light-responsive micellar aggregates. *Macromolecules* **2004,** *37* (24), 8911-8917.

206. Zhao, Y.; Qi, B.; Tong, X.; Zhao, Y., Synthesis of double side-chain liquid crystalline block copolymers using RAFT polymerization and the orientational cooperative effect. *Macromolecules* **2008,** *41* (11), 3823-3831.

207. Liu, J. H.; Chiu, Y. H., Behaviors of Self-Assembled Diblock Copolymer with Pendant Photosensitive Azobenzene Segments. *J. Polym. Sci. Pol. Chem.* **2010,** *48* (5), 1142-1148.

208. He, X. H.; Wu, J. X.; Gao, C. Y., Novel amphiphilic graft block azobenzene-containing copolymer with polypeptide block: synthesis, self-assembly and photo-responsive behavior. *Rsc Advances* **2020,** *10* (10), 5747-5757.

209. Gao, F.; Xing, Y. H.; Yao, Y.; Sun, L. Y.; Sun, Y.; He, X. H.; Lin, S. L., Self-assembly and multi-stimuli responsive behavior of PAA-b-PAzoMA-b-PNIPAM triblock copolymers. *Polymer Chemistry* **2017,** *8* (48), 7529-7536.

210. Lee, T. L.; Lo, C. T., Photoresponsive and Fluorescence Behaviors of Azobenzene-Containing Amphiphilic Block Copolymers. *J. Polym. Sci. Pt. B-Polym. Phys.* **2017,** *55* (10), 793-803.

211. Tsao, S. C.; Lo, C. T., Photoresponsive behavior and self-organization of azobenzene-containing block copolymers. *Rsc Advances* **2014,** *4* (45), 23585-23594.

212. Bunz, U. H. F., Breath Figures as a Dynamic Templating Method for Polymers and Nanomaterials. *Advanced Materials* **2006,** *18* (8), 973-989.

213. Wan, L. S.; Zhu, L. W.; Ou, Y.; Xu, Z. K., Multiple interfaces in self-assembled breath figures. *Chem Commun (Camb)* **2014,** *50* (31), 4024-39.

214. Dou, Y.; Jin, M.; Zhou, G.; Shui, L., Breath Figure Method for Construction of Honeycomb Films. *Membranes (Basel)* **2015,** *5* (3), 399-424.

215. Zhang, A.; Bai, H.; Li, L., Breath Figure: A Nature-Inspired Preparation Method for Ordered Porous Films. *Chem Rev* **2015,** *115* (18), 9801-68.

216. Bormashenko, E., Breath-Figure Self-Assembly, a Versatile Method of Manufacturing Membranes and Porous Structures: Physical, Chemical and Technological Aspects. *Membranes (Basel)* **2017,** *7* (3).

217. Widawski, G.; Rawiso, M.; François, B., Self-organized honeycomb morphology of star-polymer polystyrene films. *Nature* **1994,** *369* (6479), 387-389.

218. Stenzel, M. H., Formation of Regular Honeycomb-Patterned Porous Film by Self-Organization. *Australian Journal of Chemistry* **2002,** *55* (4), 239-243.

219. Maruyama, N.; Koito, T.; Nishida, J.; Sawadaishi, T.; Cieren, X.; Ijiro, K.; Karthaus, O.; Shimomura, M., Mesoscopic patterns of molecular aggregates on solid substrates. *Thin Solid Films* **1998,** *327-329*, 854-856.

220. Srinivasarao, M.; Collings, D.; Philips, A.; Patel, S., Three-Dimensionally Ordered Array of Air Bubbles in a Polymer Film. *Science* **2001,** *292* (5514), 79-83.

221. Yabu, H.; Shimomura, M., Simple Fabrication of Micro Lens Arrays. *Langmuir* **2005,** *21* (5), 1709-1711.

222. Wang, J.; Shen, H.-X.; Wang, C.-F.; Chen, S., Multifunctional ionomer-derived honeycomb-patterned architectures and their performance in light enhancement of light-emitting diodes. *Journal of Materials Chemistry* **2012,** *22* (9), 4089-4096.

223. Bolognesi, A.; Botta, C.; Yunus, S., Micro-patterning of organic light emitting diodes using self-organised honeycomb ordered polymer films. *Thin Solid Films* **2005,** *492* (1), 307-312.

224. Uraki, Y.; Nemoto, J.; Otsuka, H.; Tamai, Y.; Sugiyama, J.; Kishimoto, T.; Ubukata, M.; Yabu, H.; Tanaka, M.; Shimomura, M., Honeycomb-like architecture produced by living bacteria, Gluconacetobacter xylinus. *Carbohydrate Polymers* **2007,** *69* (1), 1-6.

225. Bashmakov, I. A.; Govor, L. V.; Solovieva, L. V.; Parisi, J., Preparation of Self-Assembled Carbon Network Structures with Magnetic Nanoparticles. *Macromolecular Chemistry and Physics* **2002,** *203* (3), 544-549.

226. Ishii, D.; Yabu, H.; Shimomura, M., Selective metal deposition in hydrophobic porous cavities of self-organized honeycomb-patterned polymer films by all-wet electroless plating. *Colloids and Surfaces A: Physicochemical and Engineering Aspects* **2008,** *313-314*, 590-594.

227. Ohzono, T.; Shimomura, M., Simple fabrication of ring-like microwrinkle patterns. *Colloids and Surfaces A: Physicochemical and Engineering Aspects* **2006,** *284-285*, 505-508.

228. Nyström, D.; Malmström, E.; Hult, A.; Blakey, I.; Boyer, C.; Davis, T. P.; Whittaker, M. R., Biomimetic Surface Modification of Honeycomb Films via a "Grafting From" Approach. *Langmuir* **2010,** *26* (15), 12748-12754.

229. de León, A. S.; Rodríguez-Hernández, J.; Cortajarena, A. L., Honeycomb patterned surfaces functionalized with polypeptide sequences for recognition and selective bacterial adhesion. *Biomaterials* **2013,** *34* (5), 1453-1460.

230. Min, E.; Wong, K. H.; Stenzel, M. H., Microwells with Patterned Proteins by a Self-Assembly Process Using Honeycomb-Structured Porous Films. *Advanced Materials* **2008,** *20* (18), 3550-3556.

231. Wang, C.; Liu, Q.; Shao, X.; Yang, G.; Xue, H.; Hu, X., One step fabrication of nanoelectrode ensembles formed via amphiphilic block copolymers self-assembly and selective voltammetric detection of uric acid in the presence of high ascorbic acid content. *Talanta* **2007,** *71* (1), 178-185.

232. Chen, P.-C.; Wan, L.-S.; Ke, B.-B.; Xu, Z.-K., Honeycomb-Patterned Film Segregated with Phenylboronic Acid for Glucose Sensing. *Langmuir* **2011,** *27* (20), 12597-12605.

233. Sun, X.; Brückner, C.; Nieh, M.-P.; Lei, Y., A fluorescent polymer film with self-assembled three-dimensionally ordered nanopores: preparation, characterization and its application for explosives detection. *Journal of Materials Chemistry A* **2014,** *2* (35), 14613-14621.

234. Wang, W.; Shen, D.; Li, X.; Yao, Y.; Lin, J.; Wang, A.; Yu, J.; Wang, Z. L.; Hong, S. W.; Lin, Z., Light-Driven Shape-Memory Porous Films with Precisely Controlled Dimensions. *Angewandte Chemie International Edition* **2018,** *57* (8), 2139-2143.

235. Gao, F.; Yao, Y.; Wang, W.; Wang, X.; Li, L.; Zhuang, Q.; Lin, S., Light-Driven Transformation of Bio-Inspired Superhydrophobic Structure via Reconfigurable PAzoMA Microarrays: From Lotus Leaf to Rice Leaf. *Macromolecules* **2018,** *51* (7), 2742-2749.

236. Xiong, X.; Zou, W.; Yu, Z.; Duan, J.; Liu, X.; Fan, S.; Zhou, H., Microsphere Pattern Prepared by a "Reverse" Breath Figure Method. *Macromolecules* **2009,** *42* (23), 9351-9356.

237. Wang, Z. L., Triboelectric Nanogenerators as New Energy Technology for Self-Powered Systems and as Active Mechanical and Chemical Sensors. *ACS Nano* **2013,** *7*, 9533-9557.

238. Galeotti, F.; Kozma, E.; Mróz, W.; Kutrzeba-Kotowska, B., Single-step shaping of fluorescent polymer beads by a reverse breath figure approach. *RSC Advances* **2015,** *5* (46), 36315-36319.

239. Duarte, A. R.; Maniglio, D.; Sousa, N.; Mano, J. F.; Reis, R. L.; Migliaresi, C., From honeycomb- to microsphere-patterned surfaces of poly(lactic acid) and a starch-poly(lactic acid) blend via the breath figure method. *J Appl Biomater Funct Mater* **2017,** *15* (1), e31-e42.

240. Lan, X.; Ma, X.; Wang, L.; Shi, Y.; Gu, Q.; Wu, L.; Gu, X.; Luo, Z., Self-Assembly of Diblock Copolymers Containing Thermo- and Photoresponsive Lower Critical Solution Temperature Phase Behavior Polymer with Tunable Assembly Temperature in an Ionic Liquid Mixture. *ACS Omega* **2019,** *4* (6), 11229-11236.

241. Yin, L.; Zhao, Y.; Jiang, S.; Wang, L.; Zhang, Z.; Zhu, J.; Zhang, W.; Zhu, X., Preferential chiral solvation induced supramolecular chirality in optically inactive star Azo polymers: photocontrollability, chiral amplification and topological effects. *Polymer Chemistry* **2015,** *6* (39), 7045-7052.

242. Wang, J.-S.; Matyjaszewski, K., Controlled/"living" radical polymerization. atom transfer radical polymerization in the presence of transition-metal complexes. *Journal of the American Chemical Society* **1995,** *117* (20), 5614-5615.

243. Gao, X.; Gao, F.; Chen, L.; Yao, Y.; Chen, T.; Lin, S., Tuning the morphology of amphiphilic copolymer aggregates by compound emulsifier via emulsion–solvent evaporation. *Journal of Saudi Chemical Society* **2018,** *22* (3), 297-305.

244. White, T. J.; Serak, S. V.; Tabiryan, N. V.; Vaia, R. A.; Bunning, T. J., Polarization-controlled, photodriven bending in monodomain liquid crystal elastomer cantilevers. *J. Mater. Chem.* **2009,** *19* (8), 1080-1085.

245. Chen, J.; Guo, H.; He, X.; Liu, G.; Xi, Y.; Shi, H.; Hu, C., Enhancing Performance of Triboelectric Nanogenerator by Filling High Dielectric Nanoparticles into Sponge PDMS Film. *ACS Applied Materials & Interfaces* **2016,** *8* (1), 736-744.

246. Bian, S.; Williams, J. M.; Kim, D. Y.; Li, L.; Balasubramanian, S.; Kumar, J.; Tripathy, S., Photoinduced surface deformations on azobenzene polymer films. *Journal of Applied Physics* **1999,** *86* (8), 4498-4508.

247. Singhal, R., Surface to volume ratio for sphere. In *Ektalks*, 2018.

248. Galinski, H.; Ambrosio, A.; Maddalena, P.; Schenker, I.; Spolenak, R.; Capasso, F., Instability-induced pattern formation of photoactivated functional polymers. *Proceedings of the National Academy of Sciences* **2014,** *111* (48), 17017-17022.

249. Xu, C.; Zhang, B.; Wang, A. C.; Zou, H.; Liu, G.; Ding, W.; Wu, C.; Ma, M.; Feng, P.; Lin, Z.; Wang, Z. L., Contact-Electrification between Two Identical Materials: Curvature Effect. *ACS Nano* **2019,** *13* (2), 2034-2041.

250. Lin, S.; Xu, L.; Chi Wang, A.; Wang, Z. L., Quantifying electron-transfer in liquid-solid contact electrification and the formation of electric double-layer. *Nat Commun* **2020,** *11* (1), 399.

251. Neagoe, M. B.; Prawatya, Y. E.; Zeghloul, T.; Dascalescu, L., Influence of surface roughness on the tribo-electric process for a sliding contact between polymeric plate materials. *IOP Conf. Series: Materials Science and Engineering* **2017,** *174*, 012003.

252. Bhushan, B., Contact mechanics of rough surfaces in tribology: multiple asperity contact. *Tribology Letters* **1998,** *4* (1), 1-35.

253. Willatzen, M.; Lew Yan Voon, L. C.; Wang, Z. L., Quantum Theory of Contact Electrification for Fluids and Solids. *Advanced Functional Materials* **2020,** *30* (17).